Adaptive Optics Correction of Ocular Higher-Order Aberrations and the Effects on Functional Vision

by Eugénie Dalimier

Supervisor: Prof. Chris Dainty

A thesis submitted in partial fulfilment of the requirements for the degree of Doctor of Philosophy,

Department of Experimental Physics, Science Faculty,
National University of Ireland, Galway

August 2007

Contents

Abstract

Adaptive optics is a technique originally developed to provide a dynamically adaptable diffraction-limited correction of telescopes images. It was recently implemented for the correction of ocular higher-order aberrations (beyond defocus and astigmatism). Prior to this work, research focus has been on the implementation of adaptive optics techniques in retinal imaging systems. Such techniques can also help gaining new knowledge on the combined optical and neural limitations of visual functions through psychophysical tests. It has been proven that the correction of higher-order aberrations can improve contrast sensitivity as well as visual acuity, for large pupils under photopic conditions. However, the optical and neural processes of vision are dependent on the visual tasks and the ambient light. We present here a study of the correction of ocular higher-order aberrations with adaptive optics, and the effects on functional visual performance in different light regimes. An existing adaptive optics system was modified for this purpose. The limitations of the system were thoroughly examined in view of its optimisation; in particular we present a practical analysis of deformable mirrors for vision science adaptive optics. We also present experimental data obtained on the effects of higher-order aberrations for a contrast acuity test, as a function of light level, and simulations based on an ideal observer model derived for the same visual test. The results show that the effects of higher-order aberrations on functional vision increase with pupil size but decrease as the light level is decreased. As a result, the typical overall benefit on visual performance that can be expected from absent or reduced higher-order aberrations under normal variations in ambient illumination is limited. The novel results give new insight on the application of adaptive optics techniques for everyday vision and for the investigation of visual function.

Acknowledgments

I would like to thank first my supervisor, Chris Dainty, who gave me the opportunity to work on this project and provided me with high quality guidance and support throughout the project. This research was based on the adaptive optics system built as part of her PhD work by Karen Hampson at Imperial College, London. I want to acknowledge John Barbur from City University, London, for his fruitful collaboration to our project, his suggestions and help for the major experimental study of this Thesis. I am also very grateful to Larry Thibos (Indiana University, USA) for providing the statistical model to generate the sample eye aberrations that were used in the simulations. I want to thank Simone Esposito (Osservatorio Astrofisico di Arcetri, Italy) and Harrisson Barrett (University of Arizona, USA) for their invaluable input during and even after their stay in our research group. I thank all my colleagues, and especially Sasha Goncharov for our scientific discussions and David Thorton for his technical support with the system software. I am also indebted to the subjects who volunteered for the experiments, especially those from the group who kindly accepted to give me some of their time. Finally, thank you Fabien for being here.

This research was funded by Science Foundation Ireland under grant number SFI/01/PI.2/B039C and by a European Union EU Research Training Network, contract number HPRN-CT-2002-00301 "SHARP-EYE".

Abbreviations

ADS: amplitude difference of spectrum
AFC: alternative forced-choice
AO: adaptive optics
AUC: area under the curve
BKE: background-known-exactly
CCD: charge-coupled device
cpd: cycles per degree
cpl: cycles per letter
CRT: cathode ray tube
CSF: contrast
D: Diopter
DLP: digital light-processing
DOG: difference-of-Gaussians
HO: higher-order
LCSLM: liquid crystal spatial light modulator
MEMS: microelectromechanical system
MMDM: micromachined membrane deformable mirror
MTF: modulation transfer function
NTF: neural transfer function
OTF: optical transfer function
PMN: lead magnesium niobate
PSF: point spread function
PZT: lead zirconium titanate
ROC: receiver operating characteristic
rms: root mean square
SEM: standard error of the mean
SKE: signal-known-exactly
SNR: signal-to-noise ratio
VSG: visual stimulus generator
Td: Troland

Preface

If the human eye is regarded as a special organ, it is not only because vision is the most used of our senses, but probably also because part of the eye constitutes an extension of our brain. An improvement in our understanding of visual functions gives an insight into general processes in the brain. This partly explains why new technologies based on wavefront sensing and wavefront correction recently created such enthusiasm in the vision research field.

One will always be amazed that as efficient and sophisticated as the eye can be in a large range of illumination and visual tasks, its optical components are far from the quality expected as compared to a man-made camera. This paradox was first formulated by Helmholtz, yet complete characterisation of the eye's optics were not possible before the development of ocular wavefront sensing techniques. The adaptive optics correction of ocular higher-order aberrations, as first proposed by Smirnov in 1961 [1] and implemented in 1997 by Liang *et al.* [2] took ophthalmoscopy and vision research a step forward. Correcting the ocular optical quality down to diffraction-limit made it possible to image the structures of the retina until then invisible, and carry out psychophysical experiments with until then unfeasible stimuli. In particular, such correction opened the possibility for "super-vision", beyond the limits imposed by standard ophthalmic prescriptions. The motivations behind this Thesis were to investigate the real impact of higher-order ocular aberrations on functional vision, that is for visual tasks and environment conditions representing everyday vision. Would normal healthy people benefit from such a correction? Besides from practical applications (the implementation of customised ophthalmic correction), the focus of this Thesis was to use the adaptive optics novel techniques now available to gain some new understanding of the visual processes: how do the optical and neural limits of the eye balance with each other? How can such an imperfect eye maintain high per-

formance in the broad light range that we face everyday?

The present work is the continuation of a PhD project led by Karen Hampson at Imperial College, London. She built the original adaptive optics system that was used in this project. Some time was spent on the adaptive optics system itself to modify, optimise and fully analyse its performance and limitations. As part of this work, several deformable mirrors were fully characterised and compared. Several components were also added in the vision simulator part of the system before experiments could be carried out. Finally, the experimental results were also analysed using a model of the human observer.

Synopsis

The first two chapters give an introduction to the project: through background material in physiological optics and vision, as it has been studied since more than a century ago until recent developments on ocular aberrations and image quality, and through the principles of adaptive optics, a technique that was developed for astronomy and later applied to ocular science.

Chapter 3 presents an original study of three recent deformable mirrors for the correction of ocular aberrations. The study involves the numerical simulation of the mirrors' performance, based on the influence functions of the mirrors measured experimentally, and the statistical characteristics of the typical ocular wavefronts. The calculations made it possible to select the mirror best suited for the correction of ocular wavefronts. It showed that the stroke and shape of the influence functions, as well as the number of actuators, are important parameters controlling the performance of the mirrors. The method and results were given in a peer-review publication (Publication 2) and used for the analysis and comparison of further mirrors (Publications 3 and 6).

Chapter 4 describes the experimental AO vision simulator used in the Thesis, starting from the initial adaptive optics system built by Karen Hampson. It details the new implementations and analysis performed on the adaptive optics system, focussing on the wavefront sensor accuracy and the performance of the closed-loop correction after implementation of a new modal calibration. Details are also given on the optical and psychophysical design of the visual performance tests. The results of a preliminary experiment are presented.

In Chapter 5, new experimental results are presented on the effects of higher-order aberrations on functional vision, in different light regimes and for different pupil sizes. The experiments were performed with the AO vision simulator; the visual stimulus chosen and the protocol are described. Seven subjects were tested and the results show that the effects of higher-order aberrations on functional vision decrease in the low light regimes, as compared to photopic conditions. The combined effect of ambient light level on pupil dilation and neural sensitivity results in a limited expected visual benefit for normal young subjects in everyday vision. the main results from this study were presented at several conferences (Publications 4, 5, 7 and 8) and accepted for publication in a peer-review journal (Publication 9).

Chapter 6 gives a first attempt to explain the experimental results obtained, through numerical simulations based on a vision model. The model includes the aberrated image formation on the retina, the neural filtering, and the processing of the data to perform the visual task. The analysis was performed with figures of merit to discuss the joint effect of neural sensitivity and higher-order aberrations on the model-observer performance, and compare it to the experimental data obtained. The model was outlined at a conference (Publication 8); it showed good agreement with the experimental results but raises questions for its implementation with other visual stimuli.

The last chapter concludes on the work presented in this Thesis, and gives suggestions on future topics of research.

Publications

1. E. Dalimier, K. M. Hampson, and J. C. Dainty. Effects of adaptive optics on visual performance. In *Opto-Ireland 2005: Imaging and Vision*, Proc. SPIE **5823**, 20–28 (2005).

2. E. Dalimier and C. Dainty. Comparative analysis of deformable mirrors for ocular adaptive optics. *Optics Express* **13**(11), 4275–4285 (2005).

3. E. Daly, E. Dalimier and C. Dainty. Requirements for MEMS mirrors for adaptive optics in the eye. In *MEMS/MOEMS Components and Their Applications III*, Proc. SPIE **6113**, 611309 (2006).

4. E. Dalimier, J. C. Dainty, and J. Barbur. Visual performance as a function of light level (with and without correction of higher order aberrations). 3^{rd} European Meeting in Physiological Optics, London, UK, 7-9 September 2006.

5. E. Dalimier, J. C. Dainty, and J. Barbur. Functional visual performance assessed

with and without correction of ocular aberrations. European Association for Vision and Eye Research Congress, Vilamoura, Portugal, 3-6 October 2006.

6. T. Farrell, E. Daly, E. Dalimier and C. Dainty. Task-based assessment of deformable mirrors. In *MEMS Adaptive Optics*, Proc. SPIE **6467**, 64670F (2007).

7. E. Dalimier, J. C. Dainty, and J. L. Barbur. Effects of higher-order aberrations on visual performance as a function of light level. 2007 ARVO Annual Meeting, Fort Lauderdale, USA, 6-10 May 2007.

8. E. Dalimier, J. C. Dainty, and J. L. Barbur. Psychophysical experiments on visual performance with an ocular adaptive optics system. 6^{th} International Workshop on Adaptive Optics for Industry and Medicine, Galway, Ireland, 12-15 June 2007.

9. E. Dalimier, J. C. Dainty, and J. Barbur. Effects of higher-order aberrations on functional vision as a function of light level. *Journal of Modern Optics*, in press.

Chapter 1

Physiological Optics and Vision

Vision is a complex process encompassing several stages. The aim of this project was to use adaptive optics techniques to investigate the optical quality of the human eye and its effect on visual performance. A short presentation on vision is therefore necessary to give the reader a global view of the tackled problem. We will describe here the optical elements of the eye as an introduction to ocular aberrations. Optical metrics are then presented to derive the effect of ocular aberrations on the retinal image quality, and finally, neural sensitivity is introduced to complete the understanding of the overall sensitivity of the human eye.

1.1 Optics of the Eye

The human eye can be regarded as a simple optical system similar to a camera, containing several refractive elements to image an object onto a sensor, through an optical path limited by an aperture.

In the eye, light is refracted by two principal structures, the cornea and the lens. Many optical models have been derived with the aim of describing in greatest detail the different optical surfaces and media of these refractive structures; we will con-

sider here the simple Gullstrand - Le Grand schematic eye [3]. The greatest refraction occurs at the front surface of the cornea, because of its important curvature and the large difference between the indices of refraction of air (1.0) and of the corneal tissue (1.37). Hence the cornea alone has a total optical power of 40 diopters. The lens is responsible for the remaining refraction and it is flexible to allow focussing of objects at different distances. This process is known as accommodation: the tension of the ciliary muscles surrounding the lens capsule bulges the lens to increase its optical power. The variable power ranges from 10 to 30 diopters in a young child and gets fixed past the age of 45 years. In between the cornea and the lens lies the iris, which contracts or expands according to the surrounding light. This element acts as the pupil: it defines the bundle of optical rays going through the system. Figure 1.1 shows how an object is imaged through the eye, with the marginal rays limited by the pupil. The image is formed on the retina, about 24 mm behind the cornea or 16.7 mm

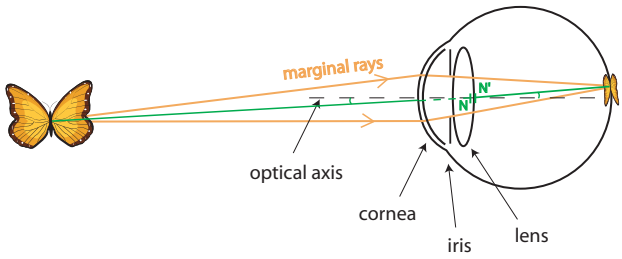

Figure 1.1: Optical schematic of the human eye imaging system.

after the image nodal point. One degree of visual angle hence represents 290 μm on the retina.It can be seen on the drawing that the optical axis differs from the visual axis defined between the point of fixation and the fovea, where the image is formed (in the eye, the two conjugated nodal points are almost superimposed). There is typically a 5 degrees angle between these two axes.

At the retinal level, the image is sampled by the photoreceptors organised in hexagonal mosaics. These can be regarded as pixels of a camera; their gain and physical dimensions yield associated sensitivity and resolution. The first complexity of the retina is that it comprises different classes of receptors, rods and cones. Rods have very good sensitivity and are responsible for detecting dim light. There are about 100 million of them in the human retina; they typically measure 1.5 μm diameter and the highest density, 160 000 rods/mm^2 (equivalent to a centre-to-centre spacing of about 2 μm), is found at 20 degrees from the fovea [4]. There are 20 times less cones in the retina, but as they are almost all concentrated in the fovea and function in bright illumination, they actually account for the most important part of our vision. The central part of the

fovea, which subtends 0.1 mm, is called the foveola, and only contains cones. In this region, cones have a diameter of 1.5 μm and a centre-to-centre spacing of 2 μm. The cone diameter grows bigger away from the fovea and the interspacing increases as more rods intermingle with them. There are three kinds of cones: short-wavelength (S) cones with a sensitivity peak at 420 nm (blue), medium-wavelength (M) cones with a peak at 531 nm (green), and long-wavelength (L) cones with a peak at 588 nm (red). Cones have less sensitivity than rods but a higher saturation level. The range defined between the cones threshold and the rods saturation is called mesopic range. Below mesopic range, where only rods are functioning, lies the scotopic range. At the other extreme, where only cones are functioning, is the photopic range.

1.2 Ocular aberrations

We previously used geometrical optics to describe the ocular optical system; a more thorough analysis requires the principles of wave optics. Ideally, a plane monochromatic wavefront entering the eye converges as a perfect spherical wavefront focussing on the retina. In reality, the wavefront is distorted by the aberrations due to the cornea and the lens. The deviation from a monochromatic perfect spherical wavefront, or

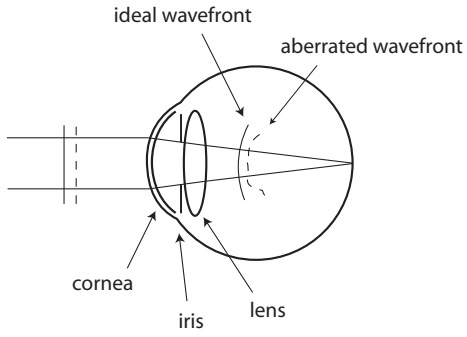

Figure 1.2: Wavefront distortion through the eye.

equivalently expressed at the exit of the eye from a perfectly plane wavefront, can be denoted $W(\rho,\theta)$, with (ρ,θ) the polar coordinates in the plane perpendicular to the propagation of the wavefront. Assessing ocular aberrations requires a discrete representation of $W(\rho,\theta)$ through a polynomial expansion,

$$W(\rho,\theta) = \sum_{i=0}^{\infty} a_i P_i(\rho,\theta), \tag{1.1}$$

where P_i represents a polynomial and a_i is the corresponding weighting coefficient. In this Thesis, we will use Zernike polynomials. The Zernike polynomials form an orthogonal set over a circle of unit radius; their complete derivation can be found in Reference [5]. Although this wavefront decomposition is only one of many possible representations, it is commonly used to describe optical systems. In particular, its wide use in the visual optics community led to a formal convention given by the Optical Society of America [6]. We recall here their normalized single indexing representation as defined by the OSA,

$$Z_i(\rho,\theta) = Z_n^m(\rho,\theta) = \begin{cases} \sqrt{2(n+1)}\, R_n^{|m|}(\rho)\, \cos(m\theta) & \text{if } m \neq 0 \text{ and } i \text{ even} \\ \sqrt{2(n+1)}\, R_n^{|m|}(\rho)\, \sin(|m|\theta) & \text{if } m \neq 0 \text{ and } i \text{ odd} \\ \sqrt{n+1}\, R_n^0 & \text{otherwise.} \end{cases} \tag{1.2}$$

The radial order n and the angular frequency m can be calculated from the single index i with the following relationships

$$\begin{cases} n = roundup\left[\frac{-3+\sqrt{9+8i}}{2}\right] \\ m = 2i - n(n+2) \\ i = 0,1,2... \end{cases} \tag{1.3}$$

As for the radial part R_n^m, it is given by

$$R_n^{|m|}(\rho) = \sum_{s=0}^{(n-|m|)/2} (-1)^s \frac{(n-s)!}{s![(n+|m|)/2-s]![(n-|m|)/2-s]!} \rho^{n-2s}. \tag{1.4}$$

Typically, a finite number N of Zernike polynomials is chosen to represent the wavefront error which is then expressed as

$$W(\rho,\theta) = \sum_{i=0}^{N} a_i Z_i(\rho,\theta) \tag{1.5}$$

and the coefficients a_i are given by the inner product integrals over the circular aperture A

$$a_i = \int\int_A W(\rho,\theta) Z_i(\rho,\theta)\, d\rho\, d\theta. \tag{1.6}$$

The square root σ of the variance of the deviation $W(\rho,\theta)$, commonly referred to as its rms, can be calculated directly from its expansion

$$\sigma = \sqrt{\sum_{i=0}^{N} a_i^2}. \tag{1.7}$$

An interesting feature of Zernike polynomials, and probably one of the reasons why they are widely used in the vision community, is that some terms are directly related to commonly known ocular aberrations. For example, structural abnormalities of the eye, such as myopia and hyperopia, introduce a defocus term that appears as the 5^{th} term of this expansion. Myopic eyes are too long to focus an object from infinity on the retina; it is only when the object gets closer that the refractive elements can be adapted to conjugate it with the retina. As for hyperopia, the eye is in this case too short, and the subject has to accommodate to look at infinity; when the object gets too close, it falls out of the range of accommodation. As the Zernike defocus term depends on accommodation, it will be given in this Thesis for a relaxed eye, unless specified otherwise. Asymmetries of curvature of the cornea result in astigmatism, represented by the 4^{th} and 6^{th} Zernike terms. The so called sphero-cylindrical refractive errors just mentioned are commonly corrected by ophthalmic prescriptions. Further Zernike terms represent higher-order aberrations: spherical aberration and coma are two of the best known of these. Spherical aberration arises from the sphericity of the optical surfaces. Coma is mainly caused by decentering and tilts of the optical system, one major factor being the 5 degrees angle between the optical axis and the line of sight as mentioned previously. The other higher-order ocular aberrations are due to further irregularities of the optical ocular structures. The overall wavefront error is spatially non-stationary over the pupil, with higher deformation at the edges of the pupil. Interestingly, it has been shown that the relative contributions of optical aberrations of the cornea and the crystalline lens tend to compensate for each other, in particular for horizontal/vertical astigmatism, spherical aberration and lateral coma [7, 8].

Higher-order ocular aberrations have raised interest probably since Helmholtz proposed several experiments to verify their existence in 1909. A section in the next chapter is devoted to the description of aberrometry techniques developed since. Several statistical studies have now been carried out on ocular aberrations in normal populations [9, 10, 11]. It was found that the magnitude of the aberration for each term generally decreases as the radial order increases. Even after ophthalmic cor-

rection, the residual second-order wavefront variance is greater than the combined higher-order wavefront variance for most of the subjects. These residual refractive aberrations can sometimes be accounted for in the term "higher-order aberrations", especially in adaptive optics systems. The mean wavefront error rms due to higher-order aberrations (3^{rd} order and higher) given by Thibos *et al.* over a 6 mm pupil is 0.3 μm (100 human eyes) [10] while that found by Porter *et al.* is 0.35 μm for a 5.7 mm pupil (109 human eyes) [9]. These values were calculated from the sum of the squared mean absolute Zernike coefficients (average total variance), then root-squared to give the mean wavefront error rms. Although wavefront aberration varies substantially between individuals, it appears that the population average for each higher-order Zernike coefficient, except spherical aberration, approximates zero. One attempt was made to fit aberrations statistics to the classical Kolmogorov model [12] which is used for turbulence in astronomy. However, it can be argued that the non-stationarity of ocular aberrations invalidates this fit. Finally, there seems to be a tendency for the aberrations to show mirror symmetry between the left and right eyes [13, 9].

The dynamic characteristics of ocular aberrations have also been investigated; several studies reported significant temporal fluctuations up to a frequency of 5 Hz [14, 15], or even 30 Hz and 70 Hz [16, 17]. It should be noted that the temporal characteristics of ocular aberrations do not strictly follow a stationary behaviour; therefore, one could bring into question these results based on power spectrum calculations. The causes of the higher-order aberrations dynamic behaviour remain a subject of investigation. Microfluctuations in accommodation (typically a few tenths of a dioptre) cannot explain the measured values (around 0.05 - 0.1 μm) of amplitude of the higher-order aberrations dynamics for a 4.7 mm pupil [15]; similar conclusions were drawn from an analysis of ocular movements (saccades, drift, tremor). In another study, Hampson *et al.* [18] measured a weak correlation between the aberration dynamics and the cardiopulmonary system. Finally, the tear film is a possible candidate, as precise measurements of its dynamics have recently been achieved [19, 20, 21]. The measured amplitudes of tear film aberrations were comparable to the total wavefront error rms variations. On a longer timescale, higher-order aberrations are also dependent on the environment: specifically, they are function of the pupil size [22] which in turn varies with ambient light, and they change with accommodation [23] according to the visual scene. Finally, a study showed that they increase with age [24].

1.3 Retinal image quality

The effect of ocular aberrations on image quality can be derived using well-known mathematical tools. Considering the wavefront deviation $W(\rho,\theta)$ over the exit pupil with respect to a perfect sphere centered on a point A in the Gaussian image plane, it can be shown [5] that the intensity in the image plane can be expressed as

$$I(x,y) = C\left|\int_{-\infty}^{+\infty}\int_{-\infty}^{+\infty} P(\xi,\eta)\,\exp\left[-\frac{2\pi i}{\lambda R}(x\xi+y\eta)\right]d\xi\,d\eta\right|^2 \tag{1.8}$$

where (x,y) are the coordinates defined with respect to A, C is a constant, λ is the wavelength, and R is the distance from the exit pupil to the Gaussian image plane. The pupil function $P(\xi,\eta)$ is defined as

$$P(\xi,\eta) = \begin{cases} \exp\left[\frac{2\pi i}{\lambda}W(\xi,\eta)\right] & \text{for } (\xi,\eta) \text{ in the aperture} \\ 0 & \text{elsewhere.} \end{cases} \tag{1.9}$$

The intensity distribution $I(x,y)$ is the response of the system to a point source at infinity; it is commonly called the intensity point spread function (PSF). Equation 1.8 shows that it is proportional to the squared modulus of the Fourier transform of the pupil function. The shape of the PSF is related to the image quality, more precisely its width gives an indication of the resolution of the image on the retina. When no aberration is present and the exit pupil is circular, the intensity distribution is the well known Airy disc function, and its first minimum is located at an angle θ

$$\theta = 1.22\,\frac{\lambda}{D} \tag{1.10}$$

with D the diameter of the pupil. For an aberration-free eye of a 3 mm diameter pupil and a wavelength of 550 nm, a point source at infinity is imaged on the retina as an Airy disc of 46 arc seconds radius, or 4 μm radius.

The PSF of the system gets wider with the aberrations, and thus image quality is altered. In the presence of small aberrations, the central intensity the PSF is reduced and the energy is redistributed around. In that case, the ratio of the intensity PSF at the central point A with aberrations to the central intensity without aberrations can be expressed as

$$S = 1 - \left(\frac{2\pi}{\lambda}\right)^2 \sigma^2, \tag{1.11}$$

where σ is the root-mean-square wavefront deformation as defined in Equation 1.7.

The value of S is referred to as the Strehl ratio. Hence for small aberrations, σ can be directly related to image quality; it is in that case a useful figure of merit, which is widely used in the vision scientist community, due to the simplicity of its calculation. A tolerance criterion to assess the image quality was defined by Maréchal (1947): it states that an optical system is considered as diffraction-limited when the Strehl ratio exceeds 0.8, or equivalently when σ is below $\lambda/14$. This is a typical criteria used to assess the correction of ocular aberrations. For the eye, the diffraction limit is given by the size of the iris. As the aberrations increase with the size of the pupil [10], it was shown that under a certain pupil diameter (of a value ranging from 3 mm [9] to 1.22 mm [10]) they are overcome by diffraction.

Under the assumption of incoherent illumination, which is valid for everyday vision and the visual tests designed in this project, and the assumption of stationarity (independence of the aberrations with the field angle), the intensity of the image of an object through the system can be written as the convolution of the intensity PSF with the intensity of the object

$$I_{out}(x,y) = \int_{-\infty}^{+\infty} \int_{-\infty}^{+\infty} \mathrm{PSF}(x-x_1, y-y_1)\, I_{in}(x_1,y_1)\, dx_1\, dy_1. \tag{1.12}$$

Using Fourier transforms **FT**, this expression simplifies to

$$I_{out}(x,y) = \mathbf{FT}^{-1}\left\{\mathbf{FT}\{I_{in}(x,y)\} \times \mathbf{FT}\{\mathrm{PSF}(x,y)\}\right\}. \tag{1.13}$$

Knowing the wavefront aberrations, it is thus easy to calculate the image of an object as it is formed on the retina.

The Fourier transform of the PSF is the optical transfer function OTF and its modulus is the modulation transfer function MTF

$$\mathrm{MTF} = |\mathrm{OTF}| = |\mathbf{FT}\{\mathrm{PSF}\}|. \tag{1.14}$$

The MTF gives the ratio of the modulation[1] of the image of a sinusoidal grating to that of the object, as a function of the spatial frequency of the grating. It can be understood as the attenuation in contrast due to the eye, or contrast sensitivity of the system. It indicates how well spatial frequencies are passed through the ocular optical system. Figure 1.3 shows example of measured MTFs for a human eye, at different pupil diameters. Not unexpectedly, as the pupil is increased, the magnitude of aberrations increases and the MTF is lowered. An interesting study by McLellan *et al.* has shown

[1] The modulation is defined as $\frac{I_{max}-I_{min}}{I_{max}+I_{min}}$

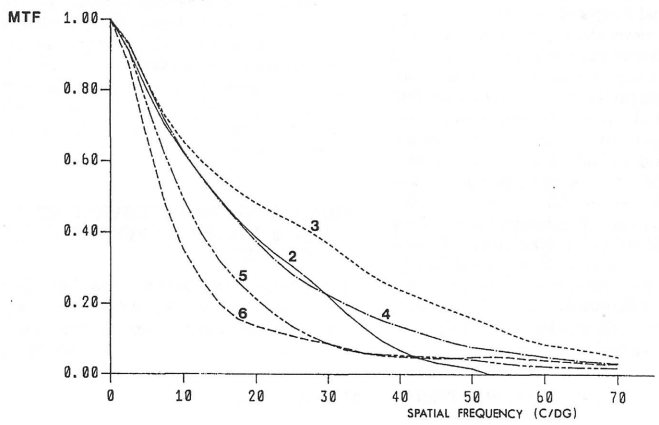

Figure 1.3: Sections of two-dimensional calculated MTFs from measured ocular aberrations at the pupil diameters (mm) indicated (after Artal [22]).

that the signs and orientations of the individual Zernike ocular aberrations tend to optimise the overall MTF of the human eye, suggesting positive functional interrelation [25]. The MTF is a measure commonly used in vision science; not only does it characterise the optical quality of the eye, it can also be used to predict the effect of ocular higher-order aberrations on visual performance, as will be explained in the following section.

Other optical degradations affect image quality. Firstly, as was mentioned earlier, a perfect wavefront does not result in a perfect focal delta function, but in a broader function known as the Airy disk, dependent on the pupil size. Scattering arising from the small particles in the eye and reflections from the optical surfaces will further alter the image. Furthermore, it should not be forgotten that as a refractive optical system, the eye suffers from dispersion: the indices of refraction are dependent on wavelength, hence different wavelengths focus at different points on the retina. With a broad spectrum light source as is often encountered in human vision, this gives rise to the so-called longitudinal chromatic aberration (spread of the focal point along the longitudinal axis), and transverse chromatic aberration for off-axis objects. In the case of the eye, the fovea is not on the optical axis, so it is already vulnerable to transverse chromatic aberrations. The polychromatic MTF can be computed from the monochromatic MTF, the longitudinal and transverse chromatic aberrations and the cones spectral sensitivities. Such calculations demonstrated that the ocular aberrations seem to attenuate the effects of chromatic aberrations [26].

Finally, a particularity of the human retina should be taken into account when considering image quality. Human cones are known to act as waveguides, tuned to a cer-

tain orientation, typically towards the center of the pupil. This is the Stiles-Crawford effect, first reported in 1933: the authors noticed that cones are more sensitive to light entering near the center of the pupil than light entering peripheral regions of the pupil [27]. The effect is now referred to as the Stiles-Crawford effect of the first kind, measured psychophysically, as opposed to the double-pass "optical" Stiles-Crawford effect that can be measured with reflectometry. Both effects have been thoroughly measured [28] and recently analytically described based on waveguide theory [29]. The impact on image quality of the Stiles-Crawford effect can be computed as an apodisation in the pupil function, implemented in the PSF and MTF calculations (Equations 1.8 and 1.14). Marcos *et al.* found that the volume of the MTF increased when introducing cone directionality for the 12 eyes they tested [30].

1.4 Contrast sensitivity of the human eye

Vision is a very complex process, of which the optical image formation on the retina is only the first part. In order to understand what limits visual performance, it is necessary to go through the whole process. After being sampled by the photoreceptors, the image is locally processed through several levels of cells in the retina, and the information is sent to the cortex through the optic nerve. It is not the purpose here to describe thoroughly these stages, but rather to ensure that the reader can grasp the complexity of the visual pathways at the retinal level, as simplistically described by Figure 1.4. A direct path sends the signal generated by the photoreceptor via a bipolar cell onto a ganglion cell, but a more indirect path from the same photoreceptor involves the interposed horizontal and amacrine cells, and generates an opposite signal. This is known as lateral inhibition, and results in bipolar and ganglion cell receptive fields: these are the total areas of photoreceptors that communicate directly or indirectly, positively or negatively, with the bipolar or ganglion cell. In a uniform field, bipolar/ganglion cells receive the direct signal from one or several photoreceptors and opposite signal from surrounding photoreceptors. The total summation results in the cancelation of the signals; the human eye visual pathways are designed to sense changes in intensity. Furthermore, the pathways are functions of eccentricity and light level. At the center of the fovea and under photopic light, the direct path is such that a single cone feeds a single bipolar cell which in turn feeds a single ganglion cell; hence the resolution of the cones mosaic is retained through the visual pathway. This is not true at higher eccentricity where larger spatial summation occurs. Although the photoreceptor mosaic gets coarser and ocular aberrations

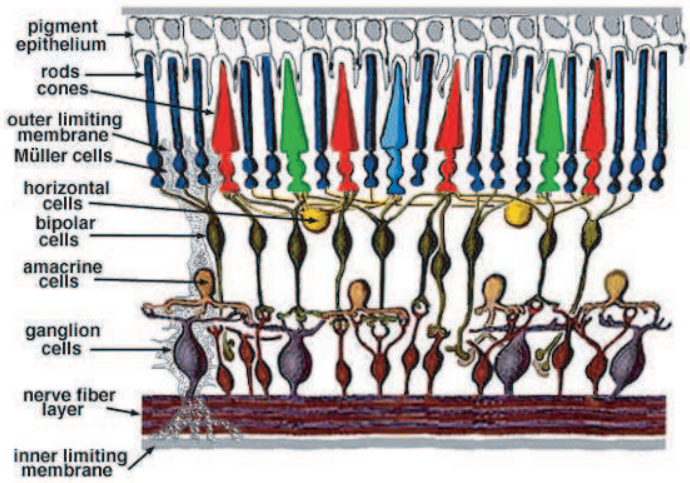

Figure 1.4: Schematic of the retinal circuitry. Taken from webvision.med.utah.edu.

increase, ganglion cells are here the limiting factors in resolution [31]. As light level is decreased, several factors should be taken into account. Obviously, the signal-to-noise ratio of the receptor's detection is decreased, it is in fact proportional to the square-root of the intensity according to the DeVries-Rose law [32]. Furthermore, the bipolar and ganglion cell receptive fields spread out [4], and if light is decreased down to mesopic and scotopic light, rod visual pathways start to intermingle with cone visual pathways. The cone and rod display very different spatial and temporal integration, spectral sensitivity and retinal distribution, which all yield a complex interaction [33].

In a similar manner to the metrics derived in the previous section to represent the optical quality of the human eye and its effect on image quality, the neural sensitivity, function of spatial frequency, is a common measure of the neural performance. The reason probably is the evidence of frequency channel responses in the visual system [34]. Neural sensitivity was first measured by Arnulf *et al.* in 1960 [35] using interferometric methods as introduced by Le Grand [36]. Two narrow beams entering the pupil can form adjustable interference fringes on the retina without degradation from the ocular optics. It is then possible to define and measure the neural MTF in a similar way as the optical MTF (see Eq. 1.14). The measurement of the neural MTF involves psychophysical methods, where a certain task (e.g. discrimination of the orientation of a grating) is used to determine the contrast threshold required by the subject to detect it at a certain spatial frequency. The neural contrast sensitivity is the inverse of the contrast threshold. The product of the neural and optical MTFs gives

the contrast sensitivity function (CSF) of the eye

$$\text{CSF} = \text{MTF}_{optical} \times \text{MTF}_{neural}. \tag{1.15}$$

This simple relation can be used to predict the effect of ocular aberrations on visual performance. The ratio of the optical MTF without aberrations over the MTF with aberrations is commonly referred to as the visual benefit. Such calculations were derived by Guirao *et al.* [37] using data of higher-order aberrations in a population of human eyes. They measured an average of 0.35 μm wavefront error rms for a 5.7 mm pupil in 109 subjects, and calculated an average visual benefit of 2.5 at 16 c/deg and 3 at 32 c/deg, the latter frequency being close to the limit of visual acuity.

Contrast sensitivity can also be measured directly, if gratings are seen normally through the whole pupil of the eye. Complete sets of data can help disentangling the different spatial filtering stages of the eye. Figure 1.5 illustrates this analysis, with a measured CSF, a measured neural MTF, and the optical MTF derived using Equation 1.15. The reader can compare the calculated optical MTF with the curves

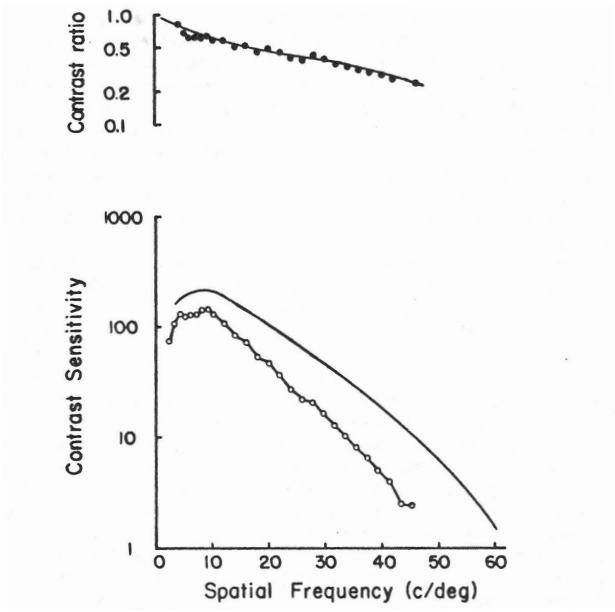

Figure 1.5: Optical modulation transfer function computed from the neural modulation transfer function and the contrast sensitivity function. At the bottom are the CSF (lower curve) and the neural MTF (upper curve); at the top is the difference between these two curves. Taken from [38].

given in Figure 1.3. The overall contrast sensitivity function is shaped as a band-pass filter: high frequencies are filtered by both optical and neural factors, while low frequencies are filtered mainly by the neural processing, through spatial summation

as just discussed. The effect of higher-order aberrations on contrast sensitivity was investigated by Williams group using adaptive optics [2, 39], a technique that will be explained in the next chapter. They showed an improvement by a factor 2-3 in contrast sensitivity for 6 mm dilated pupils in two subjects.

The cut-off frequency of the contrast sensitivity represents the acuity limit. This parameter is often used by optometrists to measure visual performance because it can easily and quickly be measured with letter charts for example. We shall refer here to the description of the retina given in Section 1.1 and the physical dimensions of the photoreceptors which were given. The Shannon sampling theorem states that a bandwidth limited signal can be fully resolved if the sampling frequency is at least twice as big as the highest frequency of the signal. Therefore, the highest frequency f_c (in c/deg) of a sinusoidal grating that can be resolved by the retina is given by

$$f_c = \frac{p\pi}{180 * S\sqrt{3}} \tag{1.16}$$

where p is the nodal distance of the eye and S the center-to-center receptor spacing. Anatomical measurements of cone spacing at the fovea lead to predictions of a resolution limit of about 60 to 85 c/deg. This value is close to the 50-60 c/deg limit measured by Williams using interference fringes [40]. He noticed that gratings beyond the cut-off frequency could still be detected but not resolved; they rather appear as lower frequency "zebra stripes", which is a typical indicator of aliasing. It is interesting to note that the diffraction limit as we computed it for a 3-mm pupil (the higher-order aberrations are then negligible) gave a resolution of 47 arc seconds, or 76 c/deg in frequency which is about the retinal limit. This seems to indicate a good balance between the degradation due to optical aberrations and the actual retinal resolution. As we have mentioned earlier, the limitation at higher eccentricity is given not by the ocular aberrations nor the receptor mosaic, but rather by the ganglion cells; aliasing phenomena can then be observed naturally.

Contrast sensitivity as a function of spatial frequency is a representation of visual performance that may not provide all the relevant information on vision. Indeed, real life images contain a broad spectrum of frequencies. Contrast sensitivity measurements for a particular spatial frequency do not represent these conditions. In fact, as such measurements usually involve a sinusoidal grating weighted with a Gaussian envelope, they probably contain a wider range of frequencies and cannot be directly related to the computed MTF. The spatial frequency domain functions representing vision provide a good basis for the understanding of visual function, but they do not

fully render the complexity and limitations of visual processes. As we have seen, vision involves several stages that all have their limitations, and these furthermore vary with ambient light. Neural sensitivity changes with light level for reasons explained earlier. The effect of luminance on visual performance has been measured in terms of contrast sensitivity function, showing a decrease as retinal illuminance[2] was decreased for a 2-mm fixed pupil [41, 42], 3-mm fixed pupil [43] and natural pupils [43]. Other measurements include the results of Coletta *et al.* who investigated the effect of luminance on neural MTF, as measured by interferometric techniques [44]. The different light regimes also affect the pupil size, resulting in different magnitudes of ocular aberrations and light scatter. It shall be noted that to the author's knowledge, no direct comparison has been done of neural and optical sensitivities with light levels, although earlier papers [45] suggested an optimized pupil size for visual performance as a factor of luminance. The extent to which neural and optical limitations may relate to each other in a range of ambient light levels for every day functional vision remains an open subject.

The work presented in this Thesis was driven by the hope that the recent techniques available to measure and correct higher-order aberrations would enable us to understand better the impact of these aberrations on visual performance, beyond the usual contrast sensitivity analysis. The next chapter is devoted to the description of adaptive optics, focussing on its implementation in vision science.

[2]Retinal illuminance is is defined as the product of the luminance in the pupil plane, measured in cd/m^2, with the pupil area, in mm^2. Its unit is Troland (Td).

Chapter 2

Ocular Adaptive Optics

The concept of Adaptive Optics (AO) was first proposed by Babcock in 1953 [46] to improve astronomical images otherwise degraded by the turbulence present in the atmosphere. Turbulence creates local and dynamic changes of optical path, the origin of wavefront aberrations as we defined them in Section 1.2. Babcock suggested to use an active optical element to correct the instantaneous wavefront distortions, after having measured them with a so-called wavefront sensor which would deliver the signals necessary to drive the correcting device. The limitations of the technology at the time did not allow the construction of such a system. However, the potential gain in resolution uncovered by this technique encouraged substantial investments, especially from the US government for defence projects. This led to the construction in 1977 of the first adaptive optics system able to sharpen two-dimensional images of satellites placed on orbit [47]. Astronomers were soon to follow, thanks to the development of better detectors allowing detection of faint sources in the near infrared; the 19 actuator COME-ON system was installed on the telescope at La Silla in Chile in the early 1990's [48]. All large telescopes are now equipped with adaptive optics systems operating in the near infrared.

Although Smirnov had mentioned the idea in 1961 [1], it was not until 1989 that adaptive optics was introduced in vision science. That year, Dreher *et al.* presented a system based on a deformable mirror conjugated with the human eye to correct astigmatism [49]. They did not however measure the wavefront aberrations, relying on ophthalmic prescriptions. The first complete system was built in 1997 by Liang *et*

al. [2]; they reported both high-resolution retinal images and a possible enhancement of vision thanks to AO. Following this successful experiment, several other ocular AO systems have since been built around the world. Adaptive optics relies on two technologies, namely wavefront sensing and wavefront correction, that will be detailed below, with particular attention to the application in vision.

2.1 Wavefront sensing in the eye

Measuring ocular aberrations requires sending light through the eye and sensing the deformations introduced. Two approaches can be considered. The subject's retina can be used as the actual sensor, hence only one pass through the system is required for such psychophysical methods. For objective methods, on the other hand, light needs to go in and out of the eye, the first pass forming a secondary light source on the retina.

History of ocular aberrometry

The first direct measurements of the overall ocular aberrations date back to 1961, with a method developed by Smirnov [1]: a coincidence subjective technique was used to measure local tilts introduced by aberrations in sub-pupils of the eye. Later, this was to become the laser ray tracing method [50]. Small laser collimated beams are sequentially scanned through the pupil, and the displaced spots formed by the so-called rays are re-imaged onto a camera to measure the local tilts induced in the first pass of the light through the eye. Other early techniques include that pioneered in 1969 by Berny [51], who adapted the Foucault knife edge test to ocular aberrations. In 1984, Walsh *et al.* [52] developed an objective version of the Howland cross-cylinder aberroscope [53]. Similarly to the laser ray tracing technique, the principle of this aberroscope is to compute the wavefront aberrations from their local partial derivatives (tilts in the pupil plane, corresponding to displacements in the retinal plane). Subjective methods suffer from the length of time needed to perform the experiment, and the variability in the results obtained. The earlier objective techniques, on the other hand, lacked from good imaging technologies and sufficient computing ability available at the time.

An approach used more recently consists in retrieving the wave aberration from double-pass intensity images [54, 55]. A point source at infinity is imaged on the retina, effectively giving the PSF of the eye, and reimaged on a camera. This idea was

pioneered by Flamant in 1955 [56] who imaged the double-pass line spread function (i.e. double-pass image of a line through the optics of the eye) on a photographic film. The technique relies on the assumption of incoherence of the imaging process provided by the long exposures; the intensity output is therefore the auto-correlation of the PSF of the eye [57]. The single MTF can be retrieved, but the phase modulation transfer cannot [58]. The implementation by Santamaría *et al.* of digital calculations in 1987 [54] improved greatly the efficiency of the measurement as compared with the photographic techniques used by Flamant and others. However, although the recording of the data could follow the dynamics of the subject, the time needed for analysis of the data would make it impossible to have a real time quantitative measurement.

Shack-Hartmann wavefront sensing

Shack-Hartmann wavefront sensing was introduced in 1994 [59] in vision science, following its establishment in astronomy. It soon became a method of preference, due to its reliability, simplicity to implement, and the relatively small amount of processing required. This technique is of particular interest for us, since it was used in the study presented in this Thesis; therefore some more details will be given here. The technique relies on the sampling of the aberrated wavefront with a lenslet array placed in a conjugated plane of the pupil where the wavefront error is to be measured. Each lenslet focusses the locally deviated wavefront onto a camera (typically a CCD camera) placed in its focal plane. Geometric rays are perpendicular to the wavefront, therefore if the wavefront is locally approximated by a titled plane, the displacement of each spot measured with respect to a reference is proportional to the local slope of the wavefront. Figure 2.1 illustrates this method. A plane wavefront gives an evenly spaced grid of focal points, while an aberrated wavefront creates a disordered grid (the figure only gives a schematic in one dimension).

The wavefront error can be reconstructed from the first derivatives

$$\begin{cases} \left.\frac{\partial W(x,y)}{\partial x}\right|_{x=x_i,y=y_i} = \frac{\Delta x_i}{f} \\ \left.\frac{\partial W(x,y)}{\partial y}\right|_{x=x_i,y=y_i} = \frac{\Delta y_i}{f} \end{cases} \tag{2.1}$$

with i the lenslet considered, f the focal length of the lenslet, and Δx_i, Δy_i the displacements of the focal spots as measured behind that lenslet on the CCD camera. $\left.\frac{\partial W(x,y)}{\partial x}\right|_{x=x_i,y=y_i}$ and $\left.\frac{\partial W(x,y)}{\partial y}\right|_{x=x_i,y=y_i}$ are the averaged partial derivatives of the wavefront error over the lenslet area. Recalling the decomposition of the wavefront in

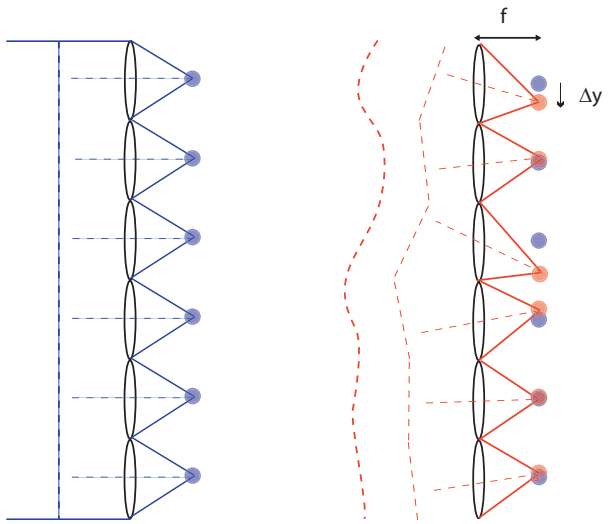

(a) Plane wavefront (b) Aberrated wavefront

Figure 2.1: 1D schematic of the measurement of the wave deformation with a Shack-Hartmann sensor.

polynomials, as given in Equation 1.1, it can be noted that the reconstruction can be computed through the Zernike derivatives, for example. The displacements themselves are measured using the centroids of the spots. An estimation of the centroids position (cx_i, cy_i) is given by

$$\begin{cases} cx_i = \frac{\sum x_j I_j}{\sum I_j} \\ cy_i = \frac{\sum y_j I_j}{\sum I_j} \end{cases} \tag{2.2}$$

where j represents a pixel of the area subtended by the lenslet, x_j and y_j are the x and y coordinates of this j^{th} pixel and I_j is the intensity at this same pixel.

Several issues of the Shack-Hartmann wavefront sensing technique should be considered. Sensitivity and dynamic range are determined by the design of the device and inevitably compete against each other, hence the design must be prepared carefully for a certain application. Furthermore, errors in the wavefront measurement originate from two problems: the fitting error imposed by the limited sampling of the wavefront by the lenslets, and the propagation of the centroiding error in the wavefront reconstruction. The fitting error is dependent on the lenslet sampling geometry and the wavefront statistics; concerning ocular aberrations, the statistics can only be estimated from population studies obtained so far. As for the actual centroid measurement, it is prone to several sources of errors. Measurement noise arising from photon noise and electronic noise of the camera has been well described in the literature [60]. Photon noise is due to the limited number of photons passing through

each lenslet; readout noise is the standard deviation of a random signal introduced by the electronics of the detector. Ocular wavefront sensing images are also degraded by several sources of spatial noise, which in turn add to the centroiding error. Waveguiding properties of the photoreceptors (the Stiles-Crawford effect described earlier) induce a Gaussian irradiance distribution in the pupil plane. Bará showed that this irradiance variation is non-negligible within each subaperture if using a 37 lenslet grid over the pupil; he evaluated a bias in the wavefront calculation in the order of 5-10% [61]. Retinal scattering also contributes to non-uniformity of the irradiance distribution, in particular producing a halo around the central core of the spot images on the CCD [62]. Moreover, when coherent light is used to illuminate the retina as is often the case in ocular wavefront sensing, speckle is produced by the interference of light scattered from different locations within the three dimensional retinal tissue and adds to the noise on the focal spots sensed by the camera. These scattering effects are dependent on the wavelength, the photoreceptor size and the polarization state of the light [58, 29]. The error is a complex issue: it is not systematic as the irradiance distribution varies with the eye movements, and the focal spot irradiance profile can be greatly affected in particular by speckle. Eye movements can average the noise over long exposures, but other types of spatial averaging are required to lower noise level with short exposures. One solution is to use short coherence light sources; another is to spatially average the noise by the use of a scanner or a rotating diffuser. The approach chosen by K. Hampson, who initiated the project, is the scanner, as was suggested by Hofer *et al.* [15]. After averaging, the spots are clean of speckle but they are also wider.

Finally, as was mentioned above, the measured wavefront is the result of an ocular double-pass. The problem was thoroughly studied by Diaz-Sanatana *et al.* who showed that for an averaged measurement (as is obtained with the methods mentioned above), the first-pass phase information loss is dependent on the scattering properties of the retina [58]. In the presence of a rough scatterer, the phase of the double-pass field, as measured by the Shack-Hartmann, does not contain information of the first-pass deformations. It raises the advantage of the technique as compared to the double-pass intensity measurement which keeps a memory of this information, as explained earlier. At the fovea, it can be considered that the difference between a symmetric double-pass wavefront error and a single-pass wavefront error lies beneath the resolution of the Shack-Hartmann. The problem is further reduced when using a very small entrance beam which will suffer from very small deformation. The performance for measuring ocular aberrations with the Shack-Hartmann has been assessed [63] and compared to other results obtained with psychophysical

techniques [64] or the Laser Ray Tracing method [65].

Other recent techniques

Other techniques implemented for ocular aberrometry include pyramid wavefront sensing, a variation of the Foucault knife test, where a pyramid is placed in a conjugated focal plane, and intensity differences between the images obtained can be related to the derivatives of the wavefront error. Several groups [66, 67] showed the feasibility and flexibility of such a sensor applied to ocular wavefronts. Interferometric techniques such as lateral shearing interferometry should be mentioned as they were recently tested to measure phase errors introduced by the tear film [68]. Curvature sensing is another method whereby the wavefront error Laplacian is retrieved through measurements of local changes in intensity in planes perpendicular to the light's propagation direction. Similarly to interferometric methods, it has the potential for higher resolution than Shack-Hartmann wavefront sensing [69, 70]. Finally, wavefront error modes can be selectively detected through the use of complementary holographic phase plates; this is the concept of so-called modal wavefront sensing [71].

2.2 Wavefront correction in the eye

Wavefront correction is possible once wavefront sensing is achieved. A deformable element is used to compensate for the measured aberrations. Figure 2.2 illustrates a typical ocular AO system that can be used for enhanced vision or retinal imaging. A coherent light source produces a plane wavefront which enters the eye, focusses on the retina and is reflected back through the whole pupil. The distorted wavefront is measured by the sensor and corrected automatically by the deformable optical element. The wavefront corrector needs to be conjugated to the wavefront sensor for exact correction of the wavefront aberrations, since the phase error changes with the propagation of the beam. They are also both conjugated to the pupil of the eye, which is the pupil of the whole system. In these planes, the size and location of the beam in independent of the present aberrations. An object seen through the system is aberrated by the corrector in such a way that it compensates for the aberrations of the eye; the final image is free of aberrations. Inversely, the system can provide a diffraction-limited image of an object at the back of the eye (photoreceptors for example).

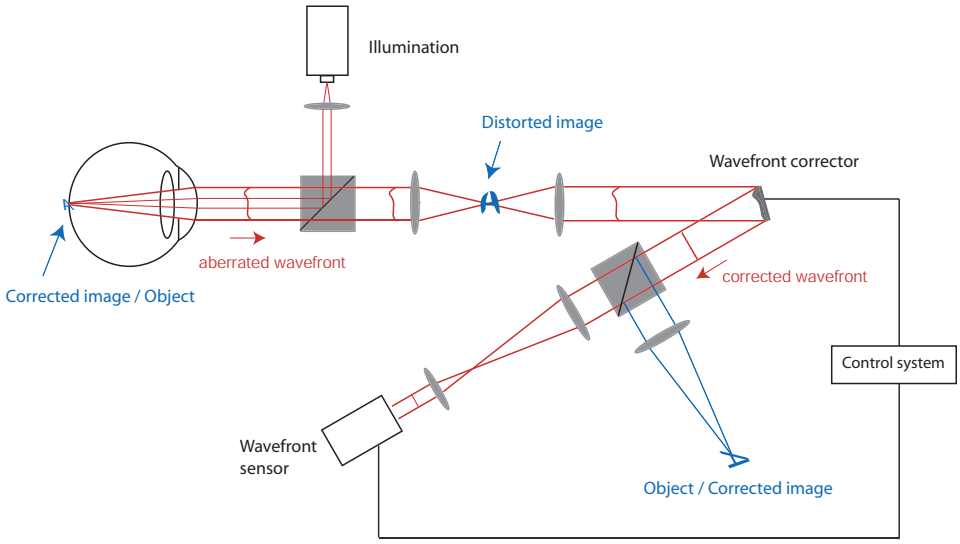

Figure 2.2: Schematic of an AO system for the eye.

Correcting devices

The spatial resolution of the correction is given by the number of actuators of the correcting device and the width of their influence functions, while the amplitude of correction is limited by its stroke. The temporal response of the corrector is another important parameter, although most correctors are well suited for ocular AO as we will see.

Several types of correcting devices have been developed and implemented in the adaptive optics field. With efficient electro-mechanical coupling, high accuracy and stability, piezoelectric actuators have been used widely in astronomy to build deformable mirrors, classified into segmented and continuous facesheet mirrors [60]. The most common actuator material is lead zirconium titanate (PZT). Figure 2.3 gives a schematic of a segmented mirror and a continuous facesheet mirror; other continuous facesheet mirrors are illustrated in the next chapter. With a discrete structure,

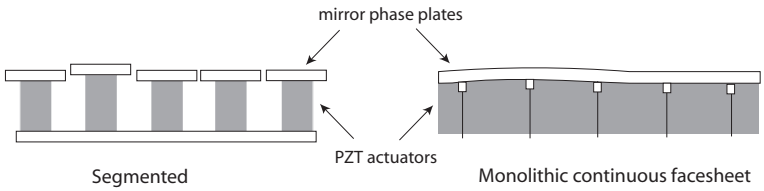

Figure 2.3: Schematics of a segmented and a monolithic continuous facesheet piezoelectric mirrors.

segmented mirrors can offer fine spatial resolution, provided a sufficient number of

actuators to counterbalance fitting errors. The fitting is further improved with actuators individually providing tip and tilt as well as piston deformation. The segments are easily assembled and repaired, but a disadvantage is that they create diffraction effects at their edges. Continuous mirrors can have more of a modal behavior and their fitting performance rapidly decreases with the spatial order of the aberrations to be corrected; however, for low order modes, they require several times less elements than piston-only segmented mirrors, and about the same as piston/tip/tilt segmented mirrors [60]. Different configurations exist: the facesheet can be directly actuated through bonded electrodes, these mirrors are called monolithic; when two wafers are bonded together they form a bimorph mirror; finally the facesheet can be deformed indirectly through the push-pull effect of a stacked array of actuators (so-called stacked actuator mirrors). Such mirrors, initially developed for the astronomy community, have been used in ocular AO systems by different groups, in a stacked actuator [2, 72, 73] or bimorph [74, 75] configuration, but their high cost is often a problem. Membrane mirrors form another type of continuous deformable mirrors: the membrane is in this case attracted by electrostatic effect [76]. Compared to piezoelectric mirrors, electrostatic mirrors have no hysteresis. Due to their low cost, these mirrors are popular in the vision community [77, 16, 18, 78, 79]. A finer spatial resolution can be obtained with microelectromechanical system (MEMS) mirrors; these miniaturised membrane mirrors indeed exhibit a zonal behavior and have been tested for the correction of higher-order ocular aberrations [80, 81]. Magnetic mirrors are also being developed, and hold the promise to provide vision scientist with an affordable very high stroke [82]. Finally, liquid crystal spatial light modulators (LCSLM), similarly to segmented mirrors, have the potential to offer very fine spatial resolution. In these components, the optical path length is locally changed due to the effect of an electric current on the orientation of the molecules of the crystal. However, they can only be used with monochromatic sources, which is often a disadvantage although it can help optimising the amplitude of correction with phase wrapping techniques. Another drawback refraining their use in AO systems is their slow temporal properties [83, 84].

Although many correcting devices have been implemented in ocular AO systems, there has been no demonstration of what technology is the most appropriate for ocular aberrations and what number of actuators and stroke are necessary for such application. The next chapter is devoted to the comparison of several continuous deformable mirrors for this particular task.

Wavefront fitting

Wavefront reconstruction itself is not strictly necessary for the correction, as long as the sensor is referenced to a plane wavefront and calibrated to the deformation introduced by the corrector. The control system translates the signal detected by the sensor into a command which is sent to the corrector. The computation is done with a matrix **B**, built such that each of its column vector characterizes the effect of each individual actuator of the corrector on the sensor. The sensor and the corrector are related by the expression

$$\mathbf{s} = \mathbf{B}\mathbf{c} \tag{2.3}$$

where **s** is the measurement given by the wavefront sensor and **c** is the command sent to the mirror. The signal after correction can be expressed as

$$\mathbf{s} = \mathbf{s}_0 + \mathbf{B}\mathbf{c} \tag{2.4}$$

with $\mathbf{s}_0$ the initial signal. Expressing the command to be sent from the signal measured implies inverting **B**. The matrix is not usually invertible, hence a best fit is used instead. A common strategy is to minimize the squared signal error which is a good measure of the correction error. The resulting controller **C** is the least-square reconstructor, also called pseudo-inverse $\mathbf{B}^{-1*}$of **B**. It can be calculated using the singular value decomposition

$$\begin{aligned} &\mathbf{B} = \mathbf{U} \times \mathbf{W} \times \mathbf{V}^{\mathrm{T}} \\ &\Rightarrow \mathbf{C} = \mathbf{B}^{-1*} = \mathbf{V} \times \mathbf{W}^{-1} \times \mathbf{U}^{\mathrm{T}}. \end{aligned} \tag{2.5}$$

The column vectors of **U** and **V** represent orthogonal sets of the system modes in the sensor base and the mirror base respectively. Their dimensions are given by the numbers of signals and actuators (degrees of freedom). The total number of modes is the smaller of these two numbers. **W** gives the singular values, or the gain of the system for each mode: the lower the singular value, the less responsive the system for that particular mode and the bigger the command to be sent. Therefore the modes associated to the smallest singular values are also the modes the most sensitive to noise. These are usually discarded, and a compromise must be found between spatial resolution and stability of the system. The number of modes can also be reduced to avoid saturation, when the stroke of the corrector is not sufficient for the wavefront error correction.

The least-square reconstruction does not take into account measurement noise propagating through the system and is thus a simplistic approach. An optimized

reconstruction can be derived considering the actual phase error,

$$\Phi = \Phi_0 + \mathbf{Mc} \tag{2.6}$$

with $\mathbf{M}$ the corrector influence matrix. This matrix characterizes the phase deformation introduced by the corrector and can be experimentally calculated measuring its influence functions, or phase deformations introduced by each actuators. The noise $\mathbf{n}$ on the wavefront sensor signals is also taken into account along with the sensor response matrix $\mathbf{S}$

$$\mathbf{s} = \mathbf{S}\Phi + \mathbf{n}. \tag{2.7}$$

Minimizing the squared wavefront error leads to a solution dependent on the aberration statistics, the noise statistics, the mirror influence matrix and the sensor response matrix, as first proposed by Wallner [85]. Assuming the noise is independent from the incoming wavefront, zero-mean, independent identical Gaussian within each lenslet ($\langle \mathbf{n}\mathbf{n}^{\mathrm{T}} \rangle = \sigma_{\mathbf{n}}^2 \mathbf{I}$), the optimal reconstructor can be expressed as

$$\mathbf{C} = -[\mathbf{M}^{\mathrm{T}}\mathbf{M}]^{-1}\mathbf{M}^{\mathrm{T}}\langle \Phi\Phi^{\mathrm{T}} \rangle \mathbf{S}^{\mathrm{T}} \left[\mathbf{S}\langle \Phi\Phi^{\mathrm{T}} \rangle \mathbf{S}^{\mathrm{T}} + \sigma_{\mathbf{n}}^2 \mathbf{I} \right]^{-1}. \tag{2.8}$$

If the statistics are Gaussian, the solution is the maximum likelihood. In astronomy, the Gaussian statistics of the turbulence are well known, and the maximum likelihood reconstructor can be derived. To the author's knowledge, such reconstructor has never been used in ocular AO.

Closed-loop system

Because the corrector is placed before the sensor, the correction is continuously reassessed and adapted. The temporal behaviour of such a closed-loop system is of importance since time parameters of the AO system are of comparable timescale to dynamics of the ocular aberrations. The parameters include the exposure duration over which the sensor signals are integrated, and the readout and calculation times introducing delays in the system. At the time the correction is applied, the actual wavefront error may have changed.

The temporal response of a closed-loop system can be modeled from the knowledge of its components, usually through Laplace transforms

$$F(s) = \mathcal{L}[f(t)] = \int_0^\infty f(t)e^{-st}dt \tag{2.9}$$

where s is the complex frequency, $s = \sigma + i\omega$. Laplace transforms greatly simplify the algebra of differential and integration operations such as those encountered in closed-loop systems. The steady-state frequency response, given by the transfer function evaluated at $s = i\omega$, provides useful analysis of the system. In particular, considerations upon bandwidth and stability can be made through the analysis of the open-loop transfer function, closed-loop transfer function and error transfer function (ratio of the closed-loop transfer function by the open-loop transfer function). Figure 2.4 gives a schematic of the closed-loop system, using classical block-diagram representation. A thorough description of each component can be found in the literature [60].

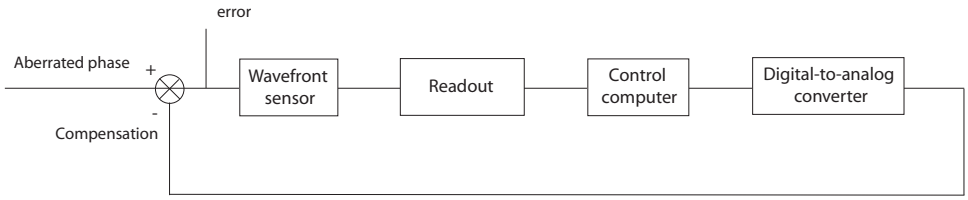

Figure 2.4: Block-diagram representation of an AO system.

The control computer temporal response can be adjusted to ensure stability of the system while optimizing its bandwidth. A simple integrator is one solution: the correction is iteratively calculated from the previous correction and the current phase error

$$\mathbf{c}_i = \mathbf{c}_{i-1} + g \times \mathbf{B}^{-1*}\mathbf{s}_i, \tag{2.10}$$

the parameter g being the gain of the system. Optimal gain can be computed from the mentioned frequency analysis, although it usually needs to be adjusted experimentally in vision science. Hofer *et al.* [86] found a good agreement between predicted and experimental optimal gain for their ocular AO system. The gain can also be adjusted separately for each mode of the system, as proposed by Gendron *et al.* [87]. A simple integrator control law may not always be the best suited and optimized predictive controls can be derived from the temporal statistics of the aberrations, such as for the turbulence [88, 89]. Again, the implementation of this optimization is more difficult in vision science due to the non-stationarity of the ocular aberrations. The dynamics of the aberrations yet need to be well understood and characterized before a more complex control law is designed.

2.3 Developments and applications of adaptive optics for vision science

Ocular AO current status

The first complete AO system was presented by Liang *et al.* [2] in 1997, based on a Shack-Hartmann sensor and a piezo-electric mirror. The following year, the performance of a system, incorporating a double-pass intensity wavefront sensor and a liquid-crystal spatial light modulator as the corrector, was evaluated [83]. Both these systems were used in a static regime, although the correction was achieved through several iterations. Since then, several systems have been developed to operate at a 20-25 Hz frame rate [86, 90], in line with the required speed derived by Hofer *et al.* [15] from aberration dynamics measurements. Higher AO sampling rates have been reported [16, 74], which may show a benefit in using higher bandwidths for higher levels of correction. However, as Diaz-Santana *et al.* highlighted it, the required bandwidth is dependent on the AO system and the subject's aberrations dynamics [16]. The residual wavefront error reported is usually around 0.1 μm rms for different pupil sizes and gain, although this is highly subject-dependent. Considering the visible spectral bandwidth centered at 550 nm, this corresponds to a residual wavefront error rms of $\lambda/5 - \lambda/6$.

Although most of the recent AO systems for vision science are based on Shack-Hartmann sensors and deformable mirrors, a complete AO system incorporating a pyramid wavefront sensor [67] and one with a liquid-crystal corrector and an interferometric feedback [91] have been presented, although the latter has not yet been tested on real eyes. Another approach of adaptive optics for vision science has been developed using feedback based on the subjective evaluation of sharpness instead of a wavefront sensor [92]. Static correction has also been demonstrated through the manufacture of customized phase plates [93, 94]. Beside the manufacturing issues to exactly match measured aberrations, the dynamics of the aberrations yield a higher static residual wavefront error than with AO systems. Moreover, if applied to contact lenses, decentrations and tilts are important issues to be taken into account for this technique [95]. Wavefront-guided surgery has also been tested [96] but the technique is not fulfilling expectations, as significant higher-order aberrations are still introduced [97]. Finally, the concept of customized intra-ocular lenses is being investigated [98], but again, alignment is here critical. The idea was taken even forward with the study by Vdovin *et al.* [99] of a intraocular adaptive optics with remote con-

trol.

Recent developments of AO systems include the implementation of two deformable mirrors in one system to combine spatial resolution and stroke of the corrective elements for an optimised correction. Zawadzki *et al.* [100] used two mirrors conjugated to the pupil plane and showed a better correction obtained than with either of the two. The idea could be developed further for a dual conjugate adaptive optics system. When all aberrations are located within one plane, a correction in a conjugated plane is sufficient for a wide-field correction, while if the aberrations extend over a thicker layer (as is the case for the eye), a single corrector can only provide diffraction-limited correction for a limited field of view, the so-called isoplanatic patch. At further eccentricity, the correction worsens the aberration pattern which varies with eccentricity. One approach consists in optimizing the correction given by a single corrector for a certain field [101], but a better wide-field correction can be achieved with several sensors and correctors placed in different planes. This is the principle of multi-conjugate adaptive optics [102], and it has been analyzed for the ocular application [103].

Applications of ocular AO

As was mentioned earlier, the main application for adaptive optics has been retinal imaging. The first adaptive optics ophthalmoscopes [2, 86, 74] were followed by AO scanning laser ophthalmoscopy (SLO) [72], optical coherence tomography [75, 73] (OCT) and combined SLO-OCT systems [79]. They reported increased light collection in the imaging branches, leading to better sensitivity and resolution. Using AO SLOs, the research has focussed on imaging individual photoreceptors (for densimetric and trichromatic topography measurements) and blood flow, while AO OCT leads to a better depth resolution to visualize the different retinal layers (although the signals obtained with this technique are still being discussed) [104].

The application which is more of interest for ourselves is the ability to perform psychophysical experiments on vision, while controlling higher-order aberrations. Beyond the straightforward experiments on visual performance [2, 39], which is the topic of the Thesis, it is worth mentioning here other experiments that have been carried out. Some interest has arisen in the study of the role of higher-order aberrations in accommodation, but no conclusive results were obtained either for steady-state accommodation [78] or accommodation response [105, 106]. Other experiments can be described in terms of functional imaging, whereby photoreceptors are excited with a very well defined stimulus, and simultaneously imaged [107]. For example,

Hofer *et al.* [108] recently reported the delivery of monochromatic stimuli less than two microns full width at half maximum. Putman *et al.* showed that the locus of fixation could this way be precisely related to the cone density [109]. The spectral sensation [108] or the local defects [110] of photoreceptors can also be revealed more precisely with such techniques.

Chapter 3

Task-based Assessment of Deformable Mirrors for Vision Science

The wavefront corrector is a key element of an adaptive optics system. Apart from stroke and number of actuators, size and price are important parameters in the search for a compact and economic ocular AO system to be easily implemented in the laboratory or in clinical environment. Excluding a few examples with liquid-crystal spatial light modulators [83, 91, 84], most ocular AO systems reported include continuous deformable mirrors. Continuous mirrors seem well suited for the correction of the relatively low number of modes characterising ocular aberrations. In astronomical AO, typical empirical numbers indicate that piston-only segmented mirrors require four to eight times more actuators than continuous mirrors which in turn provide comparable or slightly better fitting than piston/tip/tilt segmented mirrors [111, 60]. A few studies recently attempted to derive the requirements of deformable mirrors for ocular AO. Doble *et al.* modeled continuous and segmented mirrors and showed that 11-14 actuators across would be sufficient for a stacked array actuator continuous mirror, while 50-90 actuators would be required for a piston-only segmented mirror in order to correct higher-order aberrations over a 7.5 mm pupil [112]. The latter number

would be reduced for piston/tip/tilt segments (9-12 actuators across). These results were based on a large population ocular wavefront measurements and extended the simulations presented by Miller *et al.* [113] over 12 subjects, which stated that 20×20 actuators could provide diffraction-limited correction for a 6 mm pupil. No mirror meeting such high requirements has yet been implemented in ocular AO systems, and amongst all the continuous mirrors tested, it is difficult to state which one is best suited for ocular applications. A study directly compared the in-vivo ocular correction given by two different deformable mirrors (a MEMS mirror and a piezoelectric mirror) over a 4.6 mm pupil and concluded on similar performance [80] for the three subjects tested. Given the variability of ocular wavefront aberrations in a normal population and the limited practicality of AO systems, statistical conclusions cannot easily be drawn from experimental measurements.

The study presented here aimed for a task-based assessment of commercially available continuous surface deformable mirrors, that is to simulate numerically the performance of these mirrors to correct typical higher-order ocular aberrations. Three mirrors were compared: the 37 element electrostatic micromachined membrane deformable mirror (MMDM) from OKO, the 19 element piezoelectric mirror from the same company, and the 35 element bimorph mirror from AOptix. The 37 element OKO MMDM has been implemented in several ocular AO systems [77, 16, 18, 78, 79], while the other two mirrors are more recent and have only been used by a couple of research groups [75, 67]. The mirrors were precisely characterized and the measured phase maps were used to fit Zernike polynomials and typical ocular aberrations. The results of this analysis have been published [114].

3.1 Deformable mirrors

The three mirrors investigated present different spatial characteristics in terms of optical diameter and actuator geometry, as can be seen in Figure 3.1. Actuator responses also differ because of the technology used for each mirror; a short description of the three mirrors is given. As the technologies referred to here have been used in astronomy for some time, more details can be obtained from reference books [111, 60].

The 37 actuator OKO MMDM

This mirror has already been described in several publications, and its behavior has been modelled [76]. It consists of a silicon nitride membrane suspended over an array

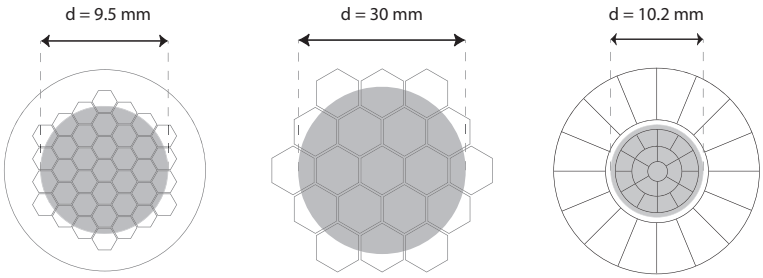

Figure 3.1: Actuators layout for the three mirrors considered: the 37ch OKO MMDM, the 19ch OKO, and the 35ch AOptix. The gray area represents the optical pupil typically used. It is defined as such by the manufacturer for the 19ch OKO and the 35ch AOptix mirrors, but set by the user for the 37ch OKO MMDM mirror.

of electrodes. The membrane is electrostatically attracted towards the 37 hexagonally arranged electrodes when a voltage is applied to them, as shown in Figure 3.2. The

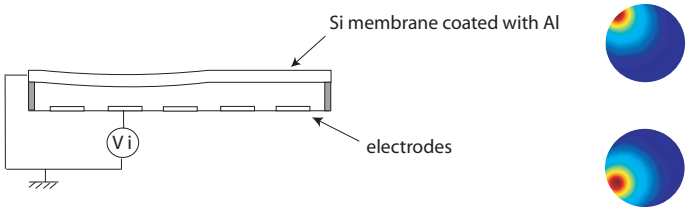

Figure 3.2: Schematic of the 37ch OKO mirror actuation and examples of actuator response.

surface deformation follows a quadratic dependance on the applied voltage, and this assumption was used in the performance simulations of the mirror. For the simulations, the optical pupil was reduced to about 2/3 of the mirror diameter, i.e. approximately 9.5 mm as shown in Fig. 3.1. This is a commonly accepted value, as the membrane is clamped to the edge, and we want to be able to correct for aberrations at the edge of the pupil [115]. The maximum stroke, measured as the difference between the deformation when the maximum voltage is applied to all actuators to that when no voltage is applied, was evaluated over this area to 3.5 μm peak-to-valley surface deviation with a commercial Twyman-Green interferometer. The single actuator stroke, corresponding to the maximum voltage applied to one actuator while the others are set to zero, was 500 nm. It should be noted that the mirrors of this series vary in characteristics such as optical flatness and distance between the membrane and the array of electrodes, so that the spatial performance evaluation given here is just an indication of typical performance.

The 19 actuator OKO piezoelectric deformable mirror

This new 30-mm mirror was recently manufactured by OKO Technologies. It integrates piezoelectric technology into a compact and relatively inexpensive device. The reflective quartz plate is piston-like deformed by the lead zirconium titanate (PZT) actuators when a voltage is applied. Furthermore, it only covers part of the outer ring of

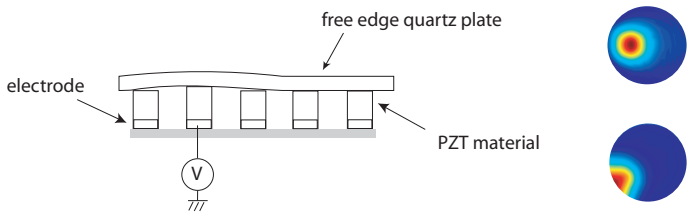

Figure 3.3: Schematic of the 19ch OKO mirror actuation and examples of actuator response.

actuators and it is not restricted at the edge. These features result in sharper influence functions and a larger stroke than for the membrane mirror: over the specified voltage range of -150V to 450V, the single actuator stroke was evaluated to 3 μm for the 7 inner actuators, and 6/8.5 μm for the outer ring. Due to a limitation of our power supply, the mirror behavior was measured over half the specified voltage range, but the values were extrapolated to the full specified range. The actuator response can be approximated to a linear curve; however the mirror exhibits hysteresis. Over the range

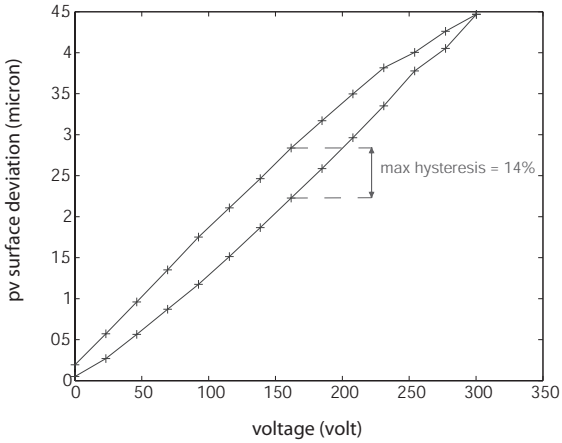

Figure 3.4: Measurement of hysteresis through the ramping of one actuator.

0 to 300V, the hysteresis was measured up to about 14% of the total deformation, as can be seen on Fig. 3.4. The hysteresis effect was ignored in the present study, since the spatial characterization measurements cancelled it out as explained in Section 3.2.

The 35 actuator AOptix bimorph mirror

The AOptix mirror consists of two layers of ceramic lead magnesium niobate (PMN) which are directly actuated by the electrodes bonded on the materials. PMN material deforms when an electric field is applied to it, similarly to PZT, but it differs to it in that the deformation is independent of the polarity of the field, and only 2% hysteresis is present at room temperature. The two layers are bonded together with a grounded electrode, and the other electrodes are mounted on the back and front face of the mirror. The front face electrode cannot be driven fast due to its high capacitance, hence it is used to produce the overall defocus. A guard ring, which limits the optical

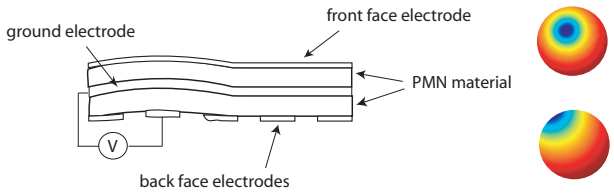

Figure 3.5: Schematic of the 35ch AOptix mirror actuation and examples of actuator response.

pupil (see Fig. 3.1), separates the actuators in two groups: the inner actuators produce a curvature deformation while the outer ones are referred to as slope actuators. The

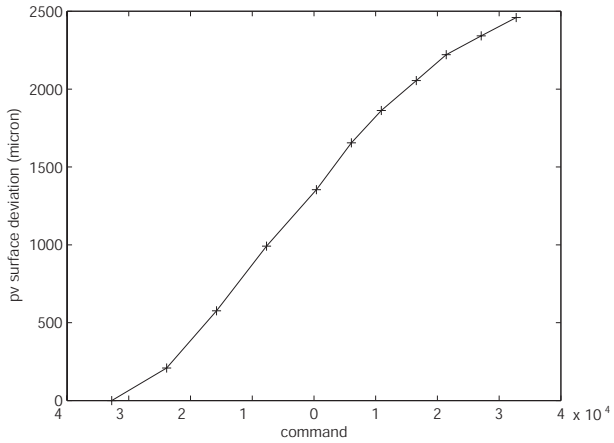

Figure 3.6: Measurement of response through the ramping of one actuator.

total stroke of the mirror is about 18 μm, and the individual stroke of the actuators varies from 3 μm for the 19 inner actuators, to 7 μm for the outer ring of actuators. These values are very similar to those measured on the piezoelectric OKO mirror. The actuator response to the voltage applied is not linear, as shown by Horsley *et al.* [116], but there was an attempt to correct for it in the software provided by the company.

Figure 3.6 shows the surface response of a single actuator driven by the commands of the software and not the voltages; the curve is approximately linear, except at the extremities of the full range.

3.2 Simulation method

Least-square phase fitting

The spatial analysis performed over the mirrors was based on the least-square fitting of specified phase maps. We will describe here the process followed step-by-step and discuss the practical issues. The first step was to record each particular deformation produced by the actuators, the so-called influence functions (IF) as illustrated in the previous section. In order to obtain precise phase maps, a commercial $FISBA^{©}$ Twyman-Green interferometer was used. Each phase map was evaluated over the optical pupil as illustrated by Figure 3.1, from the difference of two measurements of the same actuator, and normalised by the range of voltages used. The piston terms, taken as the the average of the values in the images, were removed from the phase maps before all the IFs were stored in a matrix $\mathbf{M}$.

A singular value decomposition (SVD) of $\mathbf{M}$ made it possible to obtain an orthogonal basis over which the wavefronts could be projected

$$\mathbf{M} = \mathbf{U}\mathbf{W}\mathbf{V}^{\mathrm{T}}. \tag{3.1}$$

The decomposition defines $\mathbf{U}$ and $\mathbf{V}$ as orthogonal sets of the mirror modes: $\mathbf{U}$ contains the phase maps and $\mathbf{V}$ the corresponding command sets. $\mathbf{W}$ gives the singular values: the smaller the singular value, the less responsive the mirror and the larger the commands needed to be sent for a unit mode amplitude. We will see later how these singular values are important to avoid clipping of the mirror. The process is similar to the least-square wavefront fitting described in the previous chapter, except that here the wavefront sensor signals are replaced by the interferometer pixelated phase maps. The information contained in $\mathbf{M}$ can be of much higher resolution.

Any phase Φ can be projected on this finite base, and the residual wavefront gives us an evaluation of the fitting efficiency of the mirror. The projection is mathematically expressed by

$$\Phi_m = \mathbf{U}\mathbf{U}^{\mathrm{T}}\Phi. \tag{3.2}$$

The parameter used to determine the fitting error was the root-mean-square (rms)

of the wavefront difference between Φ and Φ_m. It should be noted here that this projection does not take into account the limited range of commands available for the mirror. Hence it is necessary to simultaneously work on the corresponding commands and make sure they remain within the range available. The set of commands $\mathbf{c}$ is recovered with the pseudo-inverse $\mathbf{M}^{-1*}$, which can be calculated using the SVD,

$$\mathbf{c} = \mathbf{M}^{-1*}\Phi = \mathbf{V}\mathbf{W}^{-1}\mathbf{U}^{\mathrm{T}}\Phi. \tag{3.3}$$

A code was written in IDL to process the phase maps and perform the phase fitting.

Typical ocular wavefronts

Unlike astronomical adaptive optics, ocular adaptive optics suffers from the lack of a model of the wavefronts to be corrected. The wavefronts are not spatially stationary and there is no simple theory, such as Kolmogorov theory for turbulence. However there has been several extensive studies (on more than 100 eyes) resulting in experimental statistics. Thibos *et al.* measured the ocular aberrations of 200 young well-corrected eyes with a Shack-Hartmann sensor and decomposed the wavefronts over 36 Zernike polynomials [10]. This number of coefficients can be accepted as sufficient to describe ocular wavefronts [15]. The statistical characteristics of ocular wavefronts, in terms of mean and covariance matrix of the Zernike coefficients, were calculated from the measurements [117]. Typical ocular wavefronts can be generated using a MATLAB model containing these statistics.

Attention should be paid to the fact that these wavefronts were measured after sphero-cylindrical correction with a step size of 0.25 D. The population mean values for defocus and astigmatism after correction were not however equal to 0 due to the fact that the refraction was adjusted subjectively. Thibos argues that these findings can be explained by the Stiles-Crawford effect which results in a pupil apodization of the wavefront aberrations affecting subjective refraction, while this apodization is not taken into account by the Shack-Hartmann sensor. The objective plane of best focus determined by the aberrometer may then differ from the focus given by the rays going through the centre of the pupil. This explanation can be complemented by the observation that, combined with higher-order aberrations, a non-zero defocus term can yield a better MTF, even excluding any pupil apodization [39]. Thibos measured residual defocus and astigmatism aberrations means of about 0.25 D and 0.15 D respectively over a 6 mm pupil (i.e., 0.33 μm and 0.2 μm wavefront error rms). Second-order aberrations are very important in ocular aberrometry, because if left

uncorrected they account for about 90% of the total wavefront error rms [9], while if corrected subjectively they are left with a magnitude similar to that of the higher-order aberrations (the mean higher-order wavefront error rms in this study was about 0.3 μm). Refractive errors have therefore large impact on the total wavefront error, hence on the required mirror stroke. The present study was based on such residual refractive errors, which are quite typical, and similar to the residual that resulted from sphero-cylindrical correction in the AO system used in our project.

3.3 Results

3.3.1 Generation of Zernike polynomials

The Zernike polynomials are widely used to decompose ocular wavefronts. Therefore, we started the simulations working on these defined phase maps. For each normalized Zernike polynomial, the corresponding vector of commands was calculated using Equation 3.3. It was then rescaled so that the commands would cover half the range of available voltage. Multiplying this new vector by the matrix $\mathbf{M}$ again gives the maximum signed best Zernike fit $\mathbf{z}_m$, meaning that the mirror will be able to produce the phase deformation $\pm\,\mathbf{z}_m$. This is equivalent to rescaling the projected wavefront

$$\mathbf{z}_m = \frac{c_{lim}}{c_{max}}\mathbf{U}\mathbf{U}^T\mathbf{z} \tag{3.4}$$

where c_{lim} is the maximum command applicable, and c_{max} is obtained as follows:

$$c_{max} = \max(|\mathbf{M}^{-1*}\mathbf{z}|). \tag{3.5}$$

Since the matrix $\mathbf{M}$ had been normalized before the SVD, the command range is 1, and the maximum signed command applicable c_{lim} is $\pm$ 0.5.

Figure 3.7 shows the maximum peak-to-valley (pv) of the Zernike fit obtained with the three mirrors considered. The Zernikes are ordered according to the OSA/VSIA Taskforce conventions [6]. The peak-to-valley values represent the signed amplitude of the biggest possible wavefront deformation of the mirror for each considered Zernike, taken as a difference between the minimum and the maximum pixel values. Since these absolute values are calculated from the first saturation of any actuator, they are very sensitive to noise. Therefore, the rms deformations of the same wavefronts are also plotted, in Figure 3.8(a). These figures are calculated from all the values in the pupil, and can be considered as more representative, even if still affected

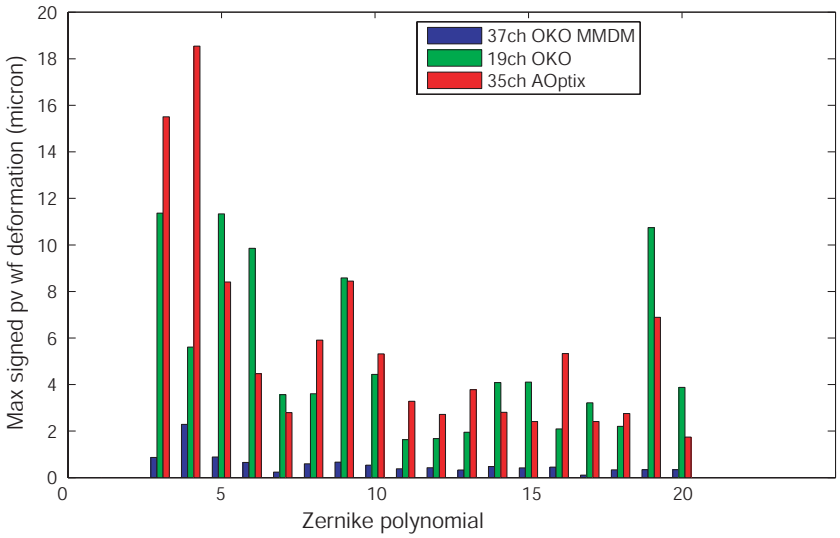

Figure 3.7: Comparison of the Zernike generation for the three mirrors in terms of pv signed wavefront produced. The first 21 polynomials excluding piston, tip and tilt, are represented.

by noise. Moreover, they are equivalent to the Zernike coefficients according to the OSA/VSIA Taskforce, and can be directly related to the wavefront decomposition. Figure 3.8(b) shows the rms wavefront error for each Zernike fit, taken as the difference between the Zernike polynomial phase map and the projected one, at maximum amplitude. The rms error should be analyzed along with the maximum rms value, not to over-estimate it: Fig. 3.8(c) represents the rms wavefront error fit (values of Fig. 3.8(b)) divided by the maximum Zernike coefficient (values of Fig. 3.8(a)), which we will refer to as the normalised rms error.

It appears from these plots that the 19 actuator OKO mirror and the 35 actuator AOptix mirror have comparable stroke concerning Zernike generation. The difference arises in the fitting, since the piezoelectric mirror shows a higher normalised rms error than the bimorph. For both mirrors, the normalised rms error generally follows a linear increase with the radial order, with a higher slope for the piezoelectric mirror. The fitting error for the 19ch OKO goes up to 40% for the higher Zernike orders, while for the AOptix, it is consistently less than 24%. It can be noted that the normalised rms error follows an interesting trend: for each Zernike polynomial order, the fitting is worse at minimum azimuthal frequency (except for defocus). This trend seems to be also present on the values of the 19ch OKO mirror, although not as marked. The relatively low performance of the 37 actuator MMDM can be attributed to its limited stroke and the large coupling between actuators. In particular, it can be noted that although the total stroke of the mirror was measured to be 3.5 μm (see

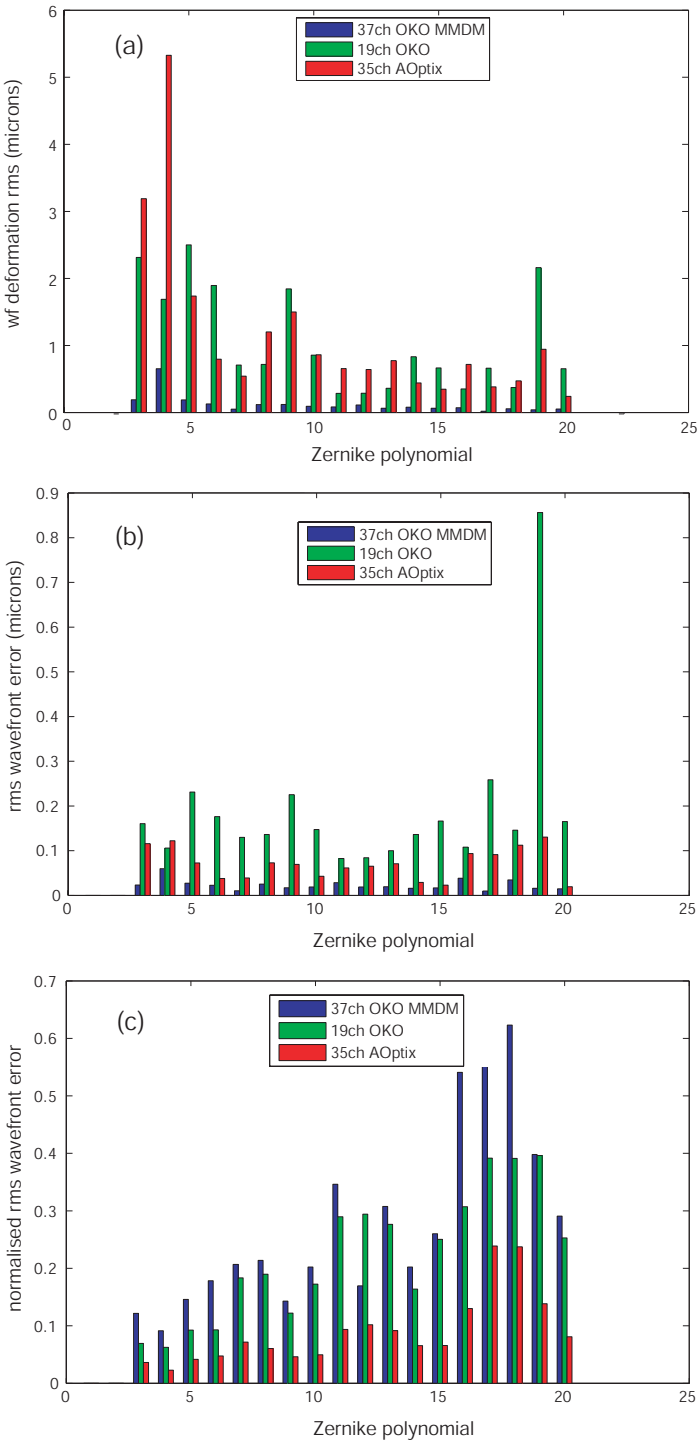

Figure 3.8: Comparison of the Zernike generation for the three mirrors: (a) in terms of maximum signed wavefront rms, (b) in terms of residual rms error and (c) in terms of normalised wavefront error (residual wavefront error rms over maximum signed wavefront rms).

Section 3.1), the simulated defocus signed wavefront deformation (corresponding to the total surface displacement) does not exceed here 2.2 μm pv. A similar comparison between the peak-to-valley simulated defocus term of the AOptix mirror and the measured stroke shows on the other hand very good consistency.

The results presented here are in agreement with previous studies carried out on the 37 actuator OKO and the 35 actuator AOptix mirrors. Fernández *et al.* [77] displayed the range of production of Zernike polynomials by the 37 actuator OKO mirror, as the total peak-to-valley surface displacement (equivalent to the signed wavefront deformation as presented here). Their calculations were based on simulated IFs of the mirror, which probably can explain why our values are lower (up to 40%). Also, they used only 12 mirror modes to generate these Zernikes. The best appropriate number of modes is usually hard to define, and varies with the application. Using a limited number of modes in our simulations resulted in higher Zernike amplitudes, but also considerably higher rms errors. We decided to further investigate this issue only for the correction of typical ocular wavefronts (Subsection 3.3.2). Regarding the results presented by Fernández, the overall same features are nevertheless observed, with a produced defocus term twice as big as the astigmatism terms, and a fast decrease of performance for the higher terms. For the AOptix mirror, the results for the signed Zernike surface displacements (equivalent to half of the signed wavefront deformations) presented by Horsley *et al.* [116] are again consistent with our figures. They measured the mirror IFs using a phase-shifting interferometer. As they pointed out, the second order terms reach very high values, and the values might even be under-estimated when the saturation is only due to one actuator (second term of astigmatism, and first term of trefoil for example in our case). Although the stroke decreases with the radial order, the signed wavefront peak-to-valley still remains above 2 μm for the higher-order aberrations. The same comment can be made on the 19 actuator OKO mirror.

The Zernike decomposition, as any other orthogonal expansion, is useful to describe wavefronts, but is by no means necessary in the correction process. In fact, real adaptive optics control systems do not use Zernike modes. Only an infinite number of Zernike polynomials would represent a complete wavefront base, hence using a limited number induces approximations. The combined mirror performance over the Zernike polynomials might not be representative of its performance over wavefronts as a whole, not only because of these approximations but also because the Zernikes produced by the mirror are no longer orthogonal. These issues point out the importance of a direct study on typical ocular wavefronts.

3.3.2 Correction of typical ocular wavefronts

The ocular wavefronts fitting was done as the following. Recalling the previous procedure described, the commands were first calculated using Equation 3.3. To take into account the limited range of the mirror, the vector obtained was modified so that each out-of-range channel was clipped to the maximum value permissible. The final fit phase is given by

$$\Phi_m = \mathbf{U}\mathbf{W}\mathbf{V}^T f(\mathbf{V}\mathbf{W}^{-1}\mathbf{U}^T\Phi) \tag{3.6}$$

where $f(c_i)$ is the clipping function defined by

$$f(c_i) = \begin{cases} c_i & \text{if} \quad -c_{lim} \leq c_i \leq c_{lim} \\ c_{lim} \times \frac{c_i}{|c_i|} & \text{if} \quad c_i < -c_{lim} \quad \text{or} \quad c_i > c_{lim}. \end{cases} \tag{3.7}$$

If no actuator is out of range, Equation 3.6 collapses to the simple projection expression (Eq. 3.2).

A sample of 100 generated ocular wavefronts over a 6 mm pupil were processed using these formulae, and the residual rms wavefront error after fitting was plotted on Figure 3.9. These results were obtained with a reduced number of modes, chosen

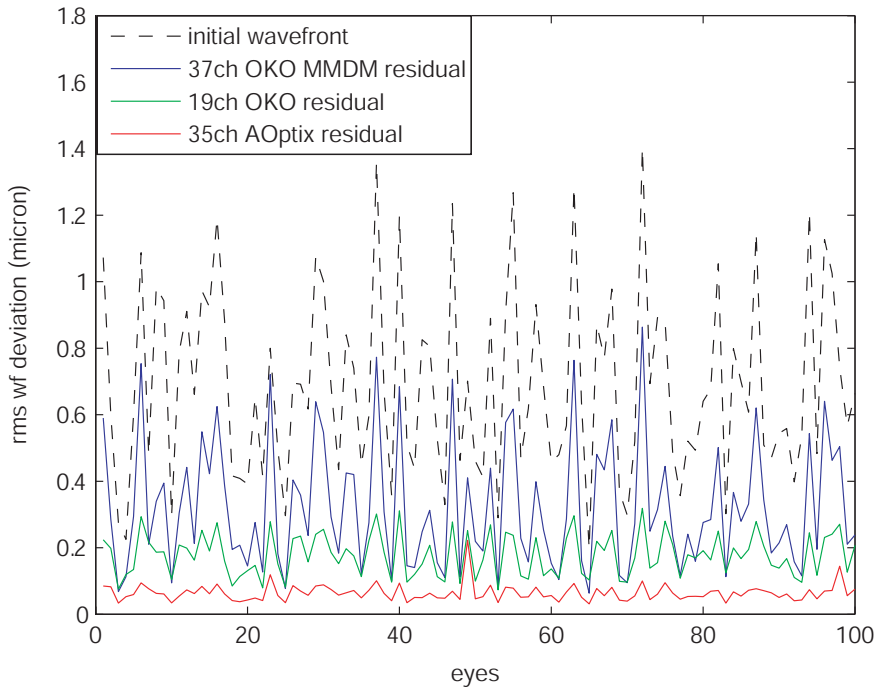

Figure 3.9: Residual wavefront error rms after fitting with the three mirrors over a 6 mm pupil. Piston, tip and tilt terms were removed.

to optimise the correction (i.e. lowest rms error). The matrices **U**, **V** and **W** were simply truncated to the selected modes. Figure 3.10 displays the average residual rms error for the same initial wavefronts according to the number of mirror modes used. As was recalled in the last section, the smaller the singular value, the more sensitive

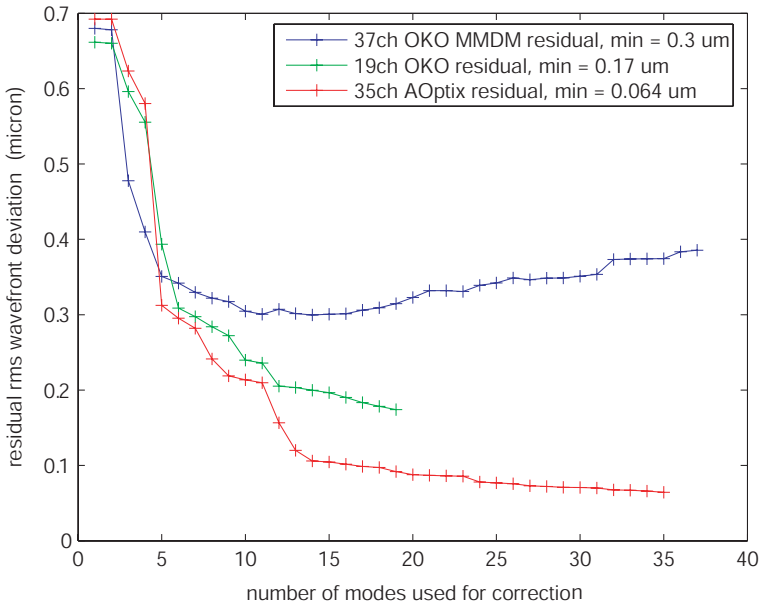

Figure 3.10: Residual rms wavefront error after fitting with the three mirrors. The results were averaged from calculations on the same initial wavefronts as in Fig. 3.9.

the mode. Such "noisy" modes are more likely to make the actuators saturate, and hence degrade the performance of the mirror. This effect is particularly highlighted by the 37 actuator OKO curve, which has a much smaller stroke than the two others as was shown earlier. On the figure, it can be seen that the mirror starts saturating with about 15 modes. At this point, the radial order of correction is reduced, but the overall wavefront approximation is better than with a higher number of modes. Indeed, distributing the command over a larger number of modes is done at the expense of the lower order modes. On the contrary, the 35 actuator AOptix mirror has a sufficient stroke so that the performance improves as more and more modes are used. In fact, a clipping of one of the actuators or more was observed for only 5 wavefronts out of 100 when using 35 modes for the correction. As for the 19 actuator OKO, the figures presented here are in agreement with the analysis performed on the Zernike polynomials: although the stroke of the piezoelectric mirror is comparable to that of the bimorph mirror, the fitting is not as good, probably due to the smaller number of actuators. As was said earlier, the figures plotted were extrapolated from the measurements to simulate the performance of the mirror over the voltage range -150V to

+450V. Nevertheless, the performance of the mirror over such typical ocular wavefronts was almost not noticeably affected by a reduction of the range to 0V-300V. In fact, it only affected the performance with correction of the correction using all modes of the mirror. When limited to the range 0V-300V, the mirror exhibits saturation, and the residual rms wavefront error goes up to 0.22 μm instead of 0.16 μm. The performance with 18 modes is however the same.

The results concerning the 37ch OKO MMDM can be compared to those presented recently by Kennedy and Paterson [118] in a comparison of several MEMS mirrors. They used a model of the mirror in good agreement with experimental measurement, and simulated the performance for ocular wavefront aberrations using the same statistics from Thibos *et al.* as we used. They presented the results in terms of Strehl ratio, for different ocular pupil and mirror pupil diameters. For a 6 mm ocular pupil and the mirror effective pupil we used, they found a mean Strehl ratio of about 0.1, which is more than the conversion in Strehl ratio calculated from our wavefront error rms. They did however remove defocus and astigmatism from the initial ocular wavefronts. We performed further simulations with the exact same conditions, and found a minimum wavefront residual rms error $\sigma = 0.14$ μm which converts to a Strehl ratio S of 0.145 using the formula

$$S = \exp\left[-\left(\frac{2\pi\sigma}{\lambda}\right)^2\right] \tag{3.8}$$

with $\lambda = 0.633$ μm. Both results are therefore very similar although Kennedy and Paterson simulated the mirror and used Zernike decomposition for the simulations. Bonora *et al.* also presented the performance of a new push-pull membrane mirror, and compared it to the pull only version of the mirror, similar to our 37ch OKO MMDM [119]. They simulated the performance of the mirrors to fit 100 aberrated eyes following the statistics published by Castejon-Mochon [11] and found a residual rms wavefront error $\sigma = 0.3$ μm for the pull only membrane mirror, in good agreement with the results we presented for the 37ch OKO MMDM. The value was taken down to 0.1 μm with the push-pull mirror, emphasising the gain in performance that can be obtained with a higher stroke.

Further mirrors were compared in our research group, using the same method. We report here the latest figure obtained [120] showing the residual wavefront error rms for 5 different mirrors, including a 140 actuator MEMS Boston Micromachines mirror, and a 52 actuator magnetic mirror manufactured by Imagine Eyes. The comparison between the Boston Micromachines mirror (BMC140) and the 37ch OKO, which has

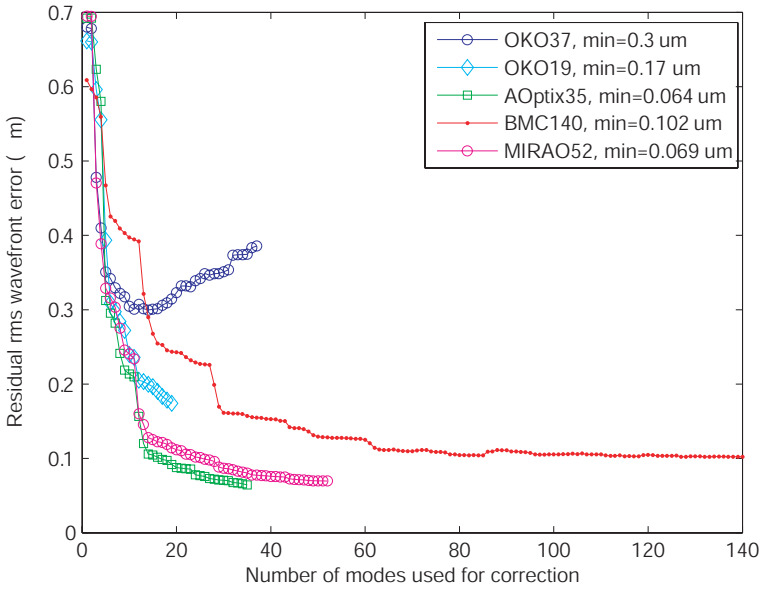

Figure 3.11: Comparison of the residual wavefront error rms after fitting of ocular aberrations with 5 mirrors.

the same stroke, shows the advantage of a larger number of actuators. However, the BMC52 does not provide as good a correction as could have been expected with such a high number of actuators. Only negligible improvement in the fitting error is obtained with more than 100 modes. The mirror has very localized influence functions and a limited stroke; its performance is not as good as that of higher stroke mirrors, such as the Imagine Eyes mirror (MIRAO52) and the AOptix mirror. The two latter show similar results, despite the MIRAO52 having more actuators and a bigger stroke (50 μm). It confirms that a limited number of modes characterises ocular aberrations well, and suggests that pre-corrected ocular wavefronts do not require the full stroke of the MIRAO52. The results can also be explained by the large influence functions of the Imagine Eyes mirror. The stroke and number of actuators are not the only important parameters to be considered; the shape of the influence functions can have great impact on the fitting capabilities of deformable mirrors.

3.4 Discussion

The values of rms fitting error obtained in this study should be considered with caution for several reasons. We will discuss here the possible errors and limitations of the method used to compare the deformable mirrors.

Numerical errors

An effort was made to check the effect of the phase map resolution on the numerical results and the validity of the algorithm approaches. As was mentioned earlier, the phase maps on which was based the numerical analysis were obtained with great resolution to ensure the high precision of the analysis. Some of the phase maps occasionally presented missing pixels inside the pupil; these were removed from the calculations so that they did not affect the fitting error computation. However, the experimental set ups for the three mirrors were such that the phase maps resolution differed from one mirror to the other. In particular, the resolution for the AOptix phase maps was approximately twice (i.e. four times more pixels in 2D) that of the 19 actuator OKO MMDM and of the 37 actuator OKO. All phase maps were binned once such that the numbers of pixels contained in the pupils of the three mirrors were respectively $1.92\,10^5$, $6.12\,10^4$ and $5.23\,10^4$ at the starting point of the simulations. The results given in the previous section, also those published, were derived from these phase maps. For better consistency between the mirrors, further simulations were later performed without binning for the two OKO mirrors, so that the resolution was similar for the three mirrors. Results are shown in Figure 3.12 along with the values previously shown. Although the new residual values for the 19ch OKO mirror are

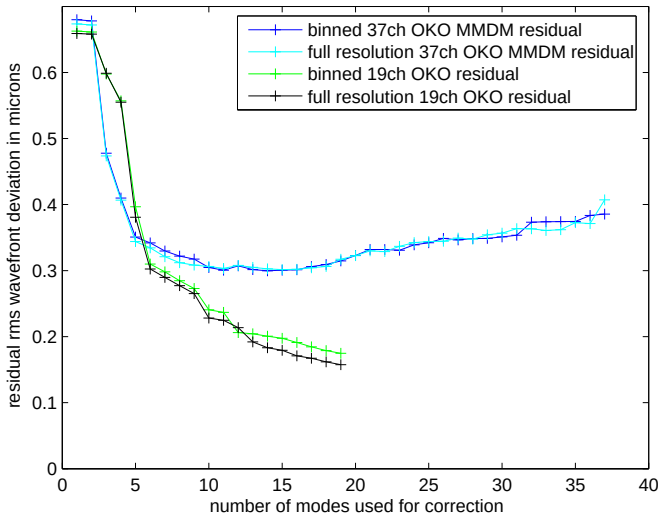

Figure 3.12: Effect of phase maps resolution on the simulations of the OKO mirrors performance.

slightly lower than those presented in the previous section, overall conclusions on the mirrors are not changed: the AOptix mirror still performs better. Calculations

were also performed with binned phase maps of the AOptix bimorph mirror, and the residuals were higher: using all the modes, the rms wavefront error increased from 0.06 μm to 0.1 μm. The change of phase maps resolution seems to have more effect on low residual values, increasing them when the resolution is lowered. It should be remembered that the wavefront error rms values are calculated here point by point, and so a coarser grid is probably more prone to errors. The $2\,10^5$ pixel resolution is about the best that could be used for measurement and calculations time limitations, and is assumed to be sufficient for our simulations.

The phase maps also contained piston terms. It was chosen to remove the piston so that the modes calculated with the SVD did not contain piston. The ocular aberrations to be fitted did not contain piston either, and piston is typically pre-corrected in an AO system. Therefore it appeared more appropriate to remove it completely from the calculations. Preliminary tests showed that the inclusion of the piston in the correction would limit the performance of the mirrors, because it would take up more stroke.

Least-square method limitations

The least-square reconstruction method, which was followed in this study, can present some limitations. We already pointed out the effect some modes can have on the performance, be it piston as described above, or noisy modes degrading the performance of the mirror for certain aberrations (in particular, the high fitting errors values noticed in the generation of particular Zernike polynomials with the 19 actuator OKO mirror). Another major issue arises when saturation of the mirror occurs. Indeed, with an unlimited stroke, the least-square fit gives a solution of the minimisation of the squared phase error, or equivalently the square of the rms (variance of the wavefront error). With a limited range of command, the least-square solution cannot be applied, and the clipped solution may not be the best fit. This last point was further investigated in the particular case of the 37 actuator OKO MMDM which had a serious problem of saturation. The open-loop fitting calculated through Eq. 3.6 was optimised in a closed-loop fashion such that the residual wavefront was fit again on the mirror modes, and further on. Such a correction loop resulted in the residual rms error following an asymptotic curve converging to the minimum value. A number of 20 iterations was evaluated to give a sufficiently good approximation of the final result. The averaged optimised residual wavefront errors rms values are plotted in Figure 3.13. The scale used is the same as the one on the previous graph so that the comparison can be maintained with the other mirrors. The improvement, although

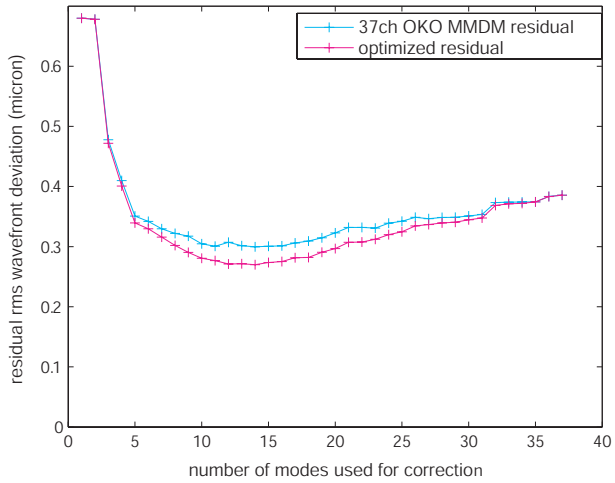

Figure 3.13: Comparison of residual rms obtained with an open-loop correction and a closed-loop correction with the 37 actuator OKO MMDM.

not negligible, does not reach the same level of correction as obtained with the other mirrors. In that particular case of saturation, the question may arise to use a completely different algorithm to find the best fit, such as a direct search method. This different approach was not investigated here.

Model assumptions

The results presented here are of course ideal calculations. The main assumptions are a perfect actuator response (linear for the 19 actuator OKO and the 35 actuator AOptix mirrors, and quadratic for the 37 actuator OKO MMDM) and a linearly additive effect of the actuators influence functions. This linearity is the basis of the algebraic analysis performed. However, as we have seen, the mirror linearity is not always perfect and they can exhibit hysteresis. In a real system, noise and limitations of the wavefront sensor further add complexity to the problem, but the closed-loop reassessment enables to handle them and correct for non-linearities. Therefore, the linearity assumptions can be considered valid here.

The simulations are also dependent on the appropriateness of the model for the aberrations of the eye. We have already mentioned that several wide studies have been completed on ocular aberrations statistics, and they do not point exactly to the same values. In particular, Doble *et al.* [112] pointed out the large differences in magnitude between Thibos population study and another study which had not been published. The real performance of the deformable mirrors can only be verified through

an experimental set up involving human subjects. However, the inter-subject variability is such that an important number of subjects is needed to give statistically significant results.

3.5 Conclusions

We assessed the performance of three commercially available continuous deformable mirrors to correct ocular wavefront aberrations. The simulations pointed to the AOptix bimorph mirror as the best suited for ocular adaptive optics. It demonstrated good ability to generate Zernike polynomials, as well as low wavefront error rms residual when fitting typical ocular wavefronts. The best mean wavefront error rms, over 100 generated ocular wavefronts, was 60 nm, which represents only $\lambda/9$ wavefront error in the visible range. A very good correction, close to diffraction limit, can be expected in a real control adaptive optics system. The study demonstrated the limited performance imposed by the limited stroke of the 37 actuator OKO MMDM, even after static closed-loop optimization of the fitting, and that constrained by the small number of actuators of the 19 actuator OKO mirror. None of the mirrors enabled to achieve diffraction limited correction, and these findings agree with the requirements derived by Doble *et al.*: although the AOptix mirror had a sufficient stroke (5 μm peak-to-valley necessary for the correction of typical 6 mm pupil ocular wavefronts, or 12 μm for 7.5 mm pupil ocular wavefronts), the number of actuators does not reach the 11 actuators across required for the diffraction limited correction of 7.5 mm pupil ocular wavefronts from the same population study [112].

The methodology described provides a valuable analysis of deformable mirrors for vision science adaptive optics. It allows the comparison of mirrors and reveals the appropriate characteristics for particular applications, as the technologies are constantly evolving. The same protocol can be used to evaluate new deformable mirrors, such as our research group did with the Boston Micromachines mirror and the Imagine Eyes mirror. The latter presented the best combination of number of actuators and stroke available, its only disadvantage being the wide influence functions. Such a high stroke mirror would find fully optimised use for highly aberrated ocular wavefronts or simultaneous correction of low- and high-order aberrations.

Chapter 4

Experimental Set Up: AO Vision Simulator

The system used for the project comprised two distinct though connected parts: the adaptive optics system, and the vision simulator. Effort was made to optimise the initial version of the AO system from which the project started, and thoroughly characterise its performance. The visual tests were also carefully implemented, through optical and psychophysical design.

4.1 Adaptive optics correction of ocular aberrations

The adaptive optics system used in this project was initially built by Karen Hampson at Imperial College, London. Most parts of it were left as originally built and the reader can refer to her Thesis [121] and publications [18, 78] for a thorough description of it. We will describe the system briefly before detailing the wavefront sensing and wavefront correction parts, focussing on the further tests and improvements added to the original setup. The performance of the system in terms of ocular aberrations correction will be presented.

4.1.1 Brief description of the system

Figure 4.1 shows the experimental set up used in this project, the adaptive optics part being highlighted. The reader can refer to Karen Hampson's Thesis [121] for further

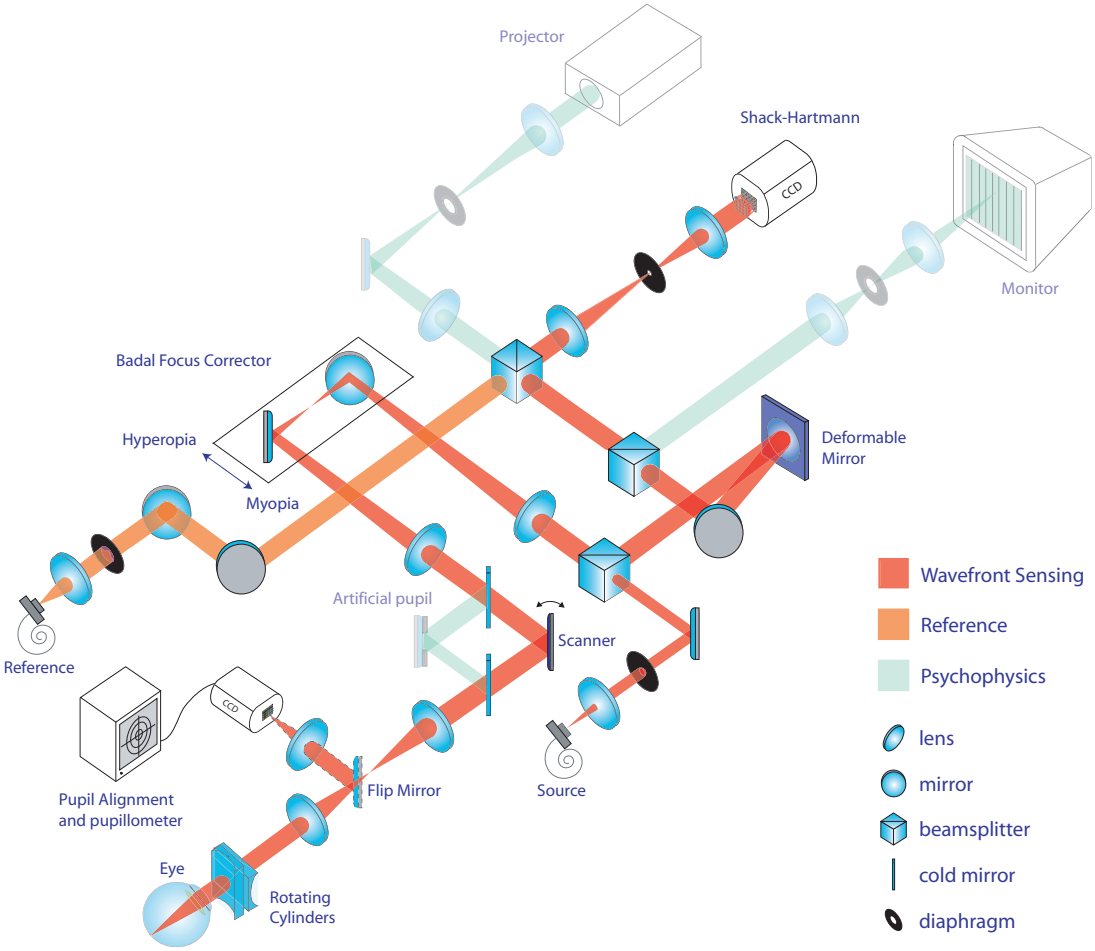

Figure 4.1: AO vision simulator, with highlighted wavefront sensing and correction path.

details about the opto-mechanical components of the system.

The probing illumination is a 825 nm laser diode source. It was chosen in the near-infrared because the human eye is less sensitive and the retinal reflectance is higher in this spectral region [122]. It is also less harmful for the retina, and higher light levels can be used. However, CCD cameras used for the Shack-Hartmann wavefront sensor usually drop in sensitivity in the infrared, and a wavelength of 825 nm was a good compromise. The light enters the eye as a 1 mm diameter collimated beam. It focusses on the retina and is then diffused back to exit the eye through the whole

pupil before being sensed by a Shack-Hartmann sensor. The principles of the Shack-Hartmann sensor have been explained in Section 2.1. The wavefront deformation measured by the Shack-Hartmann is considered to be that created by the second pass through the eye (exit pass) only. As was also discussed, a scanner was implemented in the system to reduce spatial noise on the Shack-Hartmann spots. It was placed in a plane conjugated to the nodal point of the eye in order to descan the beam on the second pass. This element was necessary due to the short exposures (typically 40 to 80 ms) and the source coherence. It was set to scan over half a degree at a frequency of 400 Hz. Analysis of the wavefront sensor precision and accuracy will be given in the next subsection. Infrared (900 nm) diodes were placed facing the eye to provide good illumination for the pupil imaging arm which helped alignment of the pupil. A pupil measurement device was implemented based on the pupil CCD but was not eventually used for the project.

Another source, referred to as the "reference" in the layout, is used to calibrate the Shack-Hartmann: since it does not go through many optics, the collimated beam from this 822 nm source is closer to produce a perfectly plane wavefront on the lenslet array. The spots obtained are then used as reference spots.

Correction of refractive sphero-cylindrical errors is achieved with the Badal optometer and the rotating cylindrical lenses. A thorough description of these elements can be found elsewhere [121, 18]. As this thesis is concerned with higher-order aberrations, effort was put in the pre-correction of low-order aberrations to simulate the correction usually provided by ophthalmic prescriptions. The use and performance of these elements will be detailed later. It can be noted that wavefront sensing light also goes through these elements before reaching the eye, so that the spot formed on the retina is also pre-corrected. This feature improves the quality of the Shack-Hartmann spots which are images of the retinal spot. The higher-order aberrations are corrected with the deformable mirror, placed in a plane conjugated to the pupil of the eye and the Shack-Hartmann lenslet array plane: the aberrations are measured and corrected in conjugated planes.

4.1.2 Accuracy and precision of the wavefront sensor

The wavefront sensor is a key element of the AO system. The aim of the project was not to thoroughly analyse the measurement of ocular wavefront aberrations, but rather to analyse their correction. The closed-loop correction described in Section 4.1.3 does not require wavefront reconstruction; however it is important to know the lim-

itations and errors of the wavefront sensor. These can be translated into accuracy of the initial and residual wavefront errors as given by the sensor. We will therefore detail and discuss in this section the precision and accuracy of the employed Shack-Hartmann sensor.

Centroid measurement error

The sources of errors in the Shack-Hartmann have been detailed in Section 2.1. We can express the centroid measurement noise as

$$\sigma^2_{noise} = \sigma^2_{photon\ noise} + \sigma^2_{readout\ noise} + \sigma^2_{speckle\ noise}. \tag{4.1}$$

The last term represents the noise caused by non-uniformities of irradiance distribution on the CCD. Effort was made to attenuate this noise with the implementation of a scanner in the system, as explained earlier. It is considered negligible and will therefore be left aside. The effect of photon noise and readout noise on the centroid calculations, on the other hand, can be estimated. The variance σ^2 of the centroid under noise is given by

$$\sigma^2_{centroid} = \frac{1}{I_{total}} \sum_{i=1}^{M} r_i^2\, \sigma_i^2 \tag{4.2}$$

with M the number of pixels in the centroiding search block, r_i the i^{th} pixel distance from the estimated centroid, σ_i the standard deviation of the noise and I_{total} the total intensity, in photons, counted in the search block. For photon noise, which relies on Poisson statistics, $\sigma_i^2 = I_i$ with I_i the intensity measured on the i^{th} pixel. For readout noise, σ_i is the value given by the manufacturer in electrons.

The camera was a Retiga EX, which was used with a 8-bit precision yielding a gain of 70 electrons per count (maximum of 18000 electrons). The quantum efficiency was 30% at the wavelength used and the readout noise was 8 electrons. The lenslet array had a focal length of about 8 mm and a pitch of 200 μm. Each lenslet corresponded to 31 pixels in diameter, or about 15 pixels when the image was binned. All measurements given in this Thesis were obtained with binned images, therefore the latter number is of more importance. The spot size, with no ocular aberrations, is limited by the diffraction on the lenslet array, giving a diameter of about 5 pixels. Finally, the positions of the spots were found with a classical centroiding calculation, as derived in Equation 2.2. The algorithm was improved from the original system for better accuracy. It consisted in two steps: a first centroiding calculation over the whole lenslet area (14 pixels-wide square), and a second centroiding over a reduced search block

(10 pixels-wide square) recentered on the first centroid position found.

The numerical calculations of the centroiding noise were performed on Matlab based on the diffraction-limited spot and the parameters given above. Furthermore, the centroid error was experimentally measured with series of 100 recordings of spots obtained with the reference source and later on an artificial eye in place of the human eye. The artificial eye consisted of a lens and a paper placed in its focal plane to mimic the diffusing properties of the retina. The results are given in Table 4.1.2 for two different search block sizes and show good agreement between simulation and experiment. Higher values of noise were measured for the artificial eye as compared to the refer-

Table 4.1: Calculated and measured centroid noise due to photon and readout noise.

Centroid window	14 pixels wide	10 pixels wide
Calculated σ_{noise} (pixels)	$2.5\ 10^{-2}$	$1.9\ 10^{-2}$
Measured σ_{noise} (pixels) with artificial eye	$2.6\ 10^{-2}$	$1.8\ 10^{-2}$
Measured σ_{noise} (pixels) with reference	$1.8\ 10^{-2}$	$1.8\ 10^{-2}$

ence, and this may be explained by the fact that scattering on the paper produced bigger spots on the CCD. The values obtained are in agreement with the study on centroiding error led by Diaz-Santana [123]. He simulated photon and readout noise on the measurement of the centroid of a 6 pixel diameter spot on a 8 e- readout noise camera, and found that at high intensity (peak intensity of the spot higher than 8000 photons), readout noise is negligible as compared to photon noise. In that case centroiding error increases for search blocks smaller than the spot, and is almost constant at higher search block sizes. For lower intensities, readout noise is not negligible and increases with larger search blocks. In that case, the optimum is found for a search block of about the size of the spot. In our case, the light level is such that the readout noise is non-negligible, especially considering the intensity non-uniformities resulting from the diffusing properties of the artificial eye, effect that is enhanced with a human eye. Therefore, it may seem appropriate to reduce the search block. However, reducing it too much may decrease accuracy since the spots obtained from the retina are broadened by the scanner, and a certain dynamic range is required. This issue will be discussed in a paragraph below.

Error propagation and fitting error through wavefront reconstruction

The reconstruction is based on the relation between the measured displacements in the focal plane of the lenslet array and the wavefront first derivatives (see Equation 2.1). In this project, modal reconstruction was obtained with Zernike polyno-

mials. Using Eq. 2.1 and Eq. 1.5, we can write

$$\begin{cases} \sum_{i=0}^{N} a_j \frac{\partial Z_j(x,y)}{\partial x}\Big|_{x=x_i,y=y_i} = \frac{\Delta x_i}{f} \\ \sum_{i=0}^{N} a_j \frac{\partial Z_j(x,y)}{\partial y}\Big|_{x=x_i,y=y_i} = \frac{\Delta y_i}{f} \end{cases} \tag{4.3}$$

with N the chosen number of Zernike polynomials to reconstruct the wavefront over. These relations give a system of N unknown, the Zernike coefficients, and $2 \times M$ known, the x and y displacements measured over the M lenslets. A matrix representation can be used for this problem,

$$\mathbf{s} = \mathbf{D}\mathbf{z} \tag{4.4}$$

where $\mathbf{s}$ is the vector of x and y displacements, $\mathbf{z}$ the vector of Zernike coefficients and $\mathbf{D}$ the matrix formed by the derivatives of the Zernike polynomials and magnification factors. Using Equation 4.1.2, the Zernike coefficients can be obtained with a least-square fit through a singular value decomposition as explained previously. In the remaining of the Thesis, the rms σ of the measured wavefront error was calculated from the Zernike coefficients without tip and tilt which are not considered as relevant aberrations.

The error on the wavefront measurement arises from the propagation of the errors through wavefront reconstruction, and the fitting of the sensor. As was underlined in the description of the Shack-Hartmann, the fitting error is dependent on the number of lenslets, and here on the number of Zernikes reconstructed as well. In our system, the lenslet array pitch was 200 μm. The eye pupil was magnified by a factor of 3 on the sensing part such that the pitch corresponds to 600 μm in the subject's pupil plane. For a given number of lenslets, the higher the order of the Zernike polynomials, the more sensitive they are to noise. Hence the number of Zernike coefficients used for reconstruction should be chosen with respect to the number of lenslets. Figure 4.2 shows the calculated wavefront error rms as a function of the number of Zernike polynomials used in the reconstruction algorithm. The rms wavefront error increases with the number of lenslets, as this number defines the area measured. It can be seen that for each subfigure, the reconstruction changes rapidly from a certain number of modes, because of the noise. Hence these graphs help to determine the maximum order of Zernike polynomial that can be reliably reconstructed for a particular lenslet configuration. The values can be compared to the number of Zernike coefficients commonly accepted for a sufficiently accurate ocular wavefront representation. In the

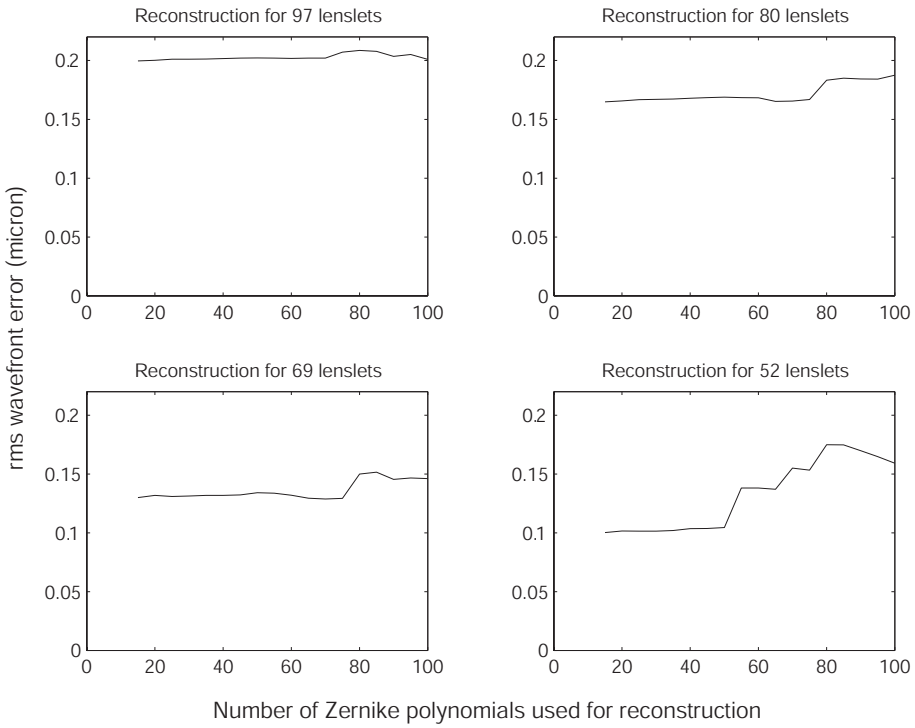

Figure 4.2: Wavefront error rms of reconstructed wavefronts, using different numbers of Zernike modes.

literature, this number usually varies from 20 [15, 9] to 36 [10]. Other authors recently pointed out that in the presence of an irregular tear film, Zernike polynomials up to 9^{th} or 10^{th} order still fail to represent the wavefront observed [20, 21]. A zonal-based method to reconstruct the wavefront from the Shack-Hartmann data, or an interferometric wavefront sensor, might then be preferable. These requirements apply only for very irregular wavefronts (i.e., tear film break, highly aberrated cornea) and did not apply for our project. A number of 36 Zernike polynomials was used in the project for the results presented, where the lenslet configuration was 80. For simplicity, we will neglect the fitting error introduced by a reconstruction with this number of modes.

The overall error on the measurement of the wavefront reduces to the propagation of the centroid error. Assuming equal and uncorrelated noise on each lenslet, it can be proven that the variance of the reconstruction error ϵ^2 is [124]

$$\epsilon^2 = \sigma^2_{centroid} \mathrm{tr}[(\mathbf{D}^t\mathbf{D})^{-1}]. \tag{4.5}$$

The centroid measurement errors given above led to reconstruction errors of about $2\,10^{-3}$ μm. In the case of the human eye, however, the noise may be larger due to the

irradiance distribution non-uniformities over the pupil.

Calibration and linearity

Having discussed centroid measurement errors and wavefront reconstruction limitations, it is important to point out that the wavefront reconstruction is based on geometrical relations (Eq. 4.3), and that it may be good to validate them, after having removed any possible error in the algorithm. In particular, the distance of the lenslet array in front of the camera could not be set exactly to its focal length. Additionally, the measurement dynamic range imposed by the size of the lenslets required to be quantified.

Spherical trial lenses were calibrated with the commercial interferometer used in the previous Chapter, and subsequently measured with the Shack-Hartmann wavefront sensor using three different algorithms (see Fig. 4.3). The initial algorithm, us-

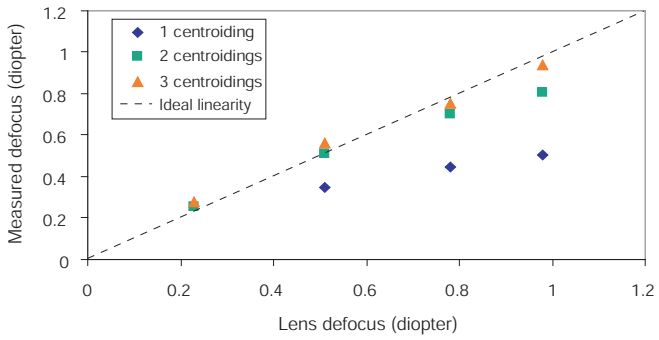

Figure 4.3: Reconstruction of the defocus introduced by a trial lens with different centroiding algorithms.

ing a single centroiding step, exhibits non-linearity due to the limited range given by the lenslet geometry: the centroid measurement becomes inaccurate when the spot reaches the edge of the search block. The 2 or 3 centroiding steps algorithms partially correct for this effect by recentering the search block on the centroid found at the previous step. The wavefront sensing dynamic range required in this project was relatively low, since the interest was focussed on higher-order aberrations. The magnitude of these aberrations for a 6 mm pupil is typically around 0.3 μm wavefront error rms. The algorithm consisting in two centroiding steps therefore appeared suitable and the appropriate scaling factor was implemented in the calculations.

We presented here some experimental results on the error of the measurement and reconstruction of wavefronts as given by the Shack-Hartmann. We wish to highlight again that the purpose of this project was not an accurate measurement of ocular aberrations, but their efficient correction. Reconstruction errors are however important to mention and acknowledge in order to know the accuracy of the initial and corrected wavefronts given, which are in turn used to estimate the correction achieved. These errors could also be used in an optimised control-loop correction.

4.1.3 Wavefront correction with a modal calibration

The initial AO system built by K. Hampson comprised a micromachined membrane deformable mirror from OKO which was changed for a bimorph deformable mirror from AOptix in this project. The AOptix mirror was described and characterized in Chapter 3. This section presents the application of the wavefront correction in the system and the performance of the correction for ocular wavefronts.

Modal calibration

The wavefront correction consists in inverting the matrix **B** relating the mirror commands to the sensor, using a least-square method (Equations 2.3 and 2.5). The matrix **B** is generally obtained through the simple poking of each actuator, the so-called influence functions, and the registration of the correspondent spots displacements produced on the CCD of the Shack-Hartmann sensor. The modes derived by singular value decomposition of this matrix are then used for the wavefront fitting. An alternative matrix was implemented in the algorithm controlling the system. The modes of the mirror, instead of the influence functions, were measured by the Shack-Hartmann. These modes were obtained through interferometric measurement as explained in Section 3.2. They are represented in Figure 4.4. It can be noted that higher order modes get noisier. Using the alternative response matrix of the system **A**, constructed from the response of the Shack-Hartmann to the modes of the mirror, Equations 2.3 and 2.5 can be written as

$$\begin{aligned} \mathbf{s} &= \mathbf{A}\mathbf{m} \\ \mathbf{m} &= \mathbf{M}\mathbf{c} \\ \Rightarrow \mathbf{c} &= \mathbf{M}^{-1*}\mathbf{m} = \mathbf{M}^{-1*}\mathbf{A}^{-1*}\mathbf{s} \end{aligned} \tag{4.6}$$

where $\mathbf{m}$ is the mirror modes vector, $\mathbf{M}$ the matrix relating the modes to the commands applied, and the other variables as defined in Chapter 2. The mirror modes

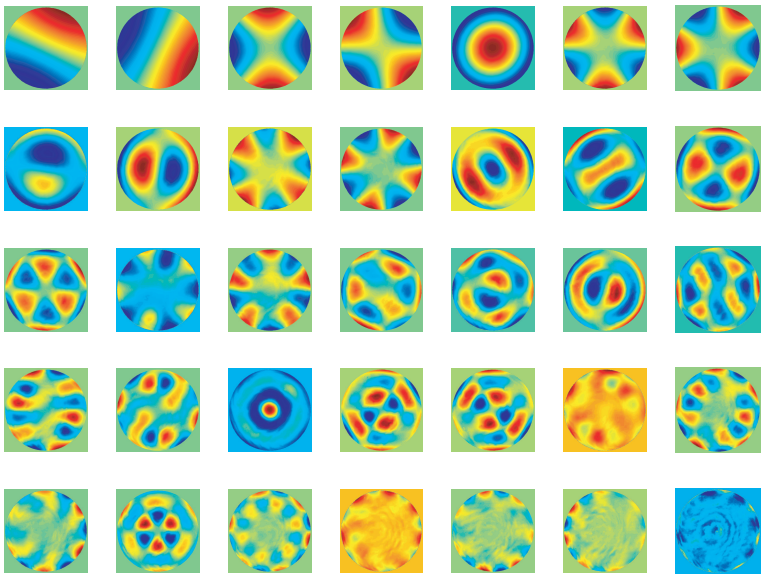

Figure 4.4: Normalised mirror modes obtained through singular value decomposition of the influence function matrix of the mirror.

are theoretically orthogonal by construction. However, the non-linearities in the mirror behaviour alter the modes shape. This is not an issue, since what matters is the conversion from modes to commands and inversely, which has been calculated. The decomposition of the matrix **A** enables one to obtain the modes of the system, which are used for the correction, similarly to the system modes of **B** in the traditional control matrix obtained through zonal calibration.

We already pointed out that the number of modes used for correction impacts the spatial fitting, but also the stability of the correction since higher-order modes are more affected by noise. We compared the two control matrices used, i.e. that obtained from the traditional or zonal calibration and that obtained from the modal calibration, for the correction of a static 0.3 μm defocus aberration term introduced in the system with the Badal optometer over 80 lenslets (6 mm diameter pupil). The two control matrices were used independently, and different numbers of modes were tested. For each configuration (modal/zonal calibration and N modes used in the reconstruction), a total of 100 frames was recorded, and the correction fitting and stability were assessed from the average of the frames after the 10 first ones, i.e. when correction had been reached. Figure 4.5 shows the wavefront error residuals and the command standard deviations averaged over the actuators. The graphs show only a limited range of number of modes since we were interested in changes of stability. Although the mirror comprises 35 actuators, the maximum number of modes was

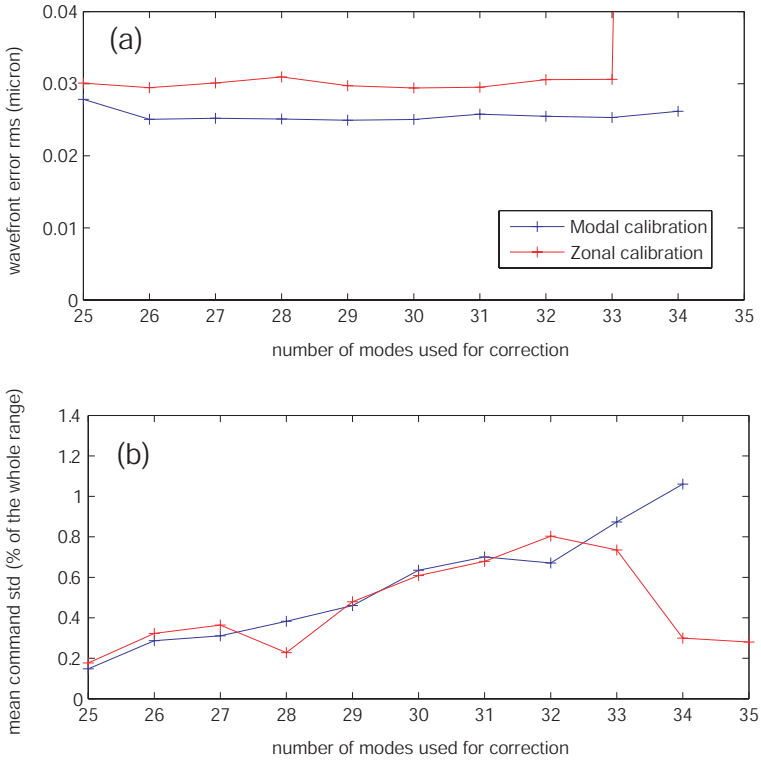

Figure 4.5: Correction of static aberrations with the modal calibration control matrix $\mathbf{A}^{-1*}$ and the zonal calibration control matrix $\mathbf{B}^{-1*}$. (a) Residual wavefront error rms averaged over the run after the 10^{th} frame. Note that the residual after the zonal calibration correction with 34 and 35 modes is out of scale (0.47 μm). (b) Commands standard deviation, in percentage of the whole range, averaged after the 10^{th} frame.

34 for the modal calibration, because as noted earlier, the 35^{th} mode was very noisy, hence excluded from the calculations. It appears from the figures that the correction achieved with modal calibration was slightly better than that obtained with zonal calibration of the system, in terms of wavefront error rms. Since the wavefront to be corrected (aberrations present in the system and additional defocus introduced) did not present significant higher-order aberrations, the wavefront error residual does not vary with the number of modes, except at the highest number of modes 34 and 35 for the reconstruction based on the zonal calibration. At this point, several actuators were clipped, and this saturation severely affected the correction. The clipping also explains why the corresponding commands standard deviations drop down. These standard deviations otherwise increase with the number of modes used for correction, as expected.

The results indicate that the modal calibration enables a slightly better and more stable correction. It should be noted however that the mode dependence on noise is

related to the number of lenslets used, and that the correction fitting error and stability are dependent on the spatial and temporal characteristics of the aberrations to be corrected. Therefore, this study alone does not enable one to generally state the number of modes that should be used for correction of higher-order ocular aberrations.

Closed-loop correction

We present here a temporal analysis of the system which was carried out to investigate the stability and bandwidth of the system. As illustrated by Figure 4.6, a cycle of our AO system starts with the integration of the signals over an exposure time T, typically 60-100 ms for ocular aberrations. Consequently, the frame is read, and the

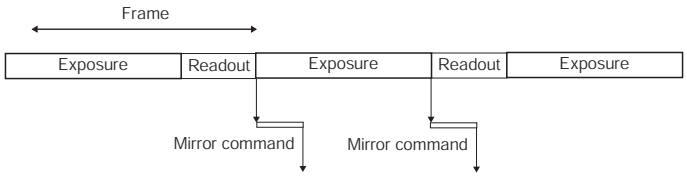

Figure 4.6: Schematic of the processes in the AO closed-loop cycle.

operation takes about τ = 26 ms. A next frame can then be captured, while the matrix calculations are performed - this just takes a few ms - to obtain the new commands which are in turn sent to the mirror - this process takes T_{drive} = 16 ms in our system. The mirror holds the new commands for a cycle which corresponds to $T + \tau$. A general Block-diagram of an AO closed-loop system was given in Figure 2.4. Laplace transforms (see Equation 2.2) were used to model each component.
The wavefront sensor transfer function is an integration over the exposure time, it can be written [60] as

$$G_{WFS} = \frac{1 - e^{-Ts}}{Ts}. \tag{4.7}$$

The readout corresponds to a delay

$$G_{RO} = e^{-\tau s}. \tag{4.8}$$

The control computer follows an iterative, hence discrete behavior. Recalling Equation 2.10 and replacing the control matrix $\mathbf{B}^{-1*}$ by $\mathbf{M}^{-1*}\mathbf{A}^{-1*}$, we can write again the closed-loop integrator relation

$$\mathbf{c}_i = \mathbf{c}_{i-1} + g \times \mathbf{M}^{-1*}\mathbf{A}^{-1*}\mathbf{s}_i. \tag{4.9}$$

The transfer function $G_{CC}(z)$ of this component can be represented as continuous using $z = e^{sT_f}$, with T_f the step time of the control computer (i.e. the inverse of the frame rate); for our system, we have $T_f = T + \tau$. Equation 4.9 can be translated into

$$G_{CC} = \frac{g}{1 - e^{-(T+\tau)\,s}}. \tag{4.10}$$

Finally, the digital-to-analog converter introduces a delay T_{drive} and holds commands for a frame

$$G_{DAC} = e^{-T_{drive}s} \times \frac{1 - e^{-T_f\,s}}{T_f\,s} \tag{4.11}$$

The open-loop, closed-loop and error transfer function are defined as:

$$\begin{aligned} G_{OL} &= G_{WFS} \times G_{WFR} \times G_{CC} \times G_{DAC} \\ G_{CL} &= \tfrac{G_{OL}}{1+G_{OL}} \\ G_{\epsilon} &= \tfrac{1}{1+G_{OL}} \end{aligned} \tag{4.12}$$

It can be noted that the transfer functions that we derived here differ from transfer functions of AO systems found in the literature [89, 60, 86]. In particular, our camera did not enable the readout of the first frame while a second frame was being captured; the process was serial, hence the frame rate was limited by the sum of the two durations. Furthermore, driving the mirror introduced a delay. It may have seemed preferable to trigger the frame exposure on the command of the mirror, but the latency of the camera did not have the required precision.

The stability of the system can be verified with G_{OL}: it is usually ensured by a positive phase margin (the phase angle at the frequency where the gain is 0 dB, shifted by π), and a positive gain margin (the amount below 0 of the magnitude at the frequency where the phase is equal to $-\pi$). Figure 4.7 shows the computed open-loop transfer function for an exposure time of 60 ms, and a gain g varying from 0.4 to 1. Stability is here ensured in all cases: the graph shows a positive phase margin and a positive gain margin for all gains. The closed-loop transfer function gives another indication: the higher the gain, the higher the overshoot as can be seen on Figure 4.8(a). Roddier suggested that the overshoot should not exceed 2.3 dB to maintain stability of the system [60]. The computations indicate that the gain in our system should not be higher than 0.8.

Several criteria can be considered to define the bandwidth of an AO system, the most relevant probably being defined by the error transfer function, since the latter

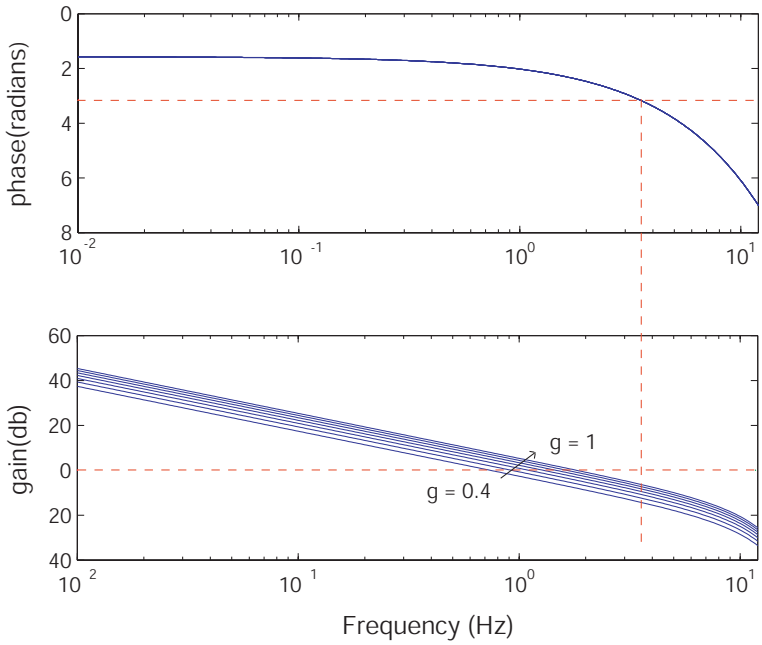

Figure 4.7: Magnitude and phase of the open-loop transfer function obtained for T = 60 ms, τ = 26 ms, T_{drive} = 16 ms, and g = 0.4, 0.5...1.

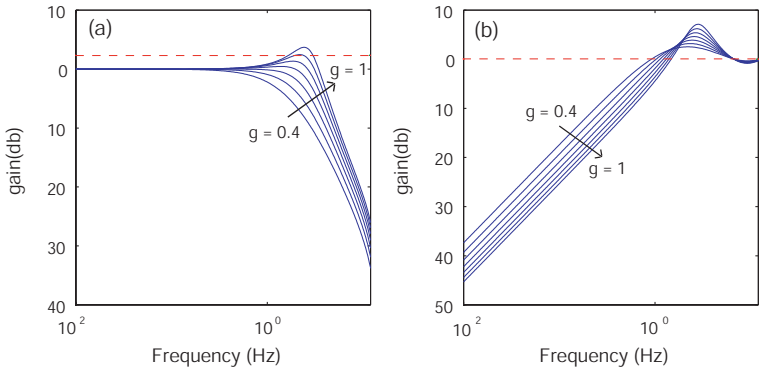

Figure 4.8: (a) Closed-loop and (b) error transfer functions obtained for T = 60 ms, τ = 26 ms, T_{drive} = 16 ms, and g = 0.4, 0.5...1.

relates the residual phase to the aberrated incoming wavefront. The bandwidth is in that case the 0 dB frequency of the magnitude; it is close to 1 Hz for our simulations.

4.1.4 Correction of ocular aberrations

Protocol

The AO system was tested over several human subjects. The wavefront sensing involved the exposure of the retina to near-infrared laser light. Since hazards may potentially result from a direct exposure of the retina to electromagnetic radiations in the UV-IR range, the experiments strictly complied with the maximum permissible exposure values edited by the National Standards Authority of Ireland and the European Union (I.S. EN 60825-1:1994/A2:2001). In our spectral range, the possible damage was thermal. The maximum permissible exposure (MPE) at the cornea for a continuous direct exposure, over a duration from 10 seconds up to 500 minutes, of a collimated beam in the range 700-1050 nm is given by

$$\text{MPE}\,(\text{W}\,\text{m}^{-2}) = 10\,C_4\,C_7 \tag{4.13}$$

where C_4 and C_7 are wavelength dependent factors: $C_4 = 10^{2(\lambda-0.7)}$ with $\lambda = 0.825\,\mu$m and $C_7 = 1$. The value is given for a 7 mm pupil, thus it translates to a maximum power of 684 μW. The laser power at the cornea used in this project was typically 70-100 μW, well below the maximum permissible, and the exposure never exceeded five minutes.

The general procedure for wavefront correction was the following. For each subject, a wax registration of the teething was made and mounted in front of the system for precise positioning and a good stabilization. The pupil area used for measurement and correction of higher-order aberrations was fixed on the camera; the software did not track the head movements. Spherical and cylindrical refractive errors were pre-corrected before AO correction, using the Badal optometer and the cylindrical lenses. When available, the ophthalmic prescription was entered in the program. A finer adjustment was possible through a closed-loop low-order correction similar to that described for the deformable mirror. In that case, the control matrix was obtained with the calibration of the three motors (one for the Badal, and two for the cylindrical lenses) controlling low-order aberrations [121, 18]. The remaining defocus and astigmatism terms after the pre-correction were typically around 0.1 D. Higher-order aberrations were then corrected by the deformable mirror. An illustration of the ocular wavefront at the different stages of correction is given in Figure 4.9.

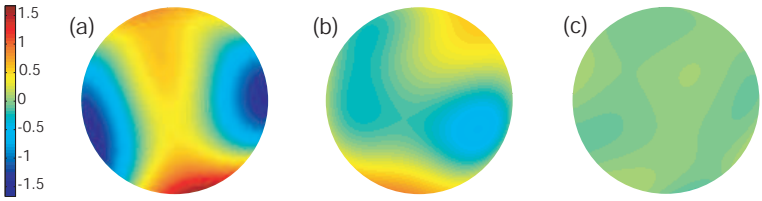

Figure 4.9: Wavefront plots measured over a 5.4 mm diameter pupil: (a) Initial ocular wavefront: wavefront error rms = 0.71 μm, (b) wavefront after sphero-cylindrical correction: rms = 0.32 μm, and (c) wavefront during AO dynamic correction: rms = 0.065 μm. The scale is given in micron.

Adjustment of the correction parameters

When correcting for ocular wavefronts, the number of modes and gain set for the control algorithm had to be adapted for each subject. We give here an example of the effect of these two parameters on the performance of the system. Higher-order ocular aberrations correction runs were performed for one subject; the wavefront error residuals and commands applied were recorded for each run extending over 100 frames. Figure 4.10 shows the performance of the system with modal and zonal calibration,

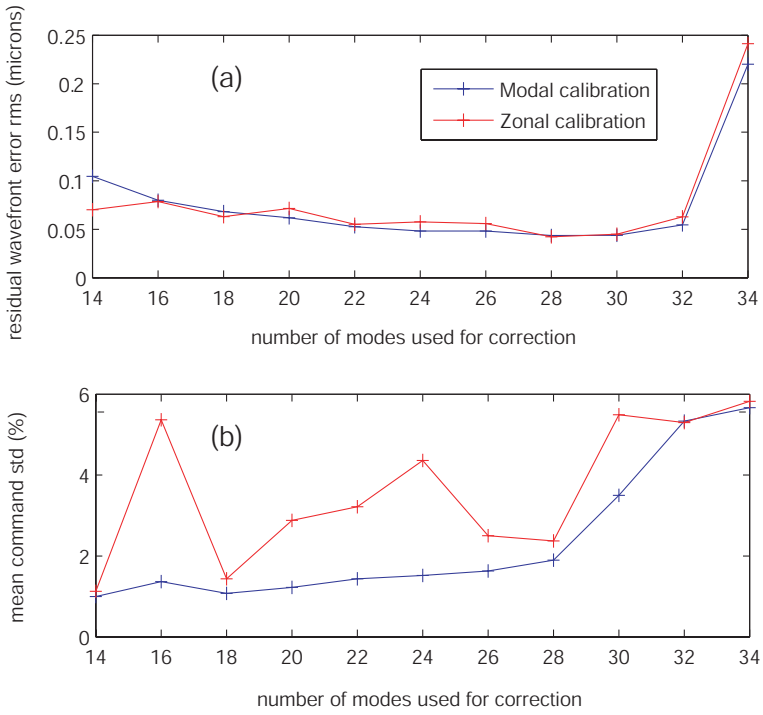

Figure 4.10: Correction of ocular aberrations with the modal calibration control matrix and the zonal calibration control matrix. (a) Residual wavefront error rms, averaged after the 15^{th} frame, (b) average of the commands standard deviation, in percentage of the whole range, after the 15^{th} frame.

with respect to the number of modes used for the correction. The points shown on

the graphs were calculated as the average of two repeated runs of 100 frames for each condition. The two control algorithms give close results, although the modal calibration again seems to yield a slightly better performance, in particular in terms of stability of the system as given by the command variability. As the number of modes used for correction increases, the wavefront error residual is decreased due to higher spatial resolution, until noise propagation in the system suddenly rises, resulting in higher commands variability and degradation of the correction. An optimum number of modes can thus be extracted; it is in the range 26-30 for this subject. The following results presented in this Thesis were obtained with the algorithm using the modal calibration.

A study of the effect of the gain on the correction showed that it mainly affected the time taken by the system to reach the correction level, as can be seen on Figure 4.11. This length of time can be directly related to the closed-loop bandwidth that

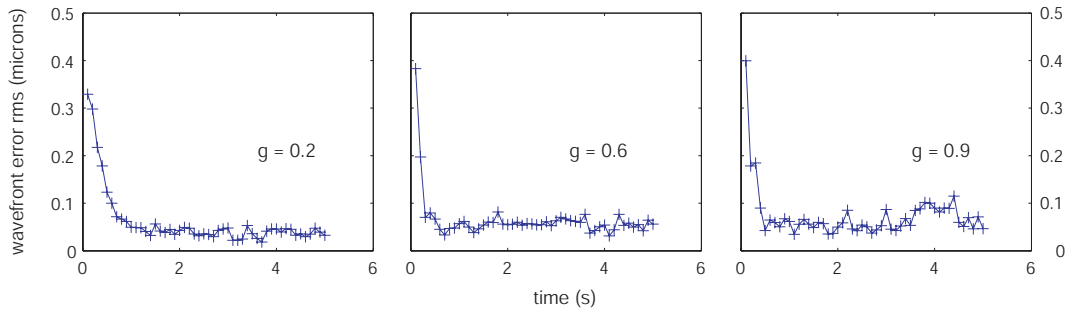

Figure 4.11: Closed-loop correction of ocular aberrations for three different gains used in the correction algorithm.

we defined earlier; it decreases from 1.2 s (0.83 Hz bandwidth) at $g = 0.2$, down to 0.5 s (2 Hz bandwidth) at $g = 0.9$, in good agreement with the numerical analysis performed earlier. Although this is less noticeable, the gain also affected the stability of the system and the wavefront error residual. From the examples shown in Figure 4.11, it can already be noted that the correction is less stable when using a gain of 0.9, than when using a gain of 0.2. For a more thorough analysis, the performance and the stability of the correction as a function of gain were plotted. From Figure 4.12(a), the residual error appears quite constant, although it increases slightly with the gain. The curve 4.12(b), however, clearly confirms the increase of instability of the system with an increased gain. A limiting gain of 0.8, as we calculated it earlier, seems consistent with the graphs.

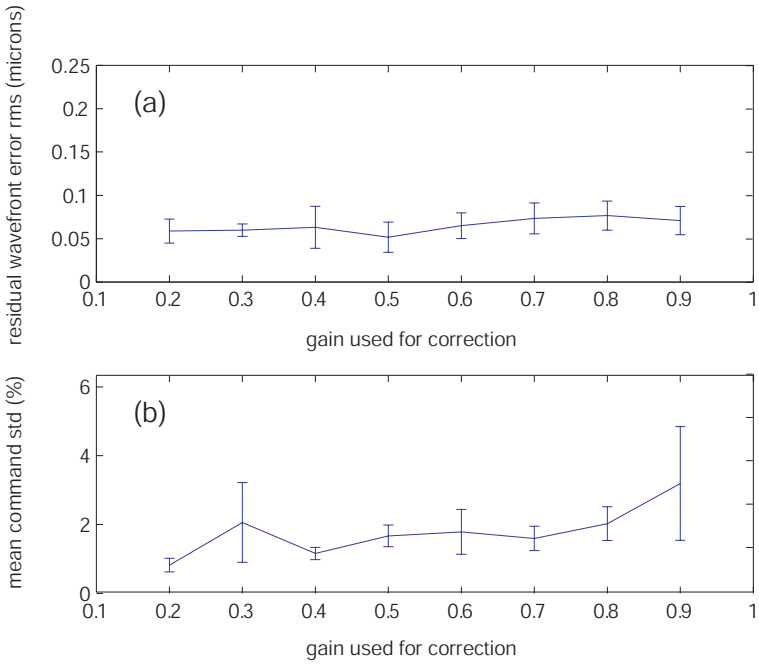

Figure 4.12: Correction of ocular aberrations as a function of the gain in the correction algorithm: (a) residual wavefront error rms, (b) average of the commands standard deviation. The error bars represent standard deviations.

Typical performance

A new adjustment of the correction parameters was required for each subject although the process was not as thorough as detailed above. In general, the gain was set to 0.5 and the number of modes was 27 by default, and roughly optimised for each subject. The correction performance of the system varied significantly from one subject to another. Figure 4.13 shows four examples of correction curves, in terms of wavefront error rms before and during dynamic correction. It can be seen that the residual wavefront error rms was not only dependent on the initial magnitude of aberrations. In general, the residual increased with the initial magnitude, as can be seen on Figures 4.13(a) and 4.13(c). However, factors such as the match between the ocular aberrations and the modes of the mirror, or stability of the subject, also affected the results (see graphs 4.13(b) and 4.13(d)). Note that the high peaks reflect blinks, and should not be taken into account (although the AO correction will be less efficient for a subject who blinks much more than normal). Ocular aberrations dynamics as well as head movements, contribute to the variations in stability of the AO system. Over the duration of this project, the system has been tested on over 15 human subjects; however, different control algorithms, pupil sizes, and dilation drugs (Tropicamide,

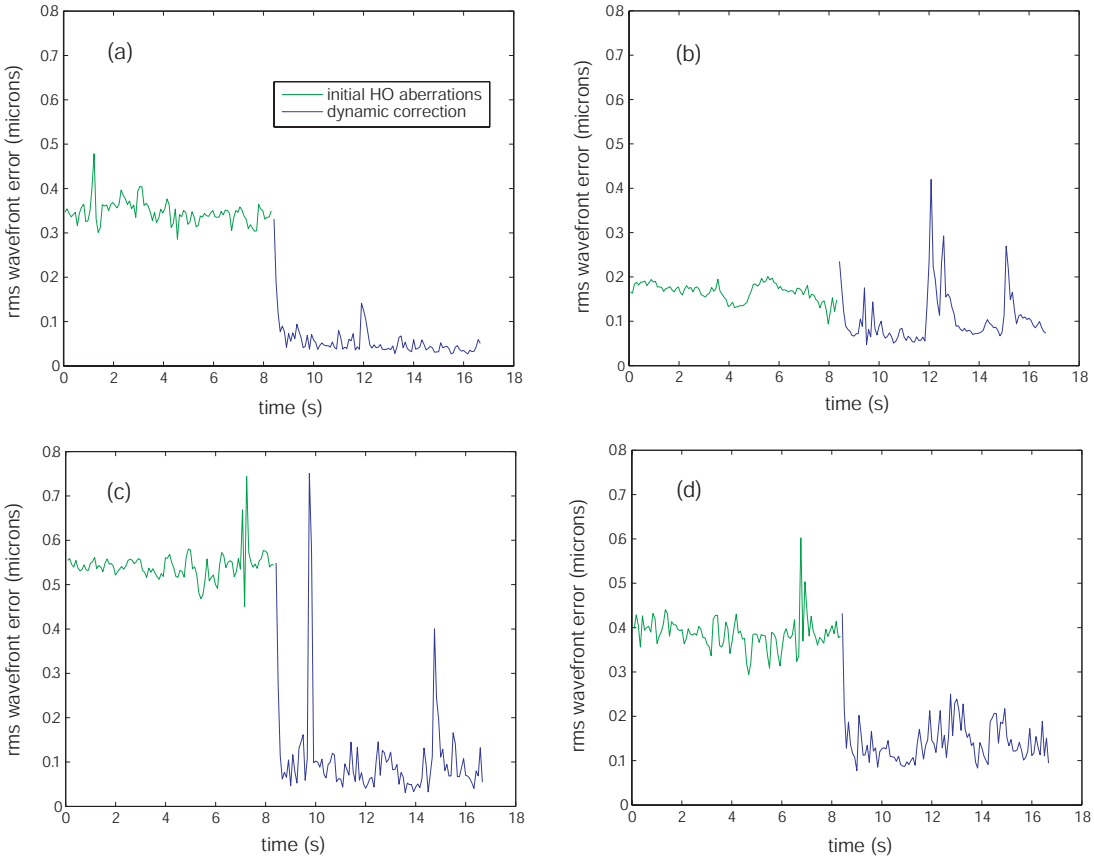

Figure 4.13: Temporal evolution of the wavefront error rms, before and during AO dynamic correction for four subjects. For all subjects, the pupil was dilated with 1% Tropicamide and the measurement and correction pupil was set to 6 mm.

Phenylephrine or none) have been used, making comparison and summary of the performance difficult. In the next chapter, the reader can find the comparison of the AO correction for 7 subjects under the same conditions. In general, the residual wavefront error rms was less than 0.1 μm and this value is comparable to the performance reported by several research groups in the literature [86, 80, 77, 75, 82, 81]. This value is quite close to the simulated residual wavefront error rms reported in Chapter 3: the average residual after the fitting of 100 typical ocular wavefronts by the AOptix mirror was found to be 0.06 μm. However, it should not be forgotten that this value was calculated from interferometric phase maps (2 10^5 pixels). The measurements given by the Shack-Hartmann wavefront sensor - typically with 80 lenslets in this project, have much lower resolution and probably underestimate the error. Furthermore, the error due to the delay between the measurement and the correction adds to the deformable mirror fitting error in the total residual measured by the Shack-Hartmann.

As for the bandwidth, it can be seen from Figure 4.13 that the correction is reached within typically 0.5 s, corresponding to a 2 Hz bandwidth, close to the simulation results.

Finally, the residual closed-loop phase error of correction can be expressed as

$$\sigma^2_{phase} = \sigma^2_{SH} + \sigma^2_{delay} + \sigma^2_{DMfitting} \tag{4.14}$$

where σ^2_{SH} is the Shack-Hartmann error as detailed in the previous section, $\sigma^2_{DMfitting}$ is the fitting error of the deformable mirror and σ^2_{delay} is the error due to the delay between the measurement and the correction. Knowledge of these errors could help optimise the correction algorithm and the resulting performance of the system, as was discussed in Chapter 2. Further investigation however requires better knowledge of the spatial and temporal statistics of the ocular wavefronts. These are likely to be subject-dependent, hence the best strategy would probably be to analyse thoroughly the measured aberrations in open-loop for one particular subject and adapt accordingly the closed-loop correction. Attempts of temporal analysis of the experimental results were made to compare to the theoretical error transfer function, but even the intra-subject variability in the power spectra calculations was quite significant. Two issues in particular should be mentioned: the non-stationarity of the ocular aberrations, as already mentioned, and the movements of the subject's eye with respect to the measurement pupil, which could have altered the measurements of the aberrations dynamics. The performance of the AO system obtained in this thesis was considered sufficient for the planned experiments on vision performance.

4.2 Visual performance measurement

This section describes how visual tests were performed through the system. We will first present the hardware components (displays and optical path), before describing the psychophysical design. Finally, preliminary tests on visual performance with adaptive optics correction of higher-order aberrations will be detailed.

4.2.1 Visible path

The visible path of the system is shown in Figure 4.14. The visual performance tests required the generation of a stimulus with a display, and the imaging of the stimulus though the system, in particular via the deformable mirror. Two different displays

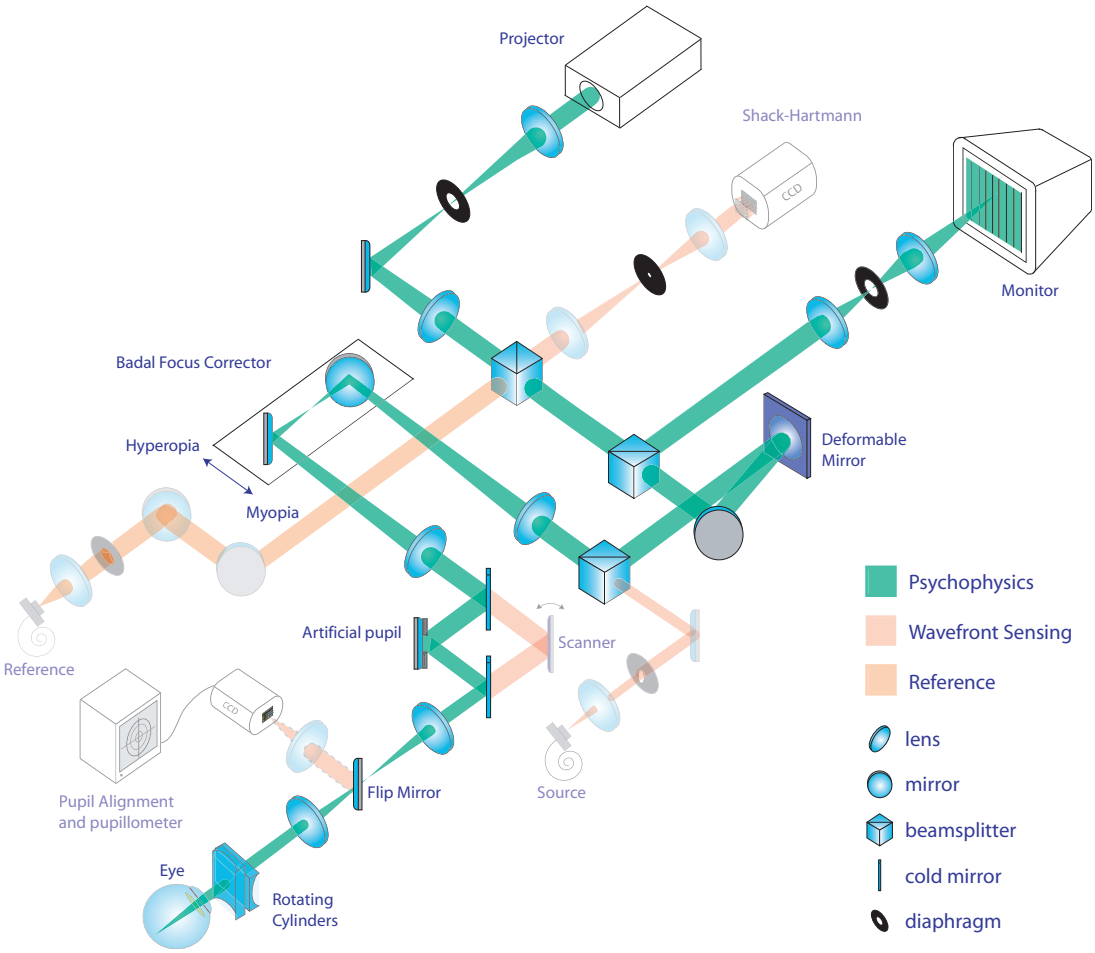

Figure 4.14: AO vision simulator, with the psychophysical path highlighted.

were used alternatively. The initial system comprised a CRT monitor; it was decided to add a digital light-processing (DLP) projector to allow very high stimulus light levels. The visible path consists in the addition of two pairs of lenses before entering the infra-red path described previously. Furthermore, one can notice the two cold mirrors used to bypass the scanner to avoid jitter of the image.

Monitor and projector reimaging through the system

The two displays were implemented in the system with the aim to optimise the balance between sufficient field of view and resolution of the stimulus. To avoid vignetting in the system due to the physical limitations of the optical elements, the field of view was set to about 4.5 degrees by a diaphragm conjugated to the stimulus for

both displays.

The CRT monitor was a 17" Trinitron color display. The two lenses in front of the monitor were adjusted so that, with the total magnification of the system, the height of the screen corresponded to 5 degrees field of view. A pixel of the monitor was imaged on the retina at a size of 0.3'. As an indication, the minimum resolvable grating on the screen had a period of 1.5 mm, corresponding to 32 cycles per degree.

The implementation of the Mitsubishi DLP projector was more problematic because such devices are designed for professional communication use. Hence the characteristics of optics inside the projector could not be obtained; furthermore, the outcoming beam was tilted upward, which added complication. A simple experiment enabled us to determine the exit pupil of the instrument and the field of view subtended by the image. The resulting Lagrange invariant, product of the pupil radius by the field of view in the pupil plane, was much higher than that defined by the deformable mirror and the 5 degrees field of view, preventing proper coupling of the system [125]. Hence the exit pupil had to be greatly magnified in the mirror plane to keep the full image given by the display. Eventually, the two lenses in front of the projector were adjusted so that the height of the display image subtended 4.5 degrees on the retina. A pixel corresponded to 0.34' on the retina.

Non-common path and chromatic errors

One issue in the AO vision simulator is that the wavefront correction was carried out for a beam different from the two beams used for the visual experiments. In particular, the optical paths followed by each beam were not the same - this difference is referred to the non-common path error, and the wavelength was different.

The optical components of the system inevitably introduced wavefront aberrations. These were measured and corrected by the AO system, except for the non-common path errors. The non-common path errors consisted of the two pairs of lenses placed in front of the displays, the two cold mirrors and the mirror bypassing the scanner, which would all introduce aberrations not seen by the wavefront sensor. The relay lenses just before the Shack-Hartmann were not part of the visible paths, but they were part of the reference path, so the aberrations they introduced was not taken into account in the AO correction. The non-common path errors were estimated for an on-axis beam set by an eye pupil size of 6 mm diameter. This was the typical and maximum pupil size used for wavefront correction and visual simulation in the system. Ray tracing calculations yielded f-numbers between $f/15$ for

the two lenses in front of the monitor and $f/30$ for the lenses in front of the projector, hence aberrations were assumed to be negligible for these elements. As for the cold mirrors, the difference between the aberrations introduced by transmission (infra-red path) and those introduced by reflection (visible path) was measured to be about 30 nm wavefront error rms for a 6 mm beam. Finally, the neutral density filters which were used in the study and are described in the next chapter, were characterised; the aberrations they introduced for a 6 mm beam ranged around a few nm, not exceeding 10 nm wavefront error rms.

The source used for wavefront sensing was a 825 nm laser diode, while the psychophysical experiments were carried out in the visible, mainly around 540 nm (green light). Dispersion in the optical components of the eye implies differences of refraction for different wavelength. In particular, the chromatic focus shift is the most significant change in ocular aberrations. It has been analytically derived [126] and experimentally confirmed in the visible [62] and near infrared range [105]. The effect of dispersion on other ocular aberrations, especially higher-order aberrations, is not straightforward and would require better understanding of the ocular optical structures to be described. Marcos et *al.* experimentally measured changes of ocular aberrations, in particular astigmatism and spherical aberrations for two subjects between 450 nm and 650 nm [127]. However, Llorente *et al.* showed that higher-order aberrations measured at 543 nm and 787 nm were equivalent for 36 eyes within the experimental error [62], and Fernández *et al.* obtained similar results while investigating wavelengths from 700 nm to 900 nm with four subjects [105]. For simplicity, we will consider that our measurements at 825 nm provide valid estimates of the higher-order aberrations in green light. This issue could however be further investigated, and we must bear in mind this uncertainty. To account for the chromatic focus shift, the system was carefully calibrated so that a zero defocus term on the Shack-Hartmann for the 825 nm source corresponded to a perfectly collimated stimulus as seen by the subject (the adjustment was performed for an experienced subject after all his aberrations had been corrected).

4.2.2 Psychophysical experiments

Principles of visual psychophysics

Psychophysics is the scientific study of the relation between a stimulus in the physical domain and the correspondent sensation in the psychological domain [128]. Feshner (1860) first developed the theory for the measurement of sensation nowadays used

by all psychophysicists. Central to psychophysics is the concept of sensory threshold, which expresses the fact that mental events have to be stronger than some critical amount in order to be consciously experienced. The concept of differential sensitivity, or relative sensitivity was investigated by Weber (1834) who stated that the change in stimulus intensity that can just be discriminated, $\Delta\phi$, is a constant fraction c of the reference intensity ϕ

$$\Delta\phi = c\,\phi. \tag{4.15}$$

This law provides a useful index of sensory discrimination which can be compared across different conditions and modalities (eg. vision and audition). It is however generally valid for a limited high intensity range only. For visual sensitivity, the eye can be considered as an ideal detector at low luminance level. From known statistics of the quantum characteristics of light, an average absorption of N photons is associated with a standard deviation of $\sqrt{N}$ photons. DeVries and Rose showed that in these conditions the absolute sensitivity threshold is proportional to $\sqrt{N}$ [129, 32]

$$\Delta\phi = k\,\sqrt{\phi} \tag{4.16}$$

with k a constant. The two regimes can be expressed by one single relation

$$\frac{\Delta\phi}{\phi} = c + \frac{k}{\sqrt{\phi}}. \tag{4.17}$$

If $c \ll k/\sqrt{\phi}$, the differential sensitivity follows DeVries-Rose law and if $c \gg k/\sqrt{\phi}$, it follows Weber law. The quantity $\Delta\phi/\phi$ represents the contrast threshold, typically measured in this project for different stimuli. Further laws state that above a critical stimulus area, contrast threshold is proportional to the reciprocal of the area (Ricco's law) and that similarly, above a critical duration, contrast threshold is proportional to the reciprocal of the duration (Bloch's law). These different relations highlight the importance of the stimulus parameters for a consistent measure of relative sensitivity.

A threshold is measured for a certain stimulus based on the performance of the subject for a specific task: to state the presence of the stimulus (detection task), to name or categorise it (recognition task), or to compare it to a reference (discrimination task). As for the way to present stimuli to the subject, three classical methods have been developed: the method of constant stimuli, where a set of pre-determined values expected to be slightly above and below threshold, are presented in random order; the method of limits, where stimulus values are presented in ascending or descending order; and the method of adjustment where the observer adjusts the stimulus value

to the threshold. Because biological reactions to stimuli are variable, the observer response shall be regarded as probalistic and not absolute. Plotting the proportion of success or correctness to a certain task as function of the magnitude of stimulus enables to obtain what is called the psychometric function. The threshold can be set at a chosen success/correctness percentage. The theory of signal detection offers a mean for disentangling the objective (biological) and subjective (such as expectancy or payoff) components of threshold variability.

The measurements carried out in this project were of contrast threshold. Different stimuli were investigated, but the task was systematically a forced-choice discrimination task. The procedure of stimuli presentation was similar for all tests, and is presented below.

The QUEST procedure

Recently, methods have been developed for the stimulus presentation, making use of an estimated psychometric function along with previous responses obtained: they are called adaptive methods. One of them is the QUEST procedure as described by Watson *et al.* [130] and since then widely used. It places each trial at the current most probable Bayesian estimate of threshold, hence providing an efficient, fast and simple test. This method was therefore used for the psychophysical experiments presented in the Thesis.

The procedure relies on three assumptions: the human psychometric function $p_T(x)$, where x is the log intensity and T sets the position of the function, is invariant in form; T is fixed from trial to trial, so all previous trials can be used; the trials are statistically independent. An estimation of the threshold T is used in the calculations, represented as a prior probability density function (pdf) $f_T(T)$. Following n trials, the data obtained consists of a set of n responses r_i at log intensities x_i. This information can be expressed as a likelihood function $f_{D|T}(D|T)$

$$f_{D|T}(D|T) = \prod_{i=1}^{n} p_{r_i|T}(x_i) \tag{4.18}$$

where $p_{r_i|T}(x_i)$ is the probability of response r_i at log intensity x_i, knowing the threshold is T,

$$p_{r_i|T}(x_i) = \begin{cases} p_T(x_i) & \text{if the response is correct} \\ 1 - p_T(x_i) & \text{if the response is wrong.} \end{cases} \tag{4.19}$$

The posterior pdf can be calculated from the likelihood function and the prior pdf of

T

$$f_{T|D}(T|D) = \frac{f_T(T)\, f_{D|T}(D|T)}{f_D(D)} \tag{4.20}$$

where $f_D(D)$ is the prior pdf of the data and is a constant. The next trial is placed at the peak of the posterior pdf, the current most probable estimate of T, and at the end of the run, the final estimate is given by the maximum of the likelihood function. In practice, a QUEST function $Q(T)$ can be derived to express all useful information

$$Q(T) = \ln f_T(T) + \ln f_{D|T}(D|T) \tag{4.21}$$

and the following recursive relations can be written

$$\begin{aligned} Q_0(T) &= \ln f_T(T) \\ Q_n(T) &= Q_{n-1}(T) + \begin{cases} \ln p_T(x_n) & \text{if success} \\ \ln[1 - p_T(x_n)] & \text{if failure.} \end{cases} \end{aligned} \tag{4.22}$$

These relations make the calculations very easy.

The psychophysical tests were implemented with a visual stimulus generator (VSG) from Cambridge Research Ltd. The code was written in Matlab, based on a psychophysics toolbox freely available on internet. The psychometric function used for the QUEST calculations was a Weibull distribution, expressed as

$$p_T(x) = \delta \times \gamma + (1 - \delta) \times (1 - (1 - \gamma) \times \exp(-10^{\beta(x+\epsilon-T)})). \tag{4.23}$$

The parameter δ specifies the upper asymptote $1 - \delta$, acknowledging the fact that even well above threshold, a non intentional mistake can happen, so that the probability of success is never exactly 1; β gives the slope of the function; γ specifies the probability of success at zero intensity, given by pure chance; ϵ is related to the probability at threshold P_T. During the course of this project, two visual performance tasks were used: a two-alternative forced choice (2AFC) task - the subject had to discriminate between two stimulus angles - and a four-alternative forced choice (4AFC) task - the subject had to discriminate between four stimulus angles. Table 4.2 gives the values set for all the parameters for the two tasks and Figure 4.15 shows the computed psychometric functions. The number of trials before termination of the procedure was set following indications found in the literature [131]: 50 for the 2AFC and 30 for the 4AFC. It is reduced for the 4AFC because the probability for a correct response at zero intensity is lower. An illustration of a well converging QUEST run is given by Figure 4.16, which represents an experimental measurement of contrast threshold.

Table 4.2: Weibull function parameters for the 2AFC and 4AFC tasks.

Task	δ	β	γ	P_T	ϵ
2AFC	0.01	3.5	0.5	82%	0.005
4AFC	0.01	3.5	0.25	72%	0.003

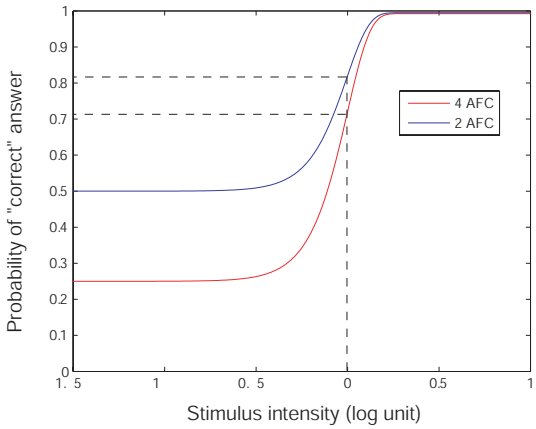

Figure 4.15: Weibull psychometric functions for a 4AFC and a 2AFC discrimination tasks. The threshold is 0 in both cases and the corresponding probability thresholds can be read on the figure (82% for the 2AFC and 72% for the 4AFC).

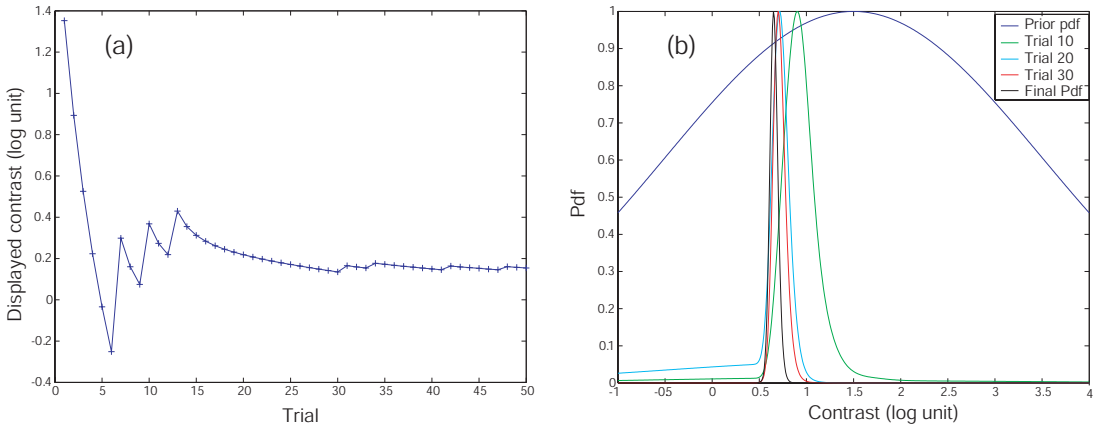

Figure 4.16: QUEST contrast measurement with a 2AFC discrimination task. (a) Sequence of trials through the procedure, set at the current most probable estimate of threshold; (b) Threshold pdf evolution through the procedure.

Figure 4.16(a) shows the trials evolution governed by a decrease of the trial contrast value after a right answer, and an increase after a wrong answer. The displayed contrast oscillates and then converges to a value which is the measured contrast threshold of the subject for that particular task. Figure 4.16(b) shows how the pdf of T, which is originally quite broad and above the true threshold (this was found to be a good

initial point for the procedure), sharpens and converges during the run, reflecting the behaviour of the trial contrast value. In this example, the convergence was reached quite rapidly; however the convergence speed varied from measurement to measurement and subject to subject.

Photometric calibrations

The visual performance measurements were based on intensity contrast measurements, which obviously require rigorous photometric calibration of the system. Both displays were carefully calibrated with a photometer provided by Cambridge Research Ltd. The data were used to construct tables for the gamma correction of the luminance responses of the displays. The VSG allowed a luminance resolution of 14 bits, only possible with analog devices such as the CRT monitor; the resolution of the projector driven by the same VSG was limited to 8 bits. Hence stimuli requiring a high number of luminance levels, such as gratings, were generated on the monitor only.

Most experiments were carried out with spectrally-limited light, defined by the colour channels of the displays. The results given in the Thesis were obtained with "green" light. Figure 4.17 shows the spectra of the two displays. The projector spectrum was measured with a spectrometer, while that of the monitor was given by the manufacturer.

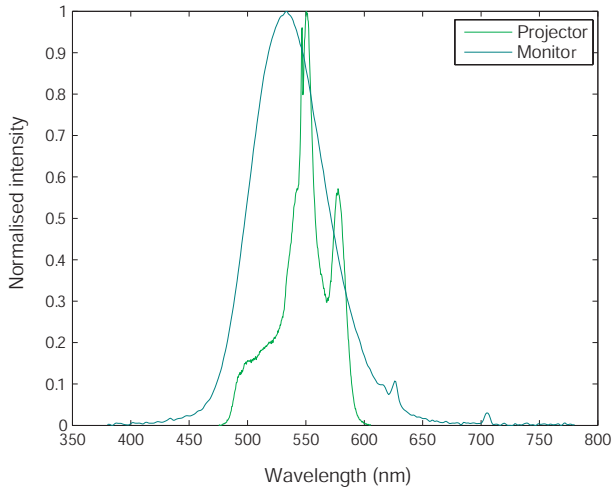

Figure 4.17: Spectra of the two displays used for psychophysical experiments.

Finally, as a large range of light levels were investigated in the experiments led

in this project, accurate measurements of luminance in the ocular pupil plane were required. These were achieved with an illuminance meter from LMT, calibrated to the photopic spectral sensitivity of the eye. The illuminance in the pupil plane E_{pup} is related to the total flux in the pupil F_{pup}

$$E_{pup} = \frac{F_{pup}}{A_{pup}} \tag{4.24}$$

where A_{pup} is the area of the pupil. The luminance L_{pup} can be calculated from the flux

$$L_{pup} = \frac{F_{pup}}{G_{pup}} \tag{4.25}$$

with G_{pup} the geometrical area. The latter can be expressed as $G_{pup} = A_{pup}\pi \sin^2\theta$, with θ the field angle subtended by the image on the retina, as seen from the pupil plane (see Figure 4.18). This yields the relation

$$L_{pup} = \frac{E_{pup}}{\pi \sin^2\theta}. \tag{4.26}$$

Illumination measurements were performed for a known image size, hence a known $\sin\theta$. All the luminance and retinal illuminance values given in this Thesis were derived from the illuminance measurements as just described.

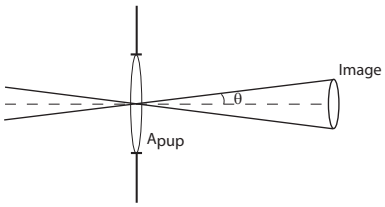

Figure 4.18: Illustration of the geometrical area definition.

4.2.3 First tests of the system

Preliminary experiments with the AO vision simulator were carried out to verify the gain in contrast sensitivity function (CSF) given by the correction of higher-order ocular aberrations. The measurements were done with the CRT monitor and could not be repeated on the DLP projector due to resolution limitations as described earlier.

The contrast sensitivity was measured with horizontal and vertical gratings of different frequencies. These gratings were weighted by a spatial Gaussian envelope, to

form Gabor patches. The spatial luminance distribution $L(x,y)$ of a vertical patch on the retina, proportional to the luminance distribution on the screen, is described as

$$L(x,y) = L_0\,[\,1 + m\,\cos(2\pi f x)\,\exp(-\frac{x^2+y^2}{2\sigma^2})] \tag{4.27}$$

where (x,y) are the coordinates on the retina in degree, L_0 is the mean luminance, f is the frequency in cpd, σ is the standard deviation, chosen to be 0.7 degrees, and m is the contrast. The Gabor patches were furthermore weighted by a temporal envelope of 70 ms standard deviation. A 2AFC discrimination task between horizontal and vertical orientations was set. The QUEST procedure was used to present the stimuli; runs of 50 trials were performed.

The contrast sensitivity was first measured for three subjects, without any AO correction but after ophthalmic correction, in order to test the task and procedure choice. Results are presented in Figure 4.19 and they highlight the inter-subject variability for this task. The characteristic band-pass shape of the contrast sensitivity function

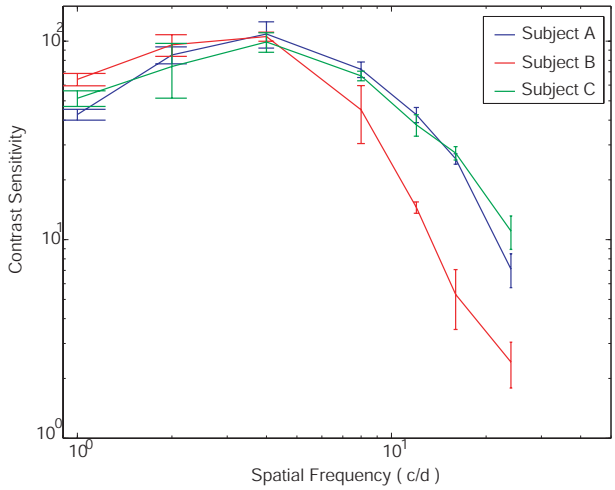

Figure 4.19: Contrast sensitivity obtained for three subjects without AO correction.

is nevertheless well present for the three subjects. The peak appears at about 4 cpd, which is consistent with values given in the literature. We wish to underline that measured contrast thresholds are dependent on the spatio-temporal properties of the stimulus [132]. As a result, there is a wide discrepancy of CSFs in the literature. In particular, the spatial bandwidth of the grating strongly affects visual performance. There has been extensive discussion on the optimised grating window size. Extended grating stimuli with many cycles are well localized in the frequency domain, which facilitates Fourier analysis and comparison to vision models. However, the window

size needs to be inversely scaled with the grating spatial frequency in order to keep a constant number of cycles; this may imply extended fields of view and unpractical experiments at low spatial frequency. Another approach is to aim for a stimulus representing free viewing conditions of real-world images; a number of investigators have argued that a spatial bandwidth of 1 octave (corresponding to a Gaussian function with standard deviation of 0.7 cycle) is an appropriate estimate of the spatial frequency bandwidth of the underlying vision mechanisms [133]. We wanted to have a narrow-band spatial frequency spectrum to help fitting the Fourier analysis of retinal imaging quality and vision system; on the other hand our small field of view did not enable such frequency spectra for gratings of low spatial frequencies. We thus decided to work with fixed-size windows to have sufficient cycles at high spatial frequency.

Complete contrast sensitivity measurements were taken through the system with subject C, with and without correction of higher-order aberrations. The subject's pupil was dilated with Tropicamide 1% fifteen minutes before the start of the measurements. His sphero-cylindrical aberrations (1.9 D of defocus and 0.25 D of astigmatism), as well as the aberrations present in the system, were corrected before the measurements started. The measurements were taken randomly with and without dynamic AO correction, at different spatial frequencies, and repeated to obtain three measurements for each set of conditions (spatial frequency / higher-order aberrations correction). The wavefront sensing light was dimly visible to the subject as a centered 0.5 degrees line superimposed on the grating. This laser was also turned on during measurements without AO correction for similar conditions. Results are shown on Figure 4.20. They show a benefit in contrast sensitivity when higher-order aberrations are corrected, and this benefit increases with spatial frequency, up to 2.2 at 12 cpd. This value is below the AO benefit results obtained by Yoon *et al.*: a benefit of a factor of 3 for a 6 mm pupil [39]. Several hypotheses can be raised. The ocular pupil size for wavefront correction and visual tests was 5.4 mm in our experiment, hence the level of higher-order aberrations was lower. Difficulties in repeating these results with several other subjects also highlighted the sensitivity of the optical alignment, the focus adjustment for the visible light, and the stability of the AO system over long correction runs. The optical alignment, in particular, was an important issue since any displacement of the visible beam from the wavefront sensing pupil would strongly deteriorate the correction. Furthermore, measurements could not be performed at spatial frequencies higher than 12 cpd, where higher AO benefit is expected, because of the relatively low retinal illuminance (25 Td) and the fact that the wavefront sensing light was partially masking the stimulus. Indeed, the contrast sen-

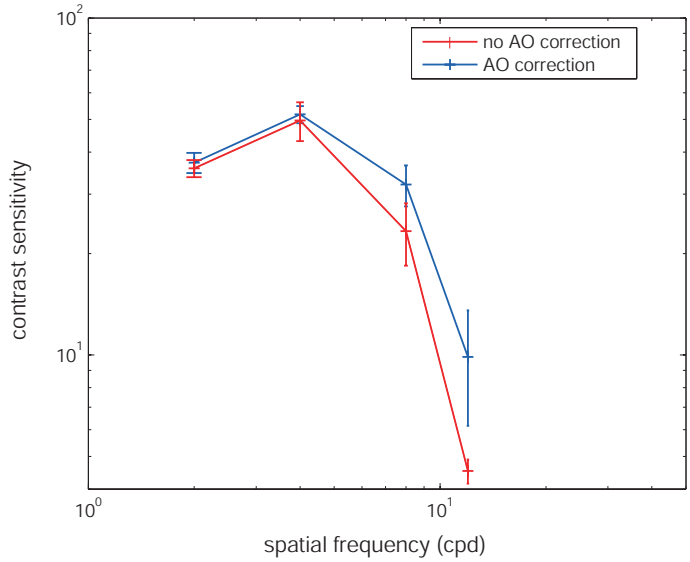

Figure 4.20: Contrast sensitivity measured with and without AO correction of higher-order aberrations for subject C. The error bars represent ± 1 standard deviation.

sitivity values without higher-order correction can be compared to the values in the previous graph, measured outside of the system: they are much lower. The retinal illuminance level is affecting neural contrast sensitivity and may have affected the results. The findings presented here led us to focus our interest on the importance of light level for visual performance, and relate the effects of HO aberrations on visual performance to the changes in neural sensitivity.

The experimental system was described in details with the aim of providing the reader with a full understanding of the different components and resources used. An analysis of the functioning and performance of the adaptive optics system was given, and it was shown that it provides very good dynamic correction of higher-order aberrations, down to 0.05 - 0.1 μm wavefront error rms. The techniques of visual performance tests used in the thesis were detailed and assessed. The first results obtained on the effect of higher-order aberrations on vision were not very conclusive, although they did demonstrate the benefit in contrast sensitivity that can be gained from correction of higher-order aberrations. In the next chapter, a functional visual test is investigated and the effects of HO aberrations on visual performance are measured for such a test, as a function of light level and pupil size.

Chapter 5

Measured Effects of Higher-Order Aberrations on Functional Vision in Different Light Regimes

In everyday life, our eyes deal with an extremely large range of light conditions. Within this range, changes in pupil size, hence in optical quality, occur in parallel with changes in neural sensitivity. Significant visual benefit when correcting higher-order (HO) aberrations has been measured for large pupils in photopic conditions [39]. One should however wonder how the benefit behaves for functional stimuli and natural pupils under normal variations of ambient light. We already pointed out that the contrast sensitivity measured for gratings or Gabor patches gives a limited representation of visual performance. Real-world stimuli are usually more complex: they contain a large spectrum of spatial frequencies. How is our resolution of such objects affected by optical quality in conjunction with neural sensitivity? How do these limitations compare in the different light regimes with natural pupil sizes? It was the aim of

this study to investigate these issues and determine how much normal people would benefit from the correction of their higher-order aberrations in everyday life. In particular, we wanted to focus on the mesopic range where both cones and rods operate. While in the photopic regime, HO aberrations are not expected to affect much vision since pupils remain small, higher complexity arises in the mesopic range with pupil dilation, the reduction of signal to noise ratio, the growth of rods signals and the increase of spatial summation, not to mention chromatic and temporal sensitivity changes [33].

Several series of measurements were carried out on seven young healthy subjects to compare visual performance with and without correction of higher-order aberrations, using the AO vision simulator detailed in the previous chapter. We present here the detailed protocol and the results obtained with some elements of discussion as an attempt to analyse the results.

5.1 Functional visual test

Contrast acuity test

The ability to detect small details at low contrast is functionally of great importance, as shown by Chisholm *et al.* [134]. The contrast acuity visual test used for this study was implemented based on Ref. [134]: it consisted in measuring the contrast threshold needed to discriminate the 3′ gap of a Landolt ring. In Chisholm's study, the average contrast threshold to discriminate this stimulus was 24% in the photopic light regime. The stimulus is shown in Figure 5.1. The size of the gap was chosen such that the

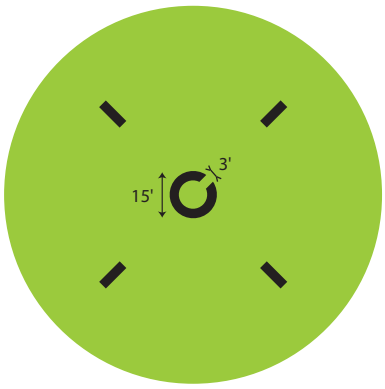

Figure 5.1: Stimulus used for the contrast acuity assessment.

corresponding frequency spectrum is typically within the bandwidth used for functional visual tasks in everyday life. Furthermore, due to its similarity to alphanumeric characters, this stimulus makes an easy target and can provide repeatable contrasts threshold measurements, especially for inexperienced observers. Finally, since only two luminance levels are required for the generation of such a stimulus, both the digital projector and the CRT monitor could be used as displays for the test, allowing a larger range of light levels to be studied.

Two stimulus contrast configurations were used in this study: negative contrast as illustrated by Figure 5.1, where the target is darker than the background (luminance decrements), and positive contrast, where the target is brighter than the background (luminance increments). The contrast in both situations was defined as

$$c = \frac{\Delta L}{L_b} \tag{5.1}$$

where L_b is the background luminance and ΔL is the difference between stimulus luminance and background luminance. This is known as the Weber contrast. For the luminance decrements configuration, contrast ranged from 0 to 100% (assuming negligible external illumination and diffusion of light in the display), while for the luminance increments configuration, the background was set to 10% of the maximum luminance available, enabling a maximum of 900% contrast.

The stimulus was presented with a 100 ms standard deviation Gaussian temporal envelope, and preceded by the short flickering of a dot in the centre of the field. The background field subtended 4.5 degrees of visual angle (note that the field of view in Figure 5.1 is intended only for illustration purposes and has not been drawn to scale) and the guiding diagonal bars were continuously present to help fixation during the visual test. A preliminary experiment was performed with a subject to validate the assumption that the small size of the field of view would not affect the measured contrast acuity thresholds. The experiment was carried out by John Barbur at City University, London, as part of a collaboration for the study presented in this chapter. As can be seen from Figure 5.2, contrast thresholds are approximately independent of the size of the uniform background field. This validated the use of a small field of view for our visual test.

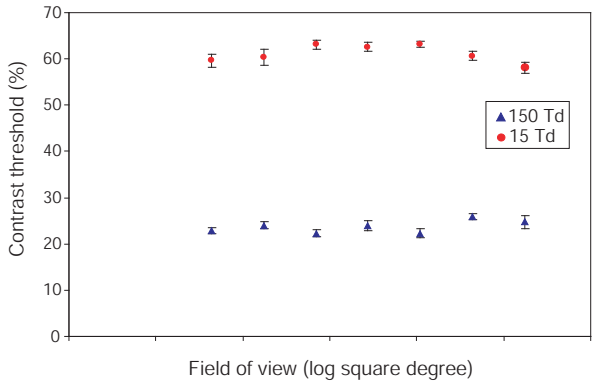

Figure 5.2: Effect of background filed size on contrast threshold, for two retinal illuminance values given in Troland (Td). The error bars represent ± 2 standard deviations.

Light levels

For these experiments, the subject's pupil was artificially dilated to enable the measurement and correction of ocular aberrations over a full 6 mm diameter pupil, while an artificial pupil in the visible path was conjugated to the pupil of the eye (see Figure 4.14) and could be set to limit the effective size of the visible beam entering the eye. This arrangement made it possible to set and calculate accurately the retinal illuminance E_r in Troland,

$$E_r = L \times A_{pupil}, \tag{5.2}$$

where L is the pupil plane luminance (measured in cd m^{-2}) and A_{pupil} is the effective pupil area (in mm^2). Recalling Equation 4.2.2, we can also write

$$E_r = \frac{F}{\pi \sin^2 \theta}. \tag{5.3}$$

Hence the retinal illuminance represents the luminous flux F captured by the eye per unit solid angle of the image on the object (θ is the field angle subtended by the image on the retina). Because it is scaled by the pupil of the eye, it is a measure more appropriate for visual function than luminance.

The Stiles-Crawford effect of the first kind was taken into account in the calculations of the retinal illuminance. As cones are less sensitive to the peripheral rays entering the pupil than the central rays [27], the integration of the luminance over the pupil area was weighted by an efficiency curve to give the effective retinal illuminance

$$E_{r,eff} = \int_0^{2\pi} \int_0^R r \times L \times f(r)\, dr\, d\theta \tag{5.4}$$

with R the radius of the pupil, as set by the artificial pupil. We used a parametric representation of the luminous efficiency, $f(r) = 10^{-0.05r^2}$, derived from values given by Applegate *et al.* [28]. This weighting was not done below 10 Td, since the Stiles-Crawford effect essentially arises when cones function normally. The luminance in the ocular pupil plane required for each retinal illuminance level can be expressed as

$$\begin{cases} L = \frac{E_r}{\pi R^2} & \text{if } E_r \geq 10 \text{ Td} \\ L = \frac{0.05 \ln(10)\, E_r}{\pi(1-\exp(-0.05 \ln 10\, R^2))} & \text{if } E_r < 10 \text{ Td.} \end{cases} \tag{5.5}$$

Neutral density filters were used with the two displays to achieve the appropriate light levels. The projector was used for the highest light levels and the monitor was used for the other light levels, to avoid stacking too many neutral density filters. The set of neutral density filters was calibrated to ensure accurate retinal illuminance values. Measurements were made with an illuminance meter (LMT) calibrated to the photopic spectral sensitivity of the eye. Table 5.1 gives the manufacturer and measured values of optical density of the filters. The standard deviations given are estimated from the variability in the measurements. The transmittance T of each filter is expressed as

$$T = 10^{-OD} \tag{5.6}$$

where OD is the optical density.

Table 5.1: Calibration of neutral density filters

Manufacturer optical density	0.1	0.2	0.3	0.5	0.6	1	3	4
Measured optical density	0.14	0.24	0.33	0.51	0.69	1.1	3.22	4.2
Standard deviation	0.02	0.02	0.02	0.02	0.03	0.03	0.03	0.03

Experimental procedure

Seven subjects participated in the experiment, aged from 19 to 27 years old (22 ± 3). They had no more than 1 D refractive prescription, and no history of ocular disease. They provided informed consent after the protocol and possible consequences had been explained to them. The research was approved by the National University of Ireland, Galway, Ethics Committee and followed the tenets of the Declaration of Helsinki. All the information was coded and strictly confidential. Measurements were performed on the right eye, after a pupil dilation with a drop of 1% Tropicamide.

Before starting the measurements, the sphero-cylindrical errors were corrected in

the system using the features described in the previous chapter. Astigmatism was corrected within 0.1 D, as measured by the Shack-Hartmann, while defocus was adjusted by the subject for best stimulus contrast, with the same precision. In the presence of other aberrations, non-zero defocus can often provide improved image quality [39]; in particular, it can help to compensate for spherical aberration [10]. Wavefront aberrations in the infrared path were also corrected, such that the wavefront aberrations seen by the subject initially comprised only their own higher-order aberrations and the non-common path errors.

Two different experimental procedures were used in this study. The first series of experiments were performed using pseudo-dynamic correction. The near infrared wavefront sensing light was visible to the subject and this ruled out the use of the AO system simultaneously with the visual test. The wavefront aberration correction was therefore only applied in between each trial within a contrast acuity measurement run: the laser was turned on and the mirror dynamically readjusted for 1.5 s to correct for aberrations, the laser was then turned off and the mirror remained frozen for the stimulus to appear. Constant monitoring of the AO correction was maintained to ensure that stability of the correction was reached following each refresh. When no correction was applied, except that of the aberrations of the system, the laser was still turned on and off to simulate the same conditions. Contrast thresholds measurements using decrements in luminance were performed on four subjects with this pseudo-dynamic correction and this set of conditions employed will be described in this paper as procedure A. The procedure was later modified, and a static correction was applied instead. This made it possible to investigate lower light levels without intermittently exposing the retina to the infrared light of the AO laser diode beam. The static correction was considered to be acceptable in our experiments, although Figure 5.3 shows that it was not as good as the dynamic correction. The figure gives the AO dynamic corrections achieved for the seven subjects, over a 6 mm pupil, and the dynamic corrections can be compared to the average static corrections for the three subjects who participated in the second series of experiments. The wavefront aberrations were measured after each test was completed to ensure that the subject had not moved significantly. When the wavefront error rms measured at the end of the run was higher than 0.2 μm, the measurement was deleted. The second series of measurements was furthermore performed with a modified stimulus, which involved increments of luminance, instead of decrements, to allow for high contrast levels. This second set of conditions will be described in the following sections as procedure B.

Contrast threshold measurements were repeated five times for each set of para-

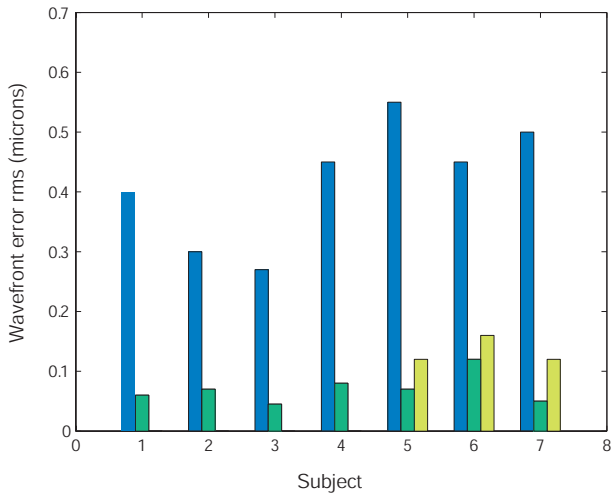

Figure 5.3: Wavefront error rms measured before AO correction, during dynamic correction and after correction (static correction).

meters (light level, pupil size, correction/no correction of higher-order aberrations). The full set of measurements for one particular pupil diameter was split over several sessions to avoid fatigue effects. Each session lasted for just over one hour, and this included the time for alignment, refractive pre-correction, testing of the AO system and breaks in between each measurement. Three or four sessions were needed to complete the measurements. The conditions were randomised whenever possible and the measurements with and without AO correction were carried out in pairs so as to keep the ratio of the two as a repeated measure.

5.2 Results

5.2.1 Effects of light level on functional AO benefit for a large pupil

Contrast acuity measurements were first carried out for a 6 mm pupil, over a range of retinal illuminance values from 1150 Td to 10 Td using procedure A. Four subjects were tested with this procedure. Each subject's performance was measured with pseudo-dynamic AO correction and without correction (except that of sphero-cylindrical aberrations and static aberrations of the system). The contrast sensitivity was calculated as the inverse of the contrast threshold.

Figure 5.4 shows the contrast sensitivity values obtained for one subject, averaged

over the five measurements for each set of conditions. The fluctuations of the measurements are given by the error bars which represent the standard deviations. In

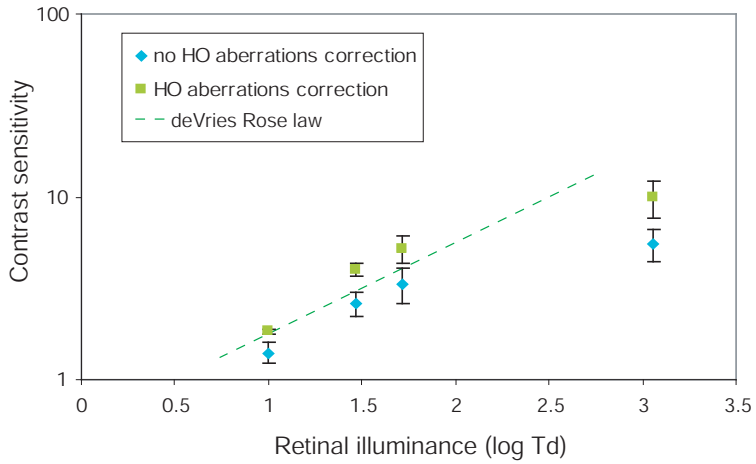

Figure 5.4: Contrast sensitivity measured with luminance decrements for the discrimination of the 3′ gap at different light levels, with and without correction of HO aberrations. The error bars represent ± 1 standard deviation.

all this Thesis, the standard deviations s reported are the unbiased estimations of the population standard deviations, calculated as

$$s = \sqrt{\frac{1}{N-1}\sum_{i=1}^{N}(x_i - \bar{x})^2} \tag{5.7}$$

where N is the size of the sample (five in this case), $x_{i,i=1...N}$ are the measurements and $\bar{x}$ is the mean of the sample. The intra-subject variability in the measurements is quite large, and can be explained by the visual performance variability, the test procedure precision, as well as the AO correction variability. The latter probably did not have too much of an effect, since as can be seen on the figure, the variability without correction is of the same magnitude, if not higher, than the variability of the measurements with AO correction. The subject's visual performance variability was noticeable from one session to another. The limited number of measurements did not enable the estimation of statistical values of this session-dependent variability, but difference ratios in contrast sensitivity of up to 1.5 were measured. Finally, the QUEST procedure used, although it had the advantage of allowing fast measurements, did not always provide consistent results. Measurements were taken out and repeated when the sequence of contrast trials, as shown on Figure 4.16 in the last chapter, was not converging.

As expected, the contrast sensitivity drops as the light level is decreased. Recalling Equation 4.16, the DeVries-Rose law predicts a linear relationship between the log of the contrast sensitivity and the log of the intensity or luminance

$$\log\left(\frac{L_b}{\Delta L}\right) = \frac{1}{2}\log L_b + \gamma \tag{5.8}$$

where γ is a constant. It is represented on the graph with an arbitrary vertical offset, as an indication of the expected trend for the data. Many arguments (optical aberrations, scattering, use of a complex stimulus...) could invalidate the exact fit to this particular law. At high light level, the contrast sensitivity for both conditions seems to approach a constant; this is well in agreement with Weber's law (see Equation 4.15). For this subject, the maximum values of contrast sensitivity were 4.5 without AO correction and 9.9 with correction, corresponding to contrast thresholds of 22% and 10% respectively. The former of these values is close to the average measured by Chisholm *et al.* for the same test [134]. Our subject's performance is slightly better, possibly because she is younger than the mean age of the population examined by Chisholm *et al*. The graph also highlights the benefit in visual performance gained by the correction of higher-order aberrations: the contrast sensitivity is better with adaptive optics than without.

We define the AO benefit as the ratio of the two contrast sensitivities. The ratio calculation was done for each pair of measurements (with and without HO aberrations correction), and averaged for each light level. It should be noted than this value may differ from the ratio of the means of contrast sensitivities. The results, obtained for our four subjects, are presented on Figure 5.5. The error bars represent here the unbiased standard errors of the mean (SEM), calculated as

$$\text{SEM} = \frac{s}{\sqrt{N-1}} \tag{5.9}$$

with s the unbiased standard deviation estimated from the five measurements of AO benefit. A number of five measurements was found to be a good compromise to have sufficiently small standard errors while not over-stretching the total experimental procedure. A striking feature on the figure is that regardless of the within- and inter-subject variability, all the subjects show a progressively smaller AO benefit as light level is decreased. A linear regression with the least-square method was performed on the data for each subject. There is no valid argument to assume linear relationship between the AO benefit and the log of the retinal illuminance. In particular, it is expected that the AO benefit does not go below the value of one, and

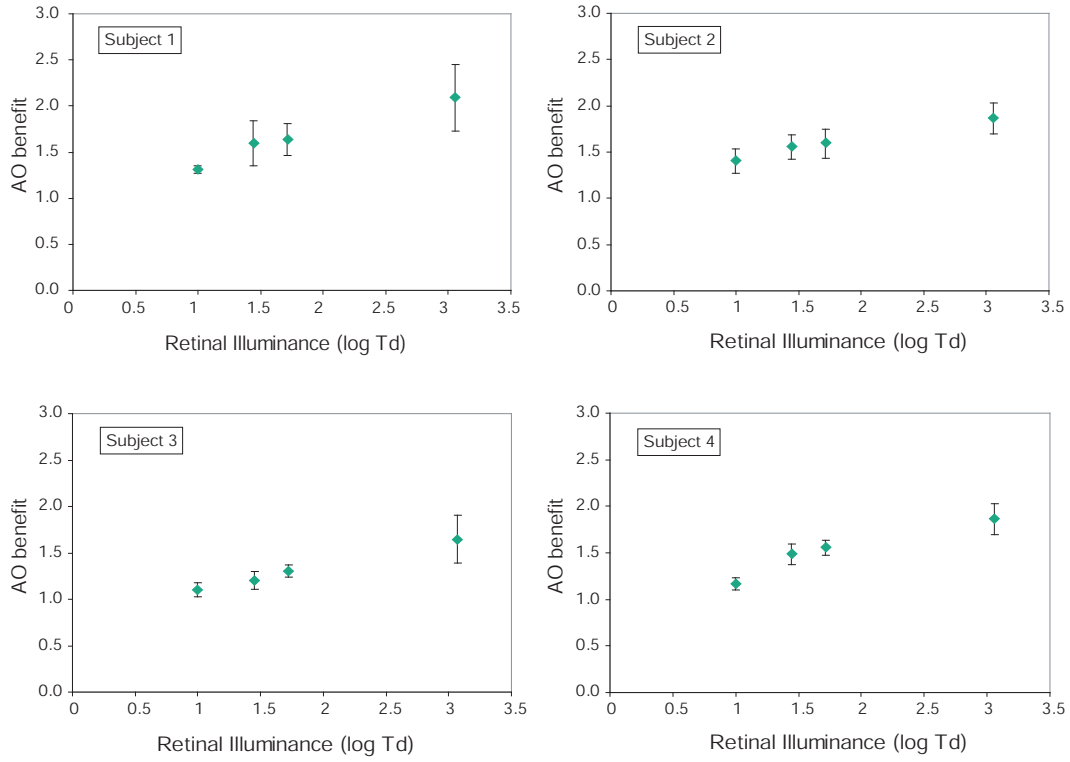

Figure 5.5: Mean AO benefit measured for four subjects over a range of light levels. The error bars represent $\pm$ 1 standard error of the mean.

that at high light levels, when the neural sensitivity is constant, it remains constant too. However, in the range of retinal illuminance levels investigated, the data shows a quite linear trend, and the slope of the best fitted line can give further information on the trend exhibited. The calculated slopes are given in Table 5.2. For each subject, we also report the standard error of the slope, and the 95% one-tail confidence interval for the slope. The confidence interval was calculated with the assumption that the mean slope divided by the standard error of the slope follows a Student's t distribution (the number of degrees of freedom of the distribution is determined by the size of the sample). It lies above zero for two subjects, showing a significantly positive slope. There is almost similar significance for subject 1, but not such significance for subject 2.

Further analysis of the data can be performed with the inter-subject average. The inter-subject mean and standard error of the mean of the AO benefit are given in Table 5.3 for each light level investigated. Consecutive paired Student's t-tests showed significant increase for each higher light level (p-values of 0.014, 0.011 and 0.002).

Table 5.2: Linear regression analysis on the AO benefit data

Subject	Slope	Standard error of the slope	95% confidence interval critical value
1	0.36	0.21	-0.01
2	0.19	0.20	-0.17
3	0.26	0.15	0.00
4	0.30	0.17	0.01

Table 5.3: Inter-subject mean and standard error of the mean of the AO benefit at the different light levels.

Retinal illuminance (Td)	10	30	50	1150
AO benefit	1.25 ± 0.08	1.46 ± 0.10	1.53 ± 0.09	1.87 ± 0.11

The findings from these experiments show that the AO benefit that results from full, 6 mm pupil correction of higher-order aberrations, reduces significantly with decreasing light level, an observation consistent with the expected reduction in the spatial resolving power of the retina. The latter is often attributed to reduced signal to noise ratio in photoreceptors, the intrusion of rod signals and the increased spatial summation. Changes in the processing of the retinal signals at lower light levels cause an overall reduction in neural sensitivity and a decreased spatial bandwidth. The processes involved in discriminating the gap of a Landolt C, for example through frequency channels as vision is often described, have not well been characterised. To the author's knowledge, no model has been derived so far for this particular task. However, several studies on the frequency components of the Landolt C used in such a task suggest that subjects are more sensitive to different components of the letter spectrum depending on the size of the C [135, 136]. One could infer that the visual processes involved will also vary with ambient light. This tentative hypothesis was investigated, and some simulation results are given in the next chapter. Finally, the inter-subject mean of the AO benefit at the highest light level is close to 2. This value remains below the ratios reported by Yoon *et al.* [39]. One can argue that the spatial frequencies investigated in this project are not very high: the 3′ gap extends over three times the acuity limit given by 20/20 by the optometrist. Again, a visual model is required to fully understand these values.

The experiment was extended for two of the subjects: the AO benefit was measured for a stimulus twice as big, the gap of the Landolt ring subtending 6′. Results are given in Figure 5.6. Interestingly, the AO benefit at the highest light level is lower than that at at the next lower light level. The significance of this observation was con-

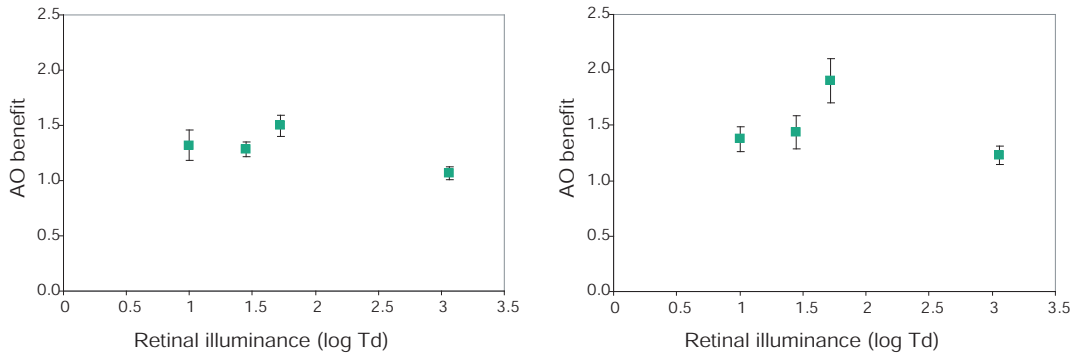

Figure 5.6: Mean AO benefit measured for two subjects for the discrimination of the orientation of a 6′ gap in a ring.

firmed by a t-test for each subject (p = 0.001 and p = 0.011). According to Weber's law, neural sensitivity is constant at high light levels; however some authors have reported a decrease of visual performance with luminance at very high light levels, especially at low spatial frequencies [137, 4]. At lower light levels, the AO benefit for this stimulus shows again a decreasing trend as the retinal illuminance is decreased.

5.2.2 AO benefit for a range of pupil sizes and light levels

As was mentioned earlier, the procedure A used for the previous measurements had several disadvantages. The pseudo-dynamic correction implied repeated exposures of the subject to the infra-red wavefront sensing light. This light, although dimly visible, affected visual performance, and could have affected the AO visual benefit measured. It also reduced the light range where visual performance could be measured. The procedure B was implemented to solve these issues: the AO correction was frozen for the whole duration of the visual test, and the stimulus was generated with luminance increments to enable very high contrast. Preliminary tests were performed with one subject to compare contrast sensitivity with static correction and with pseudo-dynamic correction. Table 5.4 gives the contrast sensitivity means and standard errors of the mean (SEM) at 1000 Td in both conditions, for two different sessions with three and six pairs of measurements respectively. The results show no statistical significant difference between the two protocols.

The contrast acuity tests with and without AO correction were performed for three subjects with procedure B for several pupil sizes, ranging from 3 mm diameter to 6 mm diameter. The neutral density filters were adjusted to set the retinal illuminance

Table 5.4: Comparison of contrast sensitivity measured with two AO correction procedures at 1000 Td, with a 6 mm pupil diameter.

	Session 1		Session 2	
AO correction	Mean	SEM	Mean	SEM
static	10.6	1.7	10.0	1.1
pseudo-dynamic	12.0	1.6	9.9	1.0

at 1000 Td, 100 Td, 10 Td, 1 Td and 0.3 Td. Due to the limited range of filters available, the exact retinal illuminance values differed slightly from one pupil size to the other. In two cases, the background luminance of the display was modified to correct for the difference, and the contrast calculations adjusted accordingly. Table 5.5 gives the relative difference of the set retinal illuminance values with respect to the mean across pupils for each light level.

Table 5.5: Relative difference to the mean of the retinal illuminance values set at each pupil size.

	1000 Td	100 Td	10 Td	1 Td	0.3 Td
6 mm pupil	-0.5%	-1.3%	0.5%	-10%	-8%
5 mm pupil	-0.6%	-1.4%	-7%	8.1%	-1.1%
4 mm pupil	0.1%	-0.7%	5.5%	8.9%	-10.6%
3 mm pupil	1.1%	3.3%	1.0%	-7%	-1.5%

For each condition (pupil size / light level), the AO benefit was calculated from a set of five pairs of contrast sensitivities, similarly to the measurement described with procedure A. The data are reported on Figure 5.7. As expected, the AO benefit increases with pupil size, since the magnitude of HO aberrations increases with pupil size. Furthermore, the curves generally show a similar trend to that observed on the previous results: the AO benefit increases with light level. This effect however becomes less evident at small pupil sizes. The 3 mm curves, in particular, do not exhibit this trend but are rather flat. The AO benefit values below 1 for subjects 5 and 6 may seem to indicate a loss in visual performance after AO correction. One should in fact read these values along with the wide error bars given to appreciate the variability on the measurements. A one-tail t-test (criterion of $p = 0.05$) showed that these values are in fact not significantly below 1. Furthermore, the reader should recall that the AO correction is not diffraction-limited. For a 3 mm pupil, the initial HO aberrations have a very small magnitude, and the AO correction, although it slightly improves the wavefront error rms, introduces residual aberrations unusual to the subject. To

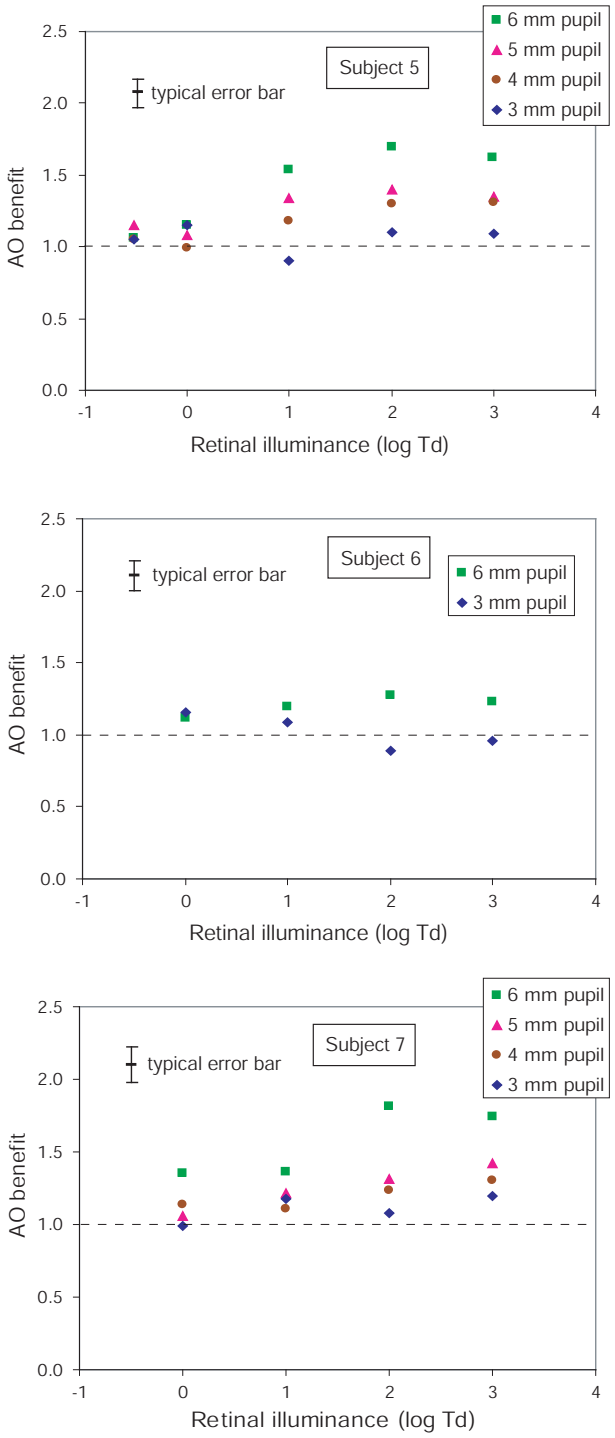

Figure 5.7: AO benefit measured as a function of retinal illuminance and pupil size for three subjects. Error bars represent ± one standard error of the mean.

a larger extent, subject 6 may exhibit this neural compensation of his own HO aberrations, as reported in previous studies [138]: unusual residual aberrations seem to compete with the benefit gained by the increase of the MTF. The resulting AO benefit for a 6 mm pupil, is lower than the benefit for the other subjects in similar conditions. Another subject, who was initially included in the study, showed a decrease in visual performance after AO correction (an AO benefit of 2/3), although the calculated MTF was improved. This subject had a very low amount of initial HO aberrations (less than 0.2 μm), and again, we argue this subject demonstrated neural adaptation to some extent. It would have been of interest to investigate this effect in different conditions (pupil size and light level); unfortunately, such experiments were not possible due to the subject's limited availability. Neural adaptation may be one factor to explain the inter-subject variability shown in Figure 5.7, but other factors, such as differences in frequency-dependent neural sensitivity, scatter and level of HO aberrations correction must be taken into account. Finally, one can also notice on the graphs that the AO benefit at the highest light level (1000 Td), is consistently slightly smaller than that at 100 Td, although the difference was not found to be statistically significative (p = 0.05 t-test). This feature was not observed with procedure A for a 3′ gap. The light levels, in that case, were not exactly identical, and luminance decrements, instead of increments, were used to define the stimulus - resulting in a slightly higher intensity of the stimulus on the retina. This behaviour was also observed for the 6′ gap width procedure A at very high light levels.

5.2.3 Effect of pupil size on functional vision at fixed retinal illuminance

Another way to analyse the data obtained is to compare the contrast sensitivities at different pupil sizes for a given light level. Considering the impact of higher-order aberrations on visual performance, it could be expected that at high light levels and without AO correction, contrast sensitivity should decrease as the pupil size and therefore the HO aberrations magnitude, are increased; with diffraction-limited AO correction on the other hand, contrast sensitivity should increase with pupil size, according to the PSF dependence on the pupil diameter. According to our findings, these trends would become less visible at low light levels. Several factors however made it difficult to perform this analysis on the data. Firstly, the experimental set up was such that it was easy to change light level, but more complicated to change the pupil size, as it required realignment in the system. Therefore, the results pre-

sented were obtained from measurements at a given pupil size with random light level; when this set of measurements was complete, another pupil size was investigated. The subject's performance variability from one session to another made the comparison between pupil diameters difficult and not reliable. Furthermore, the exact light levels, as set with the neutral density filters, slightly differed from one pupil size to another, as shown on Table 5.5.

Another series of contrast acuity measurements were therefore carried out, without AO correction with one of the subjects. The measurements were performed for a 3 mm pupil and a 6 mm pupil, conditions for which the retinal illuminance values are close by less than 5% (except for 0.3 Td). The experiment was carried out over several sessions, with an average of ten measurements for each condition. Because the 3 mm pupil / 6 mm pupil measurements were carried out separately and not as a pair like the AO correction / no AO correction measurements, the mean ratio of contrast sensitivities was in that case calculated as the ratio of the mean contrast sensitivities for the 3 mm pupil / 6 mm pupil. The mean contrast sensitivities and mean ratios are given in Figure 5.8. The relative errors on contrast sensitivities were summed to provide the

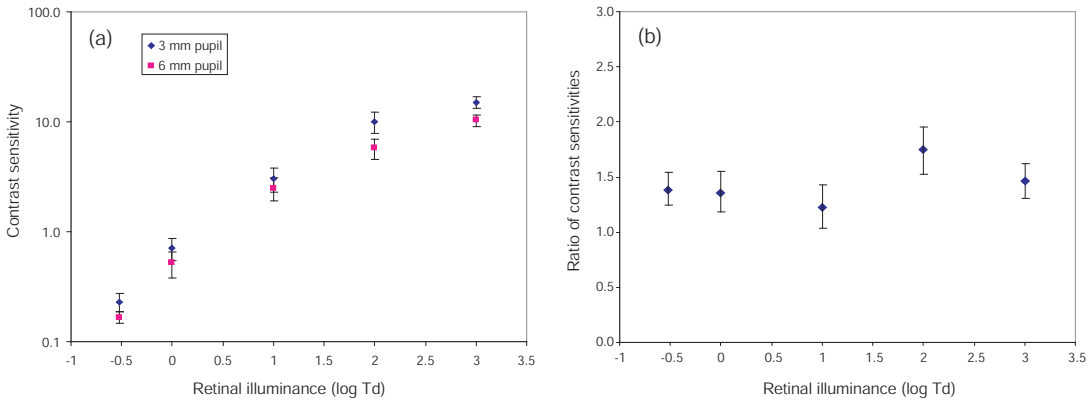

Figure 5.8: (a) Contrast sensitivity measured without AO correction. The error bars represent ± one standard deviation. (b) Mean ratio of the 3 mm contrast sensitivity by the 6 mm contrast sensitivity. The error bars represent ± one standard error of the mean.

relative error of the ratio of contrast sensitivities. As expected, the contrast sensitivity for a 6 mm pupil, uncorrected, is lower than that for a 3 mm, uncorrected, resulting in a ratio above the value of 1. As we discussed above, we would have expected to see this ratio increase with the value of retinal illuminance. The errors are larger than the ones given for the AO benefit, and make it difficult to draw conclusions on the data. The ratio of contrast sensitivities is smaller at low light levels, but the decrease is not

significant. A factor that may affect the data is the amount of scatter, which adds up when the pupil size is increased. This effect would tend to increase the difference between the 3 mm contrast sensitivity and the 6 mm contrast sensitivity (more affected by scattering). It may explain why the measured ratio remains above 1 even at low light levels. One might suggest that scattering has more effect at low light levels than at high light levels, hence dampening the slope of the decrease of our ratio. This issue would require further investigation, in particular on scattering effects.

5.2.4 Expected AO benefit in photopic, mesopic and scotopic regimes

In the aim to quantify the AO benefit that can be gained in normal conditions for everyday vision, the results presented so far must be related to natural pupil size. This study did not involve the use of natural pupils for a number of technical reasons. Firstly, the relatively small size of the field of view used for the psychophysical tests would not have produced steady-state pupil sizes typical of the corresponding ambient light. Furthermore, natural fluctuations in pupil size would have made the AO correction more difficult, as well as the control on retinal illuminance. The use of fixed pupil sizes produced optically were therefore preferred, since this made possible the generation of constant retinal illuminance levels and also facilitated the AO correction. Data on mean pupil size as a function of light level are available from other studies; in particular, de Groot *et al.* [139] compiled several studies and provided a best fit to the whole pupil diameter versus ambient luminance data, represented as

$$\log d = 0.8558 - 0.000401 \times (\log B + 8.1)^3 \tag{5.10}$$

where d is the pupil diameter in millimeters and B is the luminance in millilamberts. B can be related to retinal the illuminance E_r

$$B = \frac{E_r}{2.5\, d^2}. \tag{5.11}$$

Using these two relations, the expected mean pupil size could be calculated for each of the light levels employed in procedure B, after taking into account the Stiles-Crawford effect for the two highest light levels. These calculations are shown in Table 5.6; for clarity we also give the corresponding luminance values and light regimes (the mesopic range extends between 0.034 cd m^{-2} and 3.4 cd m^{-2} [1]). It is important to

[1] These values are given by the Illumination Engineering Society of North America.

Table 5.6: Typical pupil size and luminance at each light level

	Scotopic regime	Mesopic regime		Photopic regime	
Log Retinal illuminance (Td)	-0.5	0	1	2	3
Pupil diameter (mm)	6.1	5.8	5.0	4.0	3.0
Luminance (cd m^{-2})	0.010	0.038	0.51	8.0	140

emphasise that these data reflect only mean pupil diameters and that the effect of light level on pupil size is highly subject-dependant.

Figure 5.9 shows the expected AO benefit under natural viewing conditions as a function of light level, based on the mean natural pupil size at each retinal illuminance. Values for subject 6 are not shown in the figure since insufficient measure-

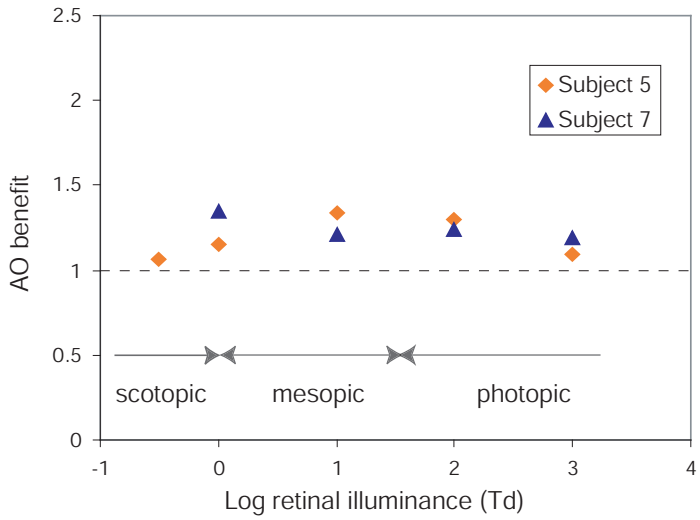

Figure 5.9: Expected AO benefit for two subjects in the photopic, mesopic and scotopic range. The values are taken from Figure 5.7 and fitted to mean natural pupil diameter.

ments were obtained. From Figure 5.7, it can already be seen that the AO benefit for this subject remains limited. Ambient light conditions can be divided in three regimes. In the photopic regime, pupils are small (3-4 mm diameter) and do not introduce large aberrations; no significant improvement in visual performance is therefore expected in this range from AO correction. In the mesopic range, pupils get bigger and exhibit increased wavefront aberrations; however the effect of optical degradation introduced is moderated by the reduction in neural contrast sensitivity. In the scotopic range, the neural sensitivity reduces rapidly and this largely overrides the loss of image quality through increased aberrations. For subjects 5 and 7, the AO benefit does not exceed 1.4 over the whole range of ambient illumination investigated.

5.3 Conclusions

This study reports new results on the effects of higher-order aberrations on visual performance as a function of light level. The study employed measurements of contrast acuity as a function of light level with and without AO correction of higher-order aberrations. The contrast acuity test used was selected to reflect minimal requirements associated with normal occupational visual tasks. The purpose of the study was to predict how the optical image degradation caused by HO aberrations in the optics of the eye affects everyday functional visual performance under normal variation in ambient illumination. In spite of the intra-subject variability, mainly due to their performance variability, and the inter-subject variability, due to differences in HO aberrations, scatter, neural sensitivity, and maybe neural adaptation, we were able to show a significant dependence of the AO benefit on the retinal illuminance. The results suggest that beyond the drop in MTF with increased pupil, other parameters also play an important part in determining the effect of HO aberrations on vision. The true benefit gained by correction of higher-order aberrations depends strongly on the spatial resolving power of the retina which in turn depends on the level of ambient illumination. The typical, overall benefit that can be expected from absent or reduced HO aberrations under normal variations in ambient illumination is therefore limited, either by the reduction of the pupil size at high light level, or the drop of neural sensitivity at low light levels. The data obtained in this study for three young subjects do not exceed 0.15 log unit AO benefit. These findings suggest that, not unexpectedly, the components of the eye are well balanced to optimise vision both at high as well as low light levels. With decreasing illuminance, an increased pupil size allows more light to reach the photoreceptors and this increases the signal-to-noise ratio, while the degraded image quality tends to match the limitations set by the neural mechanisms.

The results reported are of interest in the context of higher-order aberrations for ophthalmic correction, through wavefront guided surgery, intra-ocular lenses or contact lenses. Assuming perfect manufacturing and/or laser ablation, these techniques may not offer as much as might have been expected for everyday functional vision. There are also additional complications. The wavefront correction is very sensitive to alignment. The measurements obtained in this study involved the use of a bite bar to fixate the head of the subjects. As was described earlier, small movements of the subject's head were critical, and so would be any unwanted displacement or tilt of a customized contact lens placed on the cornea. However, the subjects involved in this study were young and their aberrations may not therefore be typical of the larger aberrations expected in older subjects or in unusual patients with much increased

higher-order aberrations, such as patients with keratoconus. The extent to which corrections of larger HO aberrations can improve vision in normal, older subjects, and how increased aberrations may be balanced by the known decrease in pupil size with age remain to be investigated.

The results given in this study were obtained for a specific test. Although they can intuitively be explained by the effect of light level on neural contrast sensitivity, it would be of interest to provide a model simulating these results, model that could be applied to other visual tests. The next chapter gives an attempt of a model of the effects of higher-order aberrations on vision as a function of light level.

Chapter 6

Model of the Observer Visual Performance: Optical and Neural Combined Effects

In the previous chapter, we studied the effect of higher-order (HO) aberrations on functional visual performance as a function of light level. Visual performance was measured as the contrast sensitivity in discriminating the orientation of a 15 minutes of arc Landolt C (the orientation being given by the position of the 3 arc minutes gap), using a four-alternative forced-choice method. We measured the ratio of the contrast sensitivity with adaptive optics (AO) correction of HO aberrations to that without correction of HO aberrations, namely the AO benefit. We showed that the AO benefit for this particular visual task decreases as light level is decreased, for a constant pupil size. This chapter presents a first attempt to derive a model-observer giving plausible explanations for these results.

In the last fifty years, vision models have been developed mainly focussed on grating detection tasks or letter identification. Some of these models include the contrast sensitivity function (CSF); however usually no separation is made between the optical transfer function and the neural transfer function, and the overall CSF used is a generic function representing photopic conditions. The recent advances in

aberrometry have enabled calculations on the impact of HO aberrations on image quality [37], effectively through a simple modulation transfer function (MTF) calculation. Nestares *et al.* performed simulations of Snellen visual acuity with a Bayesian model-observer which included individual data of MTF and neural transfer function (NTF) [140]. The work presented here follows a similar approach, although the visual task is different, and different NTFs representing different light regimes are used. Another particularity is that the model-observer performance is not computed through statistical absolute threshold calculations, but with the use of simple figures of merit. The relative performance in the presence and absence of HO aberrations is compared to the AO benefit that was experimentally measured.

6.1 Derivation of the model-observer performance

We develop a model observer for a classification task, which includes several stages starting with the optical and neural filtering of the image seen by the observer, yielding a data vector. This data vector is in turn used to produce a test statistic based on which the observer makes a decision. The different stages are described, and figures of merit for a binary and multi-class classification tasks are derived in the case of a an ideal observer.

Spatial frequency analysis of visual processes

We have seen in Chapter 1 that the retinal image quality has been described through Fourier analysis since the first half of the 20^{th} century, and that the concept of neural sensitivity appeared shortly after. The visual linear system analysis was further investigated by Campbell and Robson who suggested in 1968 that the visual system contains a group of independent, quasi-linear bandpass filters, more narrowly tuned for spatial frequency than the overall neural sensitivity. These channels can be related to the receptive fields of the ganglion cells. The neural sensitivity is of particular interest for us, since we wish to investigate the changes in visual performance in different light levels, implying different neural sensitivities. We present here an analysis of the visual processes generating a vector of data $\mathbf{s}$ from the input object seen by the subject, based on Fourier analysis.

As we have seen in Chapter 1, in incoherent illumination, an optical system is linear in intensity, and the intensity of the image equals that of the object convolved with the intensity point spread function (PSF). The last statement is valid only for a

stationary (or isoplanatic) system, for which the optical degradation is independent of field angle. In our case, the stimulus subtends 15 arc minutes; this is commonly accepted to be within the eye's isoplanatic patch. Under this assumption, we can use Fourier transforms, and express the retinal image, after filtering of the eye's optics, as

$$\widetilde{I}_{retinal}(u,v) = \widetilde{I}_{obj}(u,v) \times \widetilde{\mathrm{PSF}}(u,v) \tag{6.1}$$

where $\widetilde{I}_{obj}$ and $\widetilde{I}_{retinal}$ are the Fourier transforms of the object and retinal image intensities respectively, and $\widetilde{\mathrm{PSF}}$ is the Fourier transform of the PSF, generally called the optical transfer function or OTF.

Similarly, the neural sensitivity can be modeled as another filter applied to the retinal image. We investigated for this work two approaches: an overall filter applied to the eye, the NTF, or a set of filters representing the channels mentioned above. The use of a set of independent channel signals in detection tasks has been experimentally confirmed [141] and a channelised model-observer has shown good agreement with human-observer performance in many different situations [142]. The channels and overall NTF used in this project will be described in the next section. In the case of the overall NTF, the final image can be expressed in the Fourier domain as

$$\widetilde{I}_{neural}(u,v) = \widetilde{I}_{obj}(u,v) \times \mathrm{OTF}(u,v) \times \mathrm{NTF}(u,v) \tag{6.2}$$

while with a set of N channels, the Fourier transform of the retinal image is integrated over each channel independently to give a set of channel outputs $s_{j,\, j=1\ldots N}$

$$s_j = \int_{u,v} \widetilde{I}_{obj}(u,v) \times \mathrm{OTF}(u,v) \times \mathrm{C}_j(u,v) \tag{6.3}$$

where C_j is the j^{th} channel profile in the Fourier domain.

Two forms of the data are thus derived: the neural image in the frequency domain or the outputs of the channels. Expressing the output data as a real vector, it can be summarised as

$$\mathbf{s} = \begin{cases} \mathbf{H}_{NTF}\, \mathbf{H}_{OTF}\, \tilde{\mathbf{o}} \\ \mathbf{C}^t\, \mathbf{H}_{OTF}\, \tilde{\mathbf{o}} \end{cases} \tag{6.4}$$

where $\tilde{\mathbf{o}}$ is the Fourier transform of the object intensity expressed as a vector, and $\mathbf{H}_{OTF}$ and $\mathbf{H}_{NTF}$ are two diagonal matrices built from the elements of the OTF and the NTF respectively.

Binary decision model

The processes described above are corrupted by noise, which yields us to use the theory of signal detection, as first proposed by Tanner and Swets in 1954. The theory of signal detection was developed based on the concept of noise; it states that the observer makes a decision from the observation of data polluted by noise. Due to the randomness of the input, the process is described statistically.

Let us consider here a classification task, such as that used in our experiments. We will further limit ourselves to the binary problem, i. e. the classification between two classes. The whole process is represented by the flow chart of Figure 6.1. The data

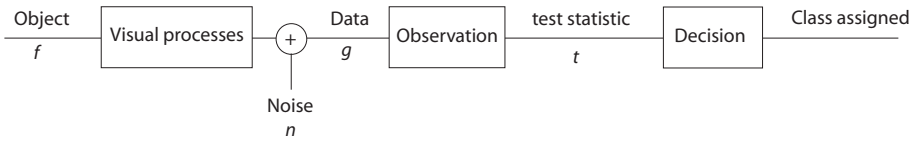

Figure 6.1: Flow chart representing the classification task performed by the observer.

observed is denoted $\mathbf{g}$

$$\begin{aligned} \mathbf{g} &= \Gamma\mathbf{o}_1 + n = \mathbf{s}_1 + \mathbf{n} \quad \text{under hypothesis } H_1 \\ \mathbf{g} &= \Gamma\mathbf{o}_2 + n = \mathbf{s}_2 + \mathbf{n} \quad \text{under hypothesis } H_2 \end{aligned} \tag{6.5}$$

where hypothesis H_1 or H_2 denotes that the object f_1 or f_2 respectively is present at the input, $\mathbf{s}_1$ is a vector resulting from the imaging process and $\mathbf{n}$ is the noise in the process described in the previous paragraph. We will describe here the observation and decision stages. The decision is made with a simple scalar t, which we will refer to as the test statistic. This test statistic is obtained with the discriminant function applied on the data: this is the observation. The observer assigns a given data set to a particular decision class by comparing t to a decision threshold or cutoff t_c. When $t < t_c$, class H_1 is chosen, we denote this decision as D_1; when $t \geq t_c$, class H_2 is chosen, this decision is D_2. Because of the noise, the decisions in the process cannot always be correct. For a two-alternative forced-choice (2AFC) task, four outcomes are possible, as shown on Table 6.1.

Table 6.1: Decision outcomes for a binary classification task.

Outcome	Hypothesis	Decision
True Positive (TP) / Hit	H_2	D_2
False Positive (FP) / False alarm	H_1	D_2
False Negative (FN) / Miss	H_2	D_1
True Negative (TN) / Correct rejection	H_1	D_1

Decision outcome fractions can be defined in terms of probabilities

$$\begin{aligned} \text{TPF} &= Pr(D_2|H_2) \\ \text{FPF} &= Pr(D_2|H_1) \\ \text{FNF} &= Pr(D_1|H_2) = 1 - TPF \\ \text{TNF} &= Pr(D_1|H_1) = 1 - FPF. \end{aligned} \tag{6.6}$$

These fractions can be used to construct the receiver operating characteristic (ROC) curve, which shows the relation between the TPF and the FPF. The ROC curve is very useful because it summarizes the difficulty of the task, the performance of the observer strategy, and the quality of the data. Also useful is the area $\mathcal{A}$ under the ROC curve, namely the AUC defined as

$$\mathcal{A} = \int_0^1 d(\text{FPF})\ \text{TPF(FPF)}. \tag{6.7}$$

The ability of the observer to perform the task is dependent on the object, the visual processes, the noise, the observation and the decision strategy. We will assume that the observation and the decision strategy are independent of the conditions of the experiment (light level / correction of higher-order aberrations), and that the nature of the noise is also a constant, its level being probably dependant on the light level but not on the correction of higher-order aberrations. We wish here to compare contrast sensitivities, therefore to give an estimate of the observer performance. Several figures of merit can be used; we choose to work with the signal-to-noise ratio of the test statistic

$$\text{SNR}_t = \frac{\langle t_1 \rangle - \langle t_2 \rangle}{\sqrt{\frac{1}{2}({\sigma_1}^2 + {\sigma_2}^2)}} \tag{6.8}$$

where the brackets $\langle\rangle$ refer to the statistical mean. We will see later how we can relate SNR_t to the visual performance experimentally measured.

If the test statistic is normally distributed under both hypothesis, the SNR_t can be related to the probability of a correct decision in a two-alternative forced-choice

method P_c. Indeed, it can be shown [142] that P_c corresponds to the definition of $\mathcal{A}$ as defined earlier. Furthermore, in case of normally distributed test statistics, we can write

$$\mathcal{A} = \frac{1}{2} + \frac{1}{2}\,\mathrm{erf}\left(\frac{SNR_t}{2}\right) \tag{6.9}$$

where erf is the error function defined as

$$\mathrm{erf}(z) = \frac{2}{\sqrt{\pi}} \int_0^z dy\, \exp(-y^2). \tag{6.10}$$

Therefore, a known percentage correct for a 2AFC corresponds to a defined SNR_t. In that case, it is of common use to refer to SNR_t as the detectability d'.

Performance of an ideal observer with Gaussian statistics

Different observer strategies are possible to perform a binary classification task. The ideal observer, i.e. an observer that maximizes $\mathcal{A}$, is an observer that performs a likelihood-ratio test properly [142], written in the form

$$\text{Choose } H_2 \text{ if } \Lambda(\mathbf{g}) = \frac{\mathrm{pr}(\mathbf{g} \mid H_2)}{\mathrm{pr}(\mathbf{g} \mid H_1)} > \Lambda_c \tag{6.11}$$

where Λ is the likelihood ratio and Λ_c is the decision threshold. A Bayesian observer or an observer that follows the maximum-likelihood criterion is an ideal observer. The likelihood-ratio test requires to have to the information necessary to formulate $\mathrm{pr}(\mathbf{g} \mid H_j)$.

We will make here an important assumption, which is that the signal $\mathbf{g}$ to classify is nonrandom and corrupted by additive Gaussian noise. This is the so-called SKE/BKE (signal-known-exactly/background-known-exactly) problem. We further assume that the noise $\mathbf{n}$ is zero-mean, independent and identical Gaussian, whether $\mathbf{g}$ represents a vector of the neural image in the spatial domain, in the frequency domain, or a vector of the channels outputs. The noise itself can have several sources (light-dependent noise, neural noise, fluctuations in the decision criterion...). Several studies have shown that human performance is well predicted by an ideal observer in uncorrelated Gaussian noise, the human observer SNR being scaled down by a factor (denoted efficiency) from the ideal observer SNR [142]. Under these assumptions, we can formulate the conditional probability density function of the vector $\mathbf{g}$ as the

product of the densities of its components

$$\mathrm{pr}(\mathbf{g} \mid H_j) = \left(\frac{1}{2\pi\sigma^2}\right)^{M/2} \prod_{m=1}^{M} \exp\left(-\frac{(g_m - s_{jm})^2}{2\sigma^2}\right) \tag{6.12}$$

where M is the dimension of the data $\mathbf{g}$ and σ^2 is the variance of the noise on each component of $\mathbf{g}$. The likelihood ratio becomes

$$\Lambda(\mathbf{g}) = \prod_{m=1}^{M} \exp\left[\frac{(s_{2m} - s_{1m})g_m}{\sigma^2} - \frac{s_{2m}^2 - s_{1m}^2}{2\sigma^2}\right]. \tag{6.13}$$

The ideal decision rule is to evaluate this expression and compare it to a threshold Λ_c. An equivalent test can be obtained using $\ln\Lambda(\mathbf{g})$: since the logarithm function is monotonic the decision outcome will be unchanged. The test statistic is now formulated as

$$\ln\Lambda(\mathbf{g}) = \sum_{m=1}^{M} \left[\frac{(s_{2m} - s_{1m})g_m}{\sigma^2} - \frac{s_{2m}^2 - s_{1m}^2}{2\sigma^2}\right]. \tag{6.14}$$

Keeping only the hypothesis-dependent terms (the other terms can be combined into the decision threshold) yields

$$\lambda(\mathbf{g}) = \sum_{m=1}^{M} (s_{2m} - s_{1m})g_m \underset{D_1}{\overset{D_2}{\gtrless}} \lambda_c' \tag{6.15}$$

with λ_c' the new decision threshold. The last expression of $\lambda(\mathbf{g})$ can be written using vector notation as

$$\lambda(\mathbf{g}) = \Delta\mathbf{s}^t\mathbf{g}. \tag{6.16}$$

This expression gives the well-known "matched-filter" discriminator in which the expected signal is used as a filter that is correlated with the data.

The resulting decision variable is a linear transformation of the Gaussian data, it is therefore a Gaussian variable as well. The SNR of the test statistic $\lambda(\mathbf{g})$ can thus be used as a figure of merit, since it is related to the AUC. Referring to Equation 6.8, we need to evaluate the mean and variance of $\lambda(\mathbf{g})$ under each hypothesis. The mean under j^{th} hypothesis is easily computed as

$$\langle \lambda(\mathbf{g}) | H_j \rangle = \Delta\mathbf{s}^t\mathbf{s}_j. \tag{6.17}$$

The variance can be expressed as

$$\begin{aligned}\sigma^2_{\lambda,j} &= \left\langle [\lambda(\mathbf{g}) - \left\langle \lambda(\mathbf{g}) \,|H_j\right\rangle]^2 \,|\, H_j \right\rangle \\ &= \left\langle \lambda^2(\mathbf{g}) \,|H_j\right\rangle - \left\langle \lambda(\mathbf{g}) \,|H_j\right\rangle^2 \\ &= \left\langle \Delta\mathbf{s}^t \mathbf{g}\mathbf{g}^t \Delta\mathbf{s} \,|\, H_j \right\rangle - \Delta\mathbf{s}^t \mathbf{s}_j \,\mathbf{s}_j^t \Delta\mathbf{s} \\ &= \Delta\mathbf{s}^t \left\langle (\mathbf{s}_j + \mathbf{n})(\mathbf{s}_j + \mathbf{n})^t \right\rangle \Delta\mathbf{s} - \Delta\mathbf{s}^t \mathbf{s}_j \,\mathbf{s}_j^t \,\Delta\mathbf{s} \\ &= \Delta\mathbf{s}^t \mathbf{K_n} \,\Delta\mathbf{s}.\end{aligned} \tag{6.18}$$

$\mathbf{K_n}$ is the covariance of the noise $<\mathbf{n}\mathbf{n}^t>$, which can can be written as $\mathbf{K_n} = \sigma^2 \mathbf{I}$ with $\mathbf{I}$ the identity matrix.

After simplification between the numerator and denominator, the squared SNR_λ takes the simple form

$$\mathrm{SNR}^2_\lambda = \frac{\Delta\mathbf{s}^t \Delta\mathbf{s}}{\sigma^2} = \frac{||\Delta\mathbf{s}||^2}{\sigma^2}. \tag{6.19}$$

Extension of the model to a L-alternative classification task

We have so far simplified the problem to a 2AFC task. The L-alternative classification task is not as straightforward. Using our previous definitions, the ideal observer is defined as that who chooses the hypothesis H_l associated with the greatest likelihood of the data $\mathrm{pr}(\mathbf{g} \,|\, H_l)$ [142]. The ROC curve is in that case a $(L^2 - l - 1)$-parameter hypersurface in an $(L^2 - 1)$-dimensional probability space. The percentage-correct, numerically derived or experimentally measured, is often chosen as the figure of merit for a L-alternative classification task. The analysis based on the ROC is more complicated and the relation between the AUC and the percentage-correct not obvious.

We formulate here a measure of class separability

$$S = \frac{1}{\sigma^2} \frac{1}{L} \sum_{l=1}^{L} ||\mathbf{s}_l - \bar{\mathbf{s}}||^2. \tag{6.20}$$

This expression is equivalent to the Hotelling trace J derived by Barrett *et al.* [142] for a SKE/BKE problem with zero-mean independent, identical Gaussian noise. Indeed

$$J = \mathrm{tr}[\mathbf{S}_2^{-1} \mathbf{S}_1] \tag{6.21}$$

with tr denoting the matrix trace and $\mathbf{S}_1$ and $\mathbf{S}_2$ the interclass and intraclass scatter

matrices defined as

$$\begin{aligned} \mathbf{S}_1 &= \frac{1}{L}\sum_{l=1}^{L}(\bar{\mathbf{g}}_l - \bar{\mathbf{g}})(\bar{\mathbf{g}}_l - \bar{\mathbf{g}})^t \\ \mathbf{S}_2 &= \frac{1}{L}\sum_{l=1}^{L}\langle(\mathbf{g} - \bar{\mathbf{g}})(\mathbf{g} - \bar{\mathbf{g}})^t|H_l\rangle \end{aligned} \tag{6.22}$$

with $\bar{\mathbf{g}}_l = \langle \mathbf{g}|H_l\rangle$ and $\bar{\mathbf{g}} = \frac{1}{L}\sum_{l=1}^{L}\bar{\mathbf{g}}_l$.

In our case, $\mathbf{S}_2 = \mathbf{K_n}$ and $\bar{\mathbf{g}_l} = \mathbf{s}_l$, thus

$$J = \frac{1}{\sigma^2}\,\mathrm{tr}[\mathbf{S}_1] = \frac{1}{\sigma^2}\,\frac{1}{L}\sum_{l=1}^{L}\mathrm{tr}[(\bar{\mathbf{s}}_l - \bar{\mathbf{s}})(\bar{\mathbf{s}}_l - \bar{\mathbf{s}})^t] = S. \tag{6.23}$$

Relation between the figures of merit and the AO benefit

The two formulae derived above greatly simplify the calculations of the observer performance. Furthermore, as we have seen, the SNR_λ for normal data can be related to the percentage of correctness of a 2AFC task. In our experiments, we measured the contrast of the stimulus required to have a defined percentage of correctness. This contrast threshold c_T is therefore associated with a detectability ${d_T}'$. The contrast was defined as $c = \frac{\Delta L}{L_b}$ with L_b the background luminance and ΔL the luminance difference between the Landolt C and the background. $\Delta\mathbf{s}$ is proportional to ΔL, which in turn is proportional to the contrast for a fixed background as we had it. Denoting SNR_0 the SNR calculated for a contrast of 100%, we can write

$${d_T}'^2 = \mathrm{SNR}_0^2 \times c_T^2. \tag{6.24}$$

The SNR for 100% contrast is proportional to the inverse of the measured contrast threshold or proportional to the contrast sensitivity of a 2AFC task. In the experiments described in the previous chapter, we measured the AO benefit, that is the ratio of the contrast sensitivity with adaptive optics correction to that without correction of ocular higher-order aberrations. Therefore, more than the absolute values of the model-observer performance figure of merits, the ratio of the figures of merit is of interest for us

$$\mathrm{R}_{\mathrm{SNR}_0} = \frac{\left(\frac{{d_T}'}{c_T}\right)_{correctedcase}}{\left(\frac{{d_T}'}{c_T}\right)_{aberratedcase}}. \tag{6.25}$$

Since the same percentage of correctness was used for the contrast sensitivity measure in both case, $d_T{}'$ is identical in both cases. The ratio $\mathrm{R}_{\mathrm{SNR}_0}$ should be equivalent to the ratio of the 2AFC contrast sensitivities measured in both case.

We have derived two simple expressions for the measure of the performance of the ideal observer in a 2AFC and a L-AFC tasks. We have shown that the figure of merit of the 2AFC, the SNR, can be directly related to the measured contrast sensitivity for that same task. The experimental study was based on a 4AFC method. Therefore, we performed calculations with the $\mathrm{R}_{\mathrm{SNR}_0}$ for a 2AFC task where the observer has to discriminate between two orthogonal directions of the ring; and we also performed calculations with a similarly defined ratio R_{S_0} for the 4AFC task where the four possible orientations of the ring are taken into account. We used these figures of merit to quantify the model-observer performance for the discrimination of the gap of the Landolt ring and compare with the human-observer data. The next section gives the details of the implementation of the calculation and the comparison of the numerical results with the experimental measurements.

6.2 Numerical simulations

Calculation of the data vector

The simulations were implemented in Matlab. The computation of the the OTF was performed from measured wavefront aberrations. Recalling Equation 1.14, the OTF is the Fourier transform of the point spread function PSF

$$\begin{aligned} \mathrm{OTF}(u,v) &= \mathbf{FT}\{\mathrm{PSF}(x,y)\} \\ &= \int_{-\infty}^{+\infty}\int_{-\infty}^{+\infty} \frac{|h(x,y)|^2}{\int_{-\infty}^{+\infty}\int_{-\infty}^{+\infty}|h(x,y)|^2 dxdy} \exp\left[-\tfrac{2\pi i}{\lambda f}(xu+yv)\right] dxdy \end{aligned} \tag{6.26}$$

with f the distance from the pupil plane to the image, that we took to be the nodal distance, $f = 16.7$ mm, and λ the wavelength which was set to be similar to that used in the psychophysical experiments, $\lambda = 550$ nm. $h(x,y)$ is the Fourier transform of the pupil function $P(\xi,\eta)$

$$h(x,y) = \int_{-\infty}^{+\infty}\int_{-\infty}^{+\infty} P(\xi,\eta)\exp\left[-\frac{2\pi i}{\lambda f}(x\xi+y\eta)\right] d\xi d\eta. \tag{6.27}$$

where the pupil function is defined as

$$P(\xi,\eta) = \begin{cases} \exp\left[\frac{2\pi i}{\lambda} W(\xi,\eta)\right] & \text{for } (\xi,\eta) \text{ in the aperture} \\ 0 & \text{elsewhere.} \end{cases} \tag{6.28}$$

$W(\xi,\eta)$ is the wave aberration function, which was reconstructed from the Shack-Hartmann wavefront measurements as described in Chapter 4. The pupil function computation was done with a reconstruction over 35 Zernike polynomials, and a grid of 256×256 pixels. Fast Fourier Transforms were used, with a padding over 1024×1024 pixels. Figure 6.2 shows the MTF, magnitude of the OTF, calculated from the measured aberrations of subject 5 in the experimental study, before and after correction by the AO system. The plot gives the radially averaged profiles of the 2D MTF.

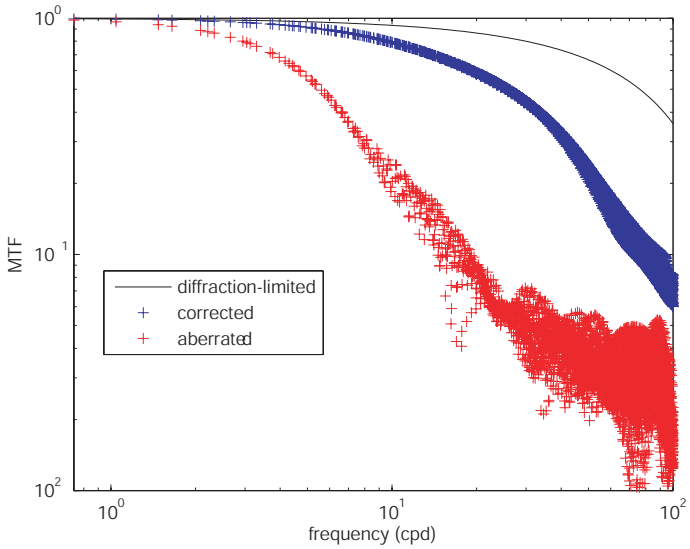

Figure 6.2: Radial profiles of the MTF calculated from the wavefront error measurements of subject 8 over a 6 mm pupil.

The neural filtering was also performed in the Fourier domain. For the channels, we chose to work with difference-of-Gaussians (DOG) functions as they are one of several bandpass profiles that have been used to model spatial-frequency selectivity in the human visual system [143]. We used the radial-frequency profile expressed for the j^{th} frequency peak by Abbey *et al.* [144] as

$$C_j(\rho) = \exp\left[-\frac{1}{2}\left(\frac{\rho}{Q\sigma_j}\right)^2\right] - \exp\left[-\frac{1}{2}\left(\frac{\rho}{\sigma_j}\right)^2\right] \tag{6.29}$$

with Q the bandwidth of the channel (we set it to 1.2), and the standard deviation $\sigma_j = \sigma_0 \times 2^j$ setting the frequency peak. We chose σ_0 such that the peak frequencies of the channels are 2, 4, 8, 16 and 32 cpd. The NTF was constructed as the sum of the channels weighted to fit approximately the overall NTF to experimental neural sensitivity curves in different light regimes taken from the literature [44]. Figure 6.3 shows the channels and the overall neural sensitivity radial profiles constructed from chosen parameters to represent the photopic and scotopic regime. We wish to empha-

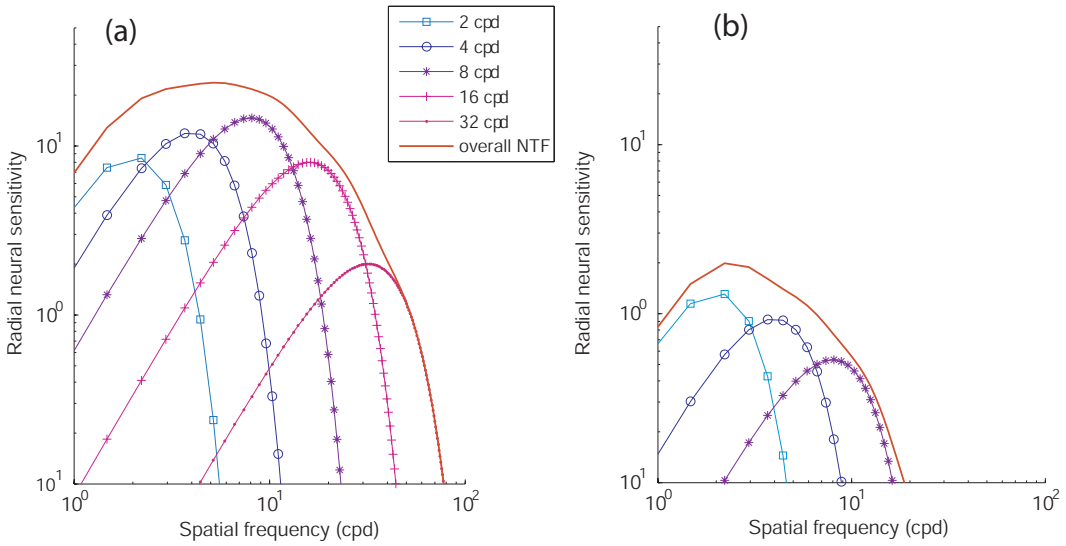

Figure 6.3: Radial profiles of DOG channels and overall NTF curves in the (a) photopic and (b) scotopic regime.

size that this weighting is arbitrary and that the channels, scaling factors, and overall NTF curves constructed are only a very crude approximation to known curves and processes. The important features that can be noticed on the figure are the reduction and the shift towards lower spatial frequencies of the neural sensitivity from the photopic to the scotopic light level. Orientation tuning of the channels are also of importance regarding the orientation discrimination task. These can be obtained if adding separately a factor $\cos(k\theta)_{k=1...K}$ and $\sin(k\theta)_{k=1...K}$ to the channel expression of Equation 6.29. The number K defines the number of orientations chosen. Calculations were performed with $K = 1$ (2 orientations) and $K = 2$ (4 orientations).

An insight of the problem can be gained with the stimulus spectrum amplitude after filtering by the OTF and NTF. As a first crude calculation, the difference between the spectrum amplitude in the direction of the gap and the spectrum amplitude in the direction perpendicular to the gap gives an indication on the separability of the two

orthogonal orientations. These calculations were performed for a Landolt C subtending 15 minutes of arc (i.e. with a gap of 3 minutes of arc). Figure 6.4 shows the calculated amplitude difference of spectrum (ADS) for a Landolt C degraded by ocular aberrations similar to those used in the MTF calculations above, and a for Landolt C corrected (similar wavefront error residual as used above). The computation was per-

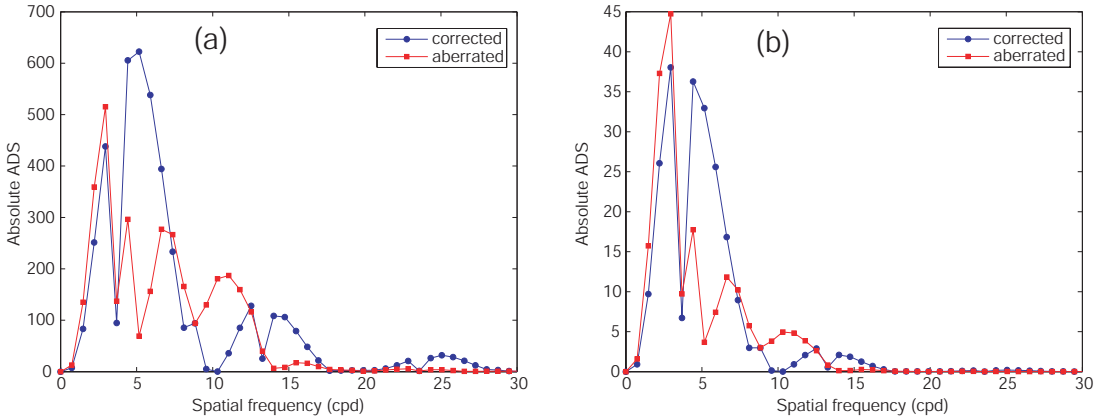

Figure 6.4: Absolute difference between the spectrum magnitude in the direction of the gap and the spectrum magnitude in the orthogonal direction, in the (a) photopic and (b) scotopic regime, for an aberrated Landolt C and a corrected Landolt C.

formed in the photopic and scotopic regimes, using the NTF illustrated in Figure 6.3. The Landolt C spectrum has already been investigated, in particular in relation to foveal crowding. It was found that the peak of the ADS, without optical or neural filtering, is located at about 1.15-1.3 cycles per letter (cpl) [145]. This value, translating in cycles per degree for our stimulus to 4.6-5.2 cpd, approximately corresponds to the peak of the ADS observed for a corrected Landolt C in the photopic regime. Other authors used filtered stimuli to measure the most pertinent object frequency (i.e. the filter frequency providing the best observer performance) for larger Landolt rings, and found values close to 2 cpl for a stimulus of 0.6 degrees [135] and 0.5 degrees [136]. These values correspond to 3.33 cpd and 3.8 cpd respectively. Therefore, it seems that although the most pertinent relative letter spatial frequency (in cpl) increases with the size of the letter, the absolute most pertinent spatial frequency (in cpd) remains approximately stable. This fact, also observed for general letter identification [146], is consistent with the optical and neural filtering, considering the peak of the CSF commonly measured at about 4-8 cpd. Such relation between the spatial-frequency characteristics of letter identification and the CSF was demonstrated by Chung *et al.* [147] who compared experiments with band-pass filtered letters and model performance simulations based on the observer's measured CSF at different eccentricities. As the NTF drops in the scotopic regime, the peak frequency in the corrected stimulus ADS

of Figure 6.4 shifts towards lower frequencies. One can note that the ADS peak frequency for the aberrated Landolt ring is dramatically different. It might have been interesting to investigate this point further with experimental measurements of visual performance while using filtered stimuli. The analysis through the ADS peak frequency remains however limited, since the observer probably uses more information to perform the task. As we are interested in the AO benefit in different light regimes, one can look at the difference between the corrected and aberrated absolute ADS in the photopic and scotopic regimes, as illustrated on the figure. It can be noted that even in the photopic condition, the ADS is mainly concentrated below 10 cpd which is not a very high spatial frequency. This is the combination of the stimulus spectrum and the neural attenuation. This observation can already explain why the measured AO benefit in Chapter 5 remained limited to a value of about 2 at the highest level. The comparison between the difference of corrected ADS and the aberrated ADS in the photopic and in the scotopic regime is not easy and again, the two radial sections plotted probably do not reflect all the information used by the observer.

Simulated AO benefit in the photopic and scotopic regimes

As illustrated by Equations 6.19 and 6.20, the signal-to-noise ratio SNR and the separability measure S take simple forms for the ideal observer. When taking the relative ratio of the figures of merit in the corrected and aberrated cases, the calculation further simplifies if we assume identical noise for the corrected/non-corrected case

$$\begin{aligned} \mathrm{R}_{\mathrm{SNR}_0} &= \frac{||\Delta\mathbf{s}||^2_{correctedcase}}{||\Delta\mathbf{s}||^2_{aberratedcase}} \\ \mathrm{R}_{\mathrm{S}_0} &= \frac{\sum_{l=1}^{L} ||\mathbf{s}_l - \bar{\mathbf{s}}||^2_{correctedcase}}{\sum_{l=1}^{L} ||\mathbf{s}_l - \bar{\mathbf{s}}||^2_{aberratedcase}}. \end{aligned} \tag{6.30}$$

The Euclidian difference can be easily calculated from the data vector $\mathbf{s}$. As we mentioned earlier, several approaches were investigated for the derivation of the final real data vector that would be used to produce a test statistic by the observer. These included the magnitude of the Fourier transform of the retinal image, the retinal image and the channel outputs, as summarised in Equation 6.4. The task set in the experimental study was to discriminate the orientation of the gap of a Landolt ring between four possibilities. It must be pointed out here that the analysis given above based on the ADS can be applied to the discrimination between two orthogonal orientations of the gap, but not to the discrimination between two opposite orientations, as these would translate into same magnitude and opposite phase. Therefore, we followed

the approach taken by Anderson and Thibos [148] when dealing with the Fourier image data vector (first expression given in Eq. 6.4): we kept the magnitude as well as the phase of each data vector $\mathbf{s}$ before computing the Euclidian magnitude difference $|||\Delta\mathbf{s}|||^2$. It can be noted that according to Parseval's theorem, the result of this Euclidian difference should be the same whether we express the data vector in the Fourier domain as we do, or in the spatial domain, $\mathbf{FT^{-1}}\{\mathbf{s}\}$. When using orientated channels, however, it was found that such filters would give results inconsistent with experimental results if applied to a 4AFC task. A further investigation would probably be needed for the issue of the Fourier domain analysis for such a task, where the observer has to discriminate between different orientations and different phases.

We computed the numerical AO benefit for a 2AFC task (R_{SNR_0}) using the two different data vector forms, and the numerical AO benefit for a 4AFC task (R_{S_0}) using the overall filter only. The first two tables below show the results obtained with the measured aberrations of subject 5 and the photopic and scotopic neural filtering as detailed previously. The terms "Channelised 1" and "Channelised 2" refer to the models

Table 6.2: AO benefit computed from the model-observer performance in different light regimes, based on aberrometry data of subject 5, and a 2AFC model.

Light regime	2AFC model AO benefit		
	Channelised 1	Channelised 2	Fourier image
photopic	2.18	1.83	1.73
scotopic	1.77	1.50	1.32

Table 6.3: AO benefit computed from the model-observer performance in different light regimes, based on aberrometry data of subject 5 and a 4AFC model.

Light regime	Fourier image 4AFC model AO benefit
photopic	1.75
scotopic	1.34

using channels filtering with 2 and 4 orientations respectively; the term "Fourier image" refers to the model producing a data vector from an overall filtered Fourier image. The results show good consistency amongst the different models. In particular, it is not surprising that the higher the number of orientations chosen for the channelised model, the closer the results are to those given by the "Fourier image"model which by definition includes all orientations information. It can be analysed in the following: while for the corrected case, most of the stimulus information is concentrated in a few orientations (in particular the direction of the gap), for the aberrated

case, the stimulus information is spread over more orientations, therefore the model benefits from a higher number of channels. The values also confirm the association made between the 2AFC performance and the 4AFC performance in the orientation discrimination task of a Landolt C, although more work would be needed to derive a full channelised 4AFC model. A striking feature is that all models show a decrease of the AO benefit in the scotopic range as compared to the photopic range.

These results can be compared to the data experimentally obtained with subject 5 with a 4AFC procedure, as presented in Chapter 5. They are summurised in the table below. The quantitative comparison between the model-observer and the human-

Table 6.4: AO benefit measured with subject 5 for the Landolt C contrast sensitivity in different light regimes. The means and standard errors of the mean are given.

Light regime	Light level (Td)	4AFC measured AO benefit
photopic	1000	1.63 ± 0.08
photopic	100	1.69 ± 0.08
mesopic	10	1.54 ± 0.20
mesopic	1	1.15 ± 0.14
scotopic	0.3	1.06 ± 0.14

observer AO benefit is difficult, due to the approximations made in the model. In particular, the neural filtering was very crudely modeled based on data found in the literature. The given photopic and scotopic regimes of the model calculations can by no means be assigned to particular light levels, such as those tested in the experimental study. Another factor that can affect the quantitative results, beyond the accuracy in the aberrations measurement, is the Stiles-Crawford effect and its impact on image quality that we mentioned in Chapter 1. The Stiles-Crawford effect can be modeled as an apodisation in the pupil plane, effectively by using a Gaussian weighting function in the pupil function. Since no individual data was available, preliminary calculations were performed with a generic function found in the literature [28], similar to that used in Chapter 5. They showed a slightly smaller simulated AO benefit when the Stiles-Crawford effect was taken into account, as compared to the case when it was not taken into account. Again, the actual values are not of much significance, since the impact on image quality is dependent on the position of the Stiles-Crawford peak, which is highly subject-dependent. A more thorough investigation would require the measurement of the individual Stiles-Crawford effect of subject 5 before including it in the calculations. In spite of all these approximations, one can note that the numerical model-observer AO benefit at the highest light level is for all cases quite close to the maximum AO benefit measured for subject 5. It confirms the observation made

on Figure 6.4 that the ADS even in the photopic regime is concentrated in spatial frequencies below 10 cpd. Calculations without neural filtering led to a model-observer AO benefit of 1.88 with a "Fourier image" model; therefore the stimulus spectrum itself limits the gain expected with AO correction.

The numerical simulations confirmed what was observed with the experimental measurements, which is that the effect of higher-order ocular aberrations on visual performance decreases as the neural sensitivity drops, that is when light level is decreased. These results are explained by the fact that the neural sensitivity limits the spatial frequency range of the stimulus spectrum that is used for the visual task. The resulting stimulus spatial frequency characteristics are dependent on the optical as well as the neural filtering of the eye. As the light level is decreased, the neural sensitivity drops and shifts towards lower spatial frequencies, where the impact of the higher-order aberrations on the stimulus spectrum are lower, as shown on Figure 6.2. This interpretation is valid for a large spectrum stimulus, however it does not hold for a stimulus comprising a single spatial frequency.

Comparison with a narrow spectrum stimulus

Visual stimuli, since they are spatially limited, cannot by definition be represented by a single spatial frequency. However, gratings, or Gabor stimuli which are often used for contrast sensitivity measurements, contain a narrow spatial frequency spectrum quite different to the spectrum of the Landolt C that we have considered so far.

We therefore performed simulations with a Gabor stimulus, as defined in Section 4.2: a 10 cpd cosine function weighted by a Gaussian envelope of a 0.5 degrees standard deviation. We computed the 2AFC discrimination task AO benefit with our ideal-observer. The OTF was again calculated based on aberrations measurements of subject 5. As expected, such a narrow spectrum stimulus shows very small decrease

Table 6.5: AO benefit computed from the model-observer performance in different light regimes, based on aberrometry data of subject 5 and a 2AFC grating discrimination model.

Light regime	2AFC model AO benefit		
	Channelised 1	Channelised 2	Fourier image
photopic	2.98	2.46	2.85
scotopic	2.96	2.44	2.82

of the AO benefit when the light level is decreased. Contrary to the previous calcula-

tions, the AO benefit calculated with the overall NTF filtering is not lower than that calculated with the channels. This observation may have an explanation in the fact that the channels were centered at 2, 4, 8, 16 and 32 cpd, therefore not optimised for the 10 cpd stimulus. The loss in contrast sensitivity at this particular frequency, due to the optical aberrations, would have therefore been underestimated.

Further experiments were carried out with subject 5 to compare with the simulations for this particular stimulus. Measurements were performed in a smaller range of retinal illuminance levels, since as we have explained it in Chapter 4, the gratings could only be generated with sufficient resolution with the monitor, which had a limited maximum luminance. Surprisingly, the experimental results show a decrease of

Table 6.6: AO benefit measured with subject 5 for a 10 cpd grating contrast sensitivity at different light levels. The means and standard errors of the mean are given.

Light regime	Light level (Td)	2AFC measured AO benefit
photopic/mesopic	50	2.98 ± 0.61
mesopic	15	2.54 ± 0.54
mesopic	5	2.07 ± 0.26

the AO benefit as the light level is decreased. The disagreement between the experimental measurements and the model rises questions about the validity of the model. We may argue that the experimental results were only obtained for one subject, and that more subjects should be tested within a broader range of light levels before any conclusion can be drawn. In particular, the standard errors of the mean are higher for this visual task than for the Landolt C orientation discrimination task, although the number of measurements was the same (5 at each light level). We also wish to emphasize again that the numerical approximations in our model yield an uncertainty difficult to estimate. However, we must also consider that the model may not encompass all or not well enough the mechanisms used by the human observer for the tasks considered. A suggestion could be to consider a non-linear model, with a form of threshold imposed on the data vector. Further investigations would be required to fully understand these results.

6.3 Preliminary conclusions

We derived an ideal-observer model and the associated figures of merit for the 2AFC and 4AFC classification tasks. Numerical calculations of the AO benefit based

on the figures of merit confirmed the interpretation of the experimentally measured decrease of the AO benefit with a decrease of the light level. The results suggest that the neural sensitivity strongly affects the spatial-frequency characteristics of the stimulus that are used for a visual task. Therefore the effect of higher-order aberrations on visual performance should be regarded in relation with the neural sensitivity. The correlation between the model- and the human-observer performance could not however be confirmed for a narrow spectrum stimulus. It proved the high dependence of the interpretation of the neural processes on the stimulus and task considered. Caution must therefore be taken for any strong conclusion.

A more thorough study would imply the calculation of the absolute contrast sensitivities based on statistical expectations of many noise realisations at different contrast values. Higher calculation resolution could also affect the results. This intensive computational method was beyond the scope of the present project, where only an estimation of the performance of the observer for a specific task was needed. Better accuracy would also be guaranteed with individual neural sensitivity and perhaps Stiles-Crawford effect data. The analysis presented in the Thesis aimed for a crude interpretation of the experimental results obtained, through the derivation and understanding of a model-observer for the visual task considered. The combined effect of higher-order aberrations and neural sensitivity under different ambient light levels was investigated and the results brought some preliminary answers to a complex problem.

Chapter 7

Conclusion

The work presented in this Thesis is part of a recent combined optics/vision research effort which led to demonstrate that adaptive optics (AO) techniques can provide a valuable tool for vision research, allowing to bypass the limitations due to ocular aberrations. Several competitive ocular AO systems have been built and tested around the world, such as the setup used in this Thesis.

Capabilities of ocular adaptive optics

We presented a thorough analysis and some optimisation of the main components of an existing AO system (wavefront sensor, wavefront correction, and control algorithm) with the aim of tackling the major issues of the application of adaptive optics techniques to the correction of higher-order aberrations. This allowed us to demonstrate a performance close to diffraction-limit, yielding a wavefront error residual ranging from 0.05 μm rms to 0.1 μm rms over a 6-mm pupil for young, healthy, well-corrected eyes.

The AO correction achieved in this project appeared sufficient for the experiments carried out, in particular a comparison between a static correction and a dynamic correction showed no statistically significant difference on the impact on visual performance, as long as the alignment was held. Other applications may require a finer dynamic correction. Ocular adaptive optics improvements are still possible: more importantly than the current limitations of the wavefront sensor, the constantly evolving

technologies of corrective elements may bring the possibility of a finer correction. In particular, as part of the project, a method was described and used to perform a task-based assessment of deformable mirrors for ocular AO. We have seen the dramatic effect that the associated characteristics of deformable mirrors (number of actuators, stroke and width of the actuators influence functions) can have on the fitting of typical ocular aberrations; the search for an optimum corrector is not over yet. The optimised solution may come from the combination of two correctors [100]. A higher level of dynamic correction would also probably require higher speed, in particular smaller delays, in the closed-loop systems. Following the advancements of AO applied to astronomy, it would be interesting to investigate the implementation of non-classical control algorithms, optimised and predictive for the spatial and temporal characteristics of ocular aberrations. However the optimisation is constrained by the limited knowledge available on the nature of ocular aberrations and their dynamics. The most important issue of ocular AO is probably the inter-subject high variability of spatial and temporal aberrations characteristics, resulting in great variability of the AO performance. A system can give a very low residual wavefront error rms (less than 0.5 μm) for a very stable subject and twice the value for another one, though the initial amount of aberrations is equivalent. The motivation could be to adapt the correction for more "difficult" subjects, i.e. on an individual basis, rather than to globally optimise the system. The analysis of a sufficient amount of open-loop recorded data of the subject's wavefront aberrations could be the base of such optimisation. Wavelet analysis is a tool appropriate to the non-stationarity of ocular aberrations.

Another challenge for ocular AO is the extension of the field of correction. Only a few case-studies have presented the variations of ocular aberrations with the field angle [149, 150], and these must be extended to quantify precisely the isoplanetic patch of the eye. Besides technical issues (several correctors, complex control algorithm), a better modelling of the eye would be required for an efficient implementation of multi-conjugate adaptive optics if necessary. Wide-field AO could benefit mainly retinal imaging.

Higher-order aberrations and visual functions

The AO system was used for visual experiments with the aim of gaining a better understanding of the limitations of functional vision. This Thesis focussed on the effects of ocular higher-order (HO) aberrations on functional visual performance. Technical issues and possible errors in the experimental setup were emphasised, as well as the

efficient use of psychophysical methods, and the choice of an appropriate visual test, in that case a contrast acuity test. We showed that the impact of HO aberrations on vision is moderated by neural sensitivity. We measured an increase of the HO aberrations with pupil size, and independently a decrease of the effects of HO aberrations on contrast acuity as the light level was decreased. We analysed these results as being caused by the drop in neural sensitivity at low light level, due to larger spatial summation, the intrusion of rod signals and the reduction of signal-to-noise ratio. A model of the observer performance, based on a classical approach of the discrimination visual task but separating the optical and neural processing stages, confirmed this analysis. The data taken at different light levels and pupil sizes made it possible to quantify the expected benefit gained by young healthy subjects in everyday vision when their higher-order aberrations are corrected. With the combined effect of pupil size, hence ocular aberrations magnitude, and neural sensitivity, this benefit proved limited in all light regimes. The results should moderate the enthusiasm created by the possibility of high-order ophthalmic correction through customised intra-ocular lenses, contact lenses, or refractive surgery.

Although novel results were presented, they only give small improvement in the knowledge of vision functions, and perhaps raise new questions. In particular, a specific visual test of contrast acuity was investigated, and a full analysis of visual performance probably also requires contrast sensitivity tests. It would be of interest to determine why our vision model did not agree with the preliminary experimental results obtained for contrast sensitivity. The use of a set of different stimuli, including fine spectrum gratings or filtered alphanumeric characters may help to answer this issue. Other factors in visual performance, such as scatter, the Stiles-Crawford effect or neural adaptation were mentioned and could be further investigated. For example, a full set of individual data for the ocular aberrations, the scatter, the Stiles-Crawford effect and the neural sensitivity would be very valuable to help disentangling the different factors affecting visual performance. Furthermore, it could be interesting to investigate the correlation between the Stiles-Crawford effect and ocular aberrations. Marcos and Burns found no statistically significant correlation between the Stiles-Crawford luminosity attenuation across and the optical degradation, but the data indicated that pupil areas near the peak of the luminosity function have better optical quality than regions far from the peak [30].

A step further in the understanding of optical limitations to the visual functions would be the study of polychromatic vision. We focussed in this Thesis on monochromatic wavefront aberrations and image formation; yet the combination of differ-

ent wavelengths in the visual system is still an open topic. Calculations of the cone polychromatic optical transfer function (OTF) based on the monochromatic OTF, the longitudinal and transverse chromatic aberrations and the cone spectral sensitivity, have shown that higher-order aberrations tend to balance the relative optical degradation perceived by the three different classes of cones, effectively reducing the chromatic blur on S cones as compared to L and M cones [26]. It was also predicted [127] and measured [39] that the overall polychromatic OTF of the eye benefits significantly less from the correction of HO aberrations than does the monochromatic OTF. Firstly, the dependence of ocular aberrations (apart from defocus) with wavelength still requires clarification. Then polychromatic stimuli could be tested with the AO system, or even their combined monochromatic AO corrected components (depending on the wavelength dependence of higher-order aberrations, a single deformable mirror with separate focus adjustment arms may then be sufficient).

The concept of neural adaptation, that is of the subject to perform a form of neural compensation for the known image degradation introduced by their aberrations, has been recently suggested and again pointed out from our experimental results. Artal *et al.* measured a better subjective image sharpness with the subject's own ocular aberrations, than with a rotated version of the same wavefront error [138]. We found that a subject who had a low amount of higher-order aberrations performed better to our contrast acuity test with her own aberrations than after AO correction (leading to a higher optical transfer function). One could test further this concept, typically with other visual tests such as contrast sensitivity, and under different conditions. Indeed, the optical aberrations are dependent on the pupil size and accommodation; therefore one could expect different levels of neural adaptations in different conditions, unless an average compensation is performed. One could also wonder what are the temporal scales of such neural adaptation. The advantage of the AO system is that not only can ocular aberrations be corrected, they can also be induced; one can test a whole set of different combinations of Zernike polynomials subtracted or added to an initial wavefront error. This could help testing neural adaptation and any possible structural or functional correlation between Zernike polynomials.

Clinical applications of psychophysical adaptive optics

The ideas developed above are just a small sample of the broad range of topics in the fundamental understanding of visual functions that could be explored with adaptive optics techniques. Another application of great importance would be the implemen-

tation of psychophysical adaptive optics systems in clinical environment. Recently, Makous *et al.* demonstrated the benefit that could be gained from an adaptive optics correction of ocular aberrations in microperimetry systems [110]. They were able to send flashes of light measuring 3 μm diameter at half height to detect microscotomas on the retina, that could not be detected with standard microperimetry. This study shows that the implementation of AO microperimeters holds exciting promises in terms of ocular disease diagnosis, such as glaucoma or age-related maculopathy, or other visual deficiencies. The clinical utility of high-resolution retinal imaging systems based on AO technology is currently being investigated [151, 152]; clinical tests of psychophysical AO systems shoudl logically follow. In particular, the association (simultaneous or sequential) of both high-resolution retinal imaging and high-resolution visual tests may be of great interest for disease diagnostic and follow-up.

It seems however that ocular AO is a very sensitive technique that still requires regular control and adjustments from an experienced user. As pointed out earlier, the good performance of AO systems on any random subject, in particular one that might be ill-at-ease due to a pathology, cannot yet be guaranteed. The utility of AO psychophysical tests in clinical environment requires to be thoroughly investigated, through a collaboration between physicists, vision scientists and clinicians.

Bibliography

[1] M. S. Smirnov. Measurement of the wave aberrations of the eye. *Biophysics*, 6:766–795, 1961.

[2] J. Liang, D. R. Williams, and D. T. Miller. Supernormal vision and high-resolution retinal imaging through adaptive optics. *J. Opt. Soc. Am. A*, 14(11):2884–2892, 1997.

[3] A. Gullstrand. *Handbuch der Physiologischen Optik*, page 299. Voss, Hamburg, 3^{rd} edition, 1909.

[4] P. L.Kaufman and A. Alm. *Adler's physiology of the eye: clinical application*. Mosby-Year Book Inc., 11830 Westline Industrial Drive, St. Louis, Missouri 63146, 10th edition, 2003.

[5] M. Born and E. Wolf. *Principles of Optics*. Pergamon Press, 198 Madison Avenue, New York, New York 10016-4314, 1990.

[6] L. N. Thibos, R. A. Applegate, J. T. Schwiegerling, and R. Webb. Standards for reporting optical aberrations of eyes. *J. Ref. Surg.*, 18:652–660, 2000.

[7] P. Artal, A. Guirao, E. Berrio, and D. R. Williams. Compensation of corneal aberrations by the internal optics in the human eye. *J. Vis.*, 1(1):1–8, 2001.

[8] J. E. Kelly, T. Mihashi, and H. C. Howland. Compensation of corneal horizontal/vertical astigmatism, lateral coma, and spherical aberration by internal optics of the eye. *J. Vis.*, 4(4):262–271, 2004.

[9] J. Porter, A. Guirao, I. G. Cox, and D. R. Williams. Monochromatic aberrations of the human eye in a large population. *J. Opt. Soc. Am. A*, 18(8):1793–1803, 2001.

[10] L. N. Thibos, X. Hong, A. Bradley, and X. Cheng. Statistical variation of aberration structure and image quality in a normal population of healthy eyes. *J. Opt. Soc. Am. A*, 19(12):2329–2348, 2002.

[11] J. F. Castejón-Mochón, N. López-Gil, A. Benito, and P. Artal. Ocular wave-front aberration statistics in a normal young population. *Vision Res.*, 42(13):1611–1617, 2002.

[12] M. P. Cagigal, V. F. Canales, J. F. Catejón-Mochón, P. M. Prieto, N. López-Gil, and P. Artal. Statistical description of wave-front aberration in the human eye. *Opt. Lett.*, 27(1):37–39, 2002.

[13] J. Liang and D. R. Williams. Aberrations and retinal image quality of the normal human eye. *J. Opt. Soc. Am. A*, 14(11):2873–2883, 1997.

[14] W. N. Charman and G. Heron. Fluctuations in accommodation; a review. *Ophthal. Physiol. Opt.*, 8:153–164, 1988.

[15] H. Hofer, P. Artal, B. Singer, J. L. Aragon, and D. R. Williams. Dynamics of the eye's wave aberration. *J. Opt. Soc. Am. A*, 18(3):497–506, 2001.

[16] L. Diaz-Santana, C. Torti, I. Munro, P. Gasson, and C. Dainty. Benefit of higher closed-loop bandwidths in ocular adaptive optics. *Opt. Express*, 11(20):2597–2605, 2003.

[17] T. Nirmaier, G. Pudasaini, and J. Bille. Very fast wave-front measurements at the human eye with a custom cmos-based hartmann-shack sensor. *Opt. Express*, 11(21):2704–2716, 2003.

[18] K. M. Hampson, I. Munro, C. Paterson, and J. C. Dainty. Weak correlation between the aberrations dynamics of the human eye and the cardiopulmonary system. *J. Opt. Soc. Am. A*, 22(7):1241–1250, 2005.

[19] A. Dubra, C. Paterson, and C. Dainty. Study of the tear topography dynamics using a lateral shearing interferometer. *Opt. Express*, 12(25):6278–6288, 2004.

[20] S. Gruppetta, F. Lacombe, and P. Puget. Study of the dynamic aberrations of the human tear film. *Opt. Express*, 13(19):7631–7636, 2005.

[21] K. Y. Li and G. Yoon. Changes in aberrations and retinal image quality due to tear film dynamics. *Opt. Express*, 14(25):12552–12559, 2006.

[22] P. Artal. Calculations of two-dimensional foveal retinal images in real eyes. *J. Opt. Soc. Am. A*, 7(8):1374–1381, 1990.

[23] J. C. He, S. A. Marcos, and S. A. Burns. Monochromatic aberrations in the accommodated human eye. *Vision Res.*, 40(1):41–48, 2000.

[24] J. S. McLellan, S. Marcos, and S. A. Burns. Age-related changes in monochromatic wave aberrations of the human eye. *Invest. Ophthalmol. Visual Sci.*, 42(6):1390–1395, 2001.

[25] J. S. McLellan, P. M. Prieto, S. Marcos, and S. A. Burns. Effects of interactions among wave aberrations on optical image quality. *Vision Res.*, 46(18):3009–3016, 2006.

[26] J. S. McLellan, S. Marcos, P. M. Prieto, and S. A. Burns. Imperfect optics may be the eye's defence against chromatic blur. *Nature*, 417:174–176, 2002.

[27] W. S. Stiles and B. H. Crawford. The luminous efficieny of rays entering the eye pupil at different position. *Proc. R. Soc. London*, 112:428–450, 1933.

[28] R. A. Applegate and V. Lakshminarayanan. Parametric representation of stiles-crawford functions: normal variation of peak location and directionality. *J. Opt. Soc. Am. A*, 10(7):1611–1623, 1993.

[29] B. Vohnsen, I. Iglesias, and P. Artal. Guided light and diffraction model of human-eye photoreceptors. *J. Opt. Soc. Am. A*, 22(11):2318–2328, 2005.

[30] S. Marcos and S. A. Burns. On the symmetry between eyes of wavefront aberration and cone directionality. *Vision Res.*, 40(18):2437–2447, 2000.

[31] L. N. Thibos, F. E. Cheney, and D. J. Walsh. Retinal limits to the detection and resolution of gratings. *J. Opt. Soc. Am. A*, 4(8):1524–1529, 1987.

[32] A. Rose. The sensitivity performance of the human eye on an absolute scale. *J. Opt. Soc. Am.*, 38(2):196–208, 1948.

[33] A. Stockman and L. T. Sharpe. Into the twilight zone: the complexities of mesopic vision and luminous efficiency. *Ophthal. Physiol. Opt.*, 26:225–239, 2006.

[34] R. L. De Valois and K. K. De Valois. *Spatial Vision*. Oxford University Press, 198 Madison Avenue, New York, New York 10016-4314, 1990.

[35] M. A. Arnulf and M. O. Dupuy. La transmission des contrastes par le système optique de l'oeil et les seuils de contrastes retininines. *C. R. Acad. Sci. Paris*, 250:2757–2759, 1960.

[36] Y. Le Grand. Sur la mesure de l'acuité visuelle au moyen de franges d'interference. *C. R. Acad. Sci. Paris*, 200:490–491, 1935.

[37] A. Guirao, J. Porter, D. R. Williams, and I. G. Cox. Calculated impact of higher-order monochromatic aberrations on retinal image quality in a population of human eyes. *J. Opt. Soc. Am. A*, 19(1):1–9, 2002.

[38] F. W. Campbell and D. G. Green. Optical and retinal factors affecting visual resolution. *J. Physiol. (Lond.)*, 181:576–593, 1965.

[39] G. Y. Yoon and D. R. Williams. Visual performance after correcting the monochromatic and chromatic aberrations of the eye. *J. Opt. Soc. Am. A*, 19(2):266–275, 2002.

[40] D. R. Williams. Visibility of interference fringes near the resolution limit. *J. Opt. Soc. Am. A*, 11(12):1087–1093, 1988.

[41] A. S. Patel. Spatial resolution by the human visual system. the effect of mean retinal illuminance. *J. Opt. Soc. Am.*, 56(5):689–694, 1966.

[42] F. L. Van Nes and M. A. Bouman. Spatial modulation transfer in the human eye. *J. Opt. Soc. Am.*, 57(3):401–406, 1967.

[43] A. Van Meeteren and J. J. Vos. Resolution and contrast sensitivity at low luminances. *Vision Res.*, 12(5):825–833, 1972.

[44] N. J. Coletta and V. Sharma. Effects of luminance and spatial noise on interferometric contrast sensitivity. *J. Opt. Soc. Am. A*, 12(10):2244–2251, 1995.

[45] F. W. Campbell and A. H. Gregory. Effect of size of pupil on visual acuity. *Nature*, 187:1121–1123, 1960.

[46] H. W. Babcock. The possibility of compensating astronomical seeing. *Pub. Astr. Soc. Pac.*, 65:229–236, 1953.

[47] J. W. Hardy, J. E. Lefebvre, and C. L. Koliopoulos. Real-time atmospheric compensation. *J. Opt. Soc. Am.*, 67:360–369, 1977.

[48] G. Rousset, J. C. Fontanella, P. Kern, P. Gigan, F. Rigaut, and P. Lena. First diffraction-limited astronomical images with adaptive optics. *Astron. Astrophys.*, 230:29–32, 1990.

[49] A. W. Dreher, J. J. Bille, and R. N. Weinreb. Active optical depth resolution improvement of the laser tomographic scanner. *Appl. Opt.*, 28(4):804–808, 1989.

[50] R. Navarro M. A. Losada. Aberrations and relative efficiency of light pencils in the living human eye. *Optom. Vis. Sci.*, 74:540–547, 1997.

[51] F. Berny. Etude de la formation des images rétiniennes et détermination de l'aberration de sphéricité de l'œil humain. *Vision Res.*, 9(8):979–990, 1969.

[52] G. Walsh, W. N. Charman, and H. C. Howland. Objective technique for the determination of monochromatic aberrations of the huamn eye. *J. Opt. Soc. Am. A*, 1(9):987–992, 1984.

[53] H. Howland and B. Howland. A subjective method for the measurement of monochromatic aberrations of the eye. *J. Opt. Soc. Am. A*, 67(11):1508–1518, 1977.

[54] J. Santamaría, P. Artal, and J. Bescós. Determination of the point-spread function of human eyes using a hybrid optical-digital approach. *J. Opt. Soc. Am. A*, 4(6):1109–1114, 1987.

[55] P. Artal, J. Santamaría, and J. Bescós. Retrieval of the wave aberration of the human eyes from actual point-spread function data. *J. Opt. Soc. Am. A*, 5(8):1201–1206, 1988.

[56] F. Flamant. Etude de la répartition de la lumière dans l'image rétinienne d'une fente. *Rev. Opt. Théor. Instrum.*, 34:433–459, 1955.

[57] P. Artal, S. Marcos, R. Navarro, and D. R. Williams. Odd aberrations and double-pass measurements of retinal image quality. *J. Opt. Soc. Am. A*, 2(12):195–201, 1995.

[58] L. Diaz-Santana and J. C. Dainty. Effects of retinal scattering in the ocular double-pass process. *J. Opt. Soc. Am. A*, 18(7):1437–1444, 2001.

[59] J. Liang, B. Grimm, S. Goelz, and J. F. Bille. Objective measurement of wave aberrations of the human eye with the use of a Hartmann-Shack wave-front sensor. *J. Opt. Soc. Am. A*, 11(7):1949–1957, 1994.

[60] F. Roddier. *Adaptive optics in astronomy*. Cambridge University Press, Cambridge, U.K., 1999.

[61] S. Bará. Measuring eye aberrations with hartmann-shack wave-front sensors: Should the irradiance distribution across the eye pupil be taken into account? *J. Opt. Soc. Am. A*, 20(12):2237–2245, 2003.

[62] L. Llorente, L. Diaz-Santana, D. Lara-Saucedo, and S. Marcos. Aberrations of the human eye in visible and near infrared illumination. *Optom. Vis. Sci.*, 80(1):26–35, 2003.

[63] P. M. Prieto and F. Vargas-Martín. Analysis of the performance of the hartmann-shack sensor in the human eye. *J. Opt. Soc. Am. A*, 17(8):1388–1398, 2000.

[64] T. O. Salmon, L. N. Thibos, and A. Bradley. Comparison of the eye's wave-front aberration measured psychophysically and with the shack-hartmann wave-front sensor. *J. Opt. Soc. Am. A*, 15(9):2457–2465, 1998.

[65] E. Moreno-Barriuso and R. Navarro. Laser ray tracing versus hartmann-shack sensor for measuring optical aberrations in the human eye. *J. Opt. Soc. Am. A*, 17(6):974–985, 2000.

[66] I. Iglesias, R. Ragazzoni, Y. Julien, and P. Artal. Extended source pyramid wave-front sensor for the human eye. *Opt. Express*, 10(9):419–428, 2002.

[67] S. R. Chamot, C. Dainty, and S. Esposito. Adaptive optics for ophthalmic applications using a pyramid wavefront sensor. *Opt. Express*, 14(2):518–526, 2006.

[68] A. Dubra, C. Paterson, and C. Dainty. Double lateral shearing interferometer for the quantitative measurement of tear film topography. *Appl. Opt.*, 44(7):1191–1199, 2005.

[69] S. Gruppetta, L. Koechlin, F. Lacombe, and P. Puget. Curvature sensor for the measurement of the static corneal topography and the dynamic tear film topography in the human eye. *Opt. Lett.*, 30(20):2757–2759, 2005.

[70] F. Díaz-Doutón, J. Pujol, M. Arjona, and S. O. Luque. Curvature sensor for ocular wavefront measurement. *Opt. Lett.*, 31(15):2245–2247, 2006.

[71] M. A. A. Neil, M. J. Booth, and T. Wilson. A new modal wave-front sensor: a theoretical analysis. *J. Opt. Soc. Am. A*, 17(6):1098–1107, 2000.

[72] A. Roorda, F. Romero-Borja, W. J. Donnelly III, H. Queener, T. J. hebert, and M. C. W. Campbell. Adaptive optics scanning laser ophthalmoscopy. *Opt. Express*, 10(9):405–412, 2002.

[73] Y. Zhang, J. Rha, R. S. Jonnal, and D. T. Miller. Adaptive optics parallel spectral domain optical coherence tomography for imaging the living retina. *Opt. Express*, 13(12):4792–4811, 2005.

[74] M. Glanc, E. Gendron, F. Lacombe, D. Lafaille, J.-F. Le Gargasson, and P. Léna. Towards wide-field retinal imaging with adaptive optics. *Opt. Commun.*, 230:225–238, 2004.

[75] R. J. Zawadzki, S. M. Jones, S. S. Olivier, M. Zhao, B. A. Bower, J. A. Izatt, S. S. Choi, S. Laut, and J. S. Werner. Adaptive-optics optical coherence tomography for high-resolution and high-speed 3d retinal in vivo imaging. *Opt. Express*, 13(21):8532–8546, 2005.

[76] G. Vdovin and P. M. Sarro. Flexible mirror micromachined in silicon. *Appl. Opt.*, 34(16):2968–2972, 1995.

[77] E. J. Fernández and P. Artal. Membrane deformable mirror for adaptive optics: performance limits in visual optics. *Opt. Express*, 11(9):1056–1069, 2003.

[78] K. M. Hampson, C. Paterson, C. Dainty, and E. A. H. Mallen. Adaptive optics system for investigation of the effect of the aberration dynamics of the human eye on steady-state accommodation control. *J. Opt. Soc. Am. A*, 23(5):1082–1088, 2006.

[79] D. Merino, C. Dainty, A. Bradu, and A. G. Podoleanu. Adaptive optics enhanced simultaneous *en-face* optical coherence tomography and scanning laser ophthalmoscopy. *Opt. Express*, 14(8):3345–3353, 2006.

[80] N. Doble, G. Y. Yoon, L. Chen, P. Bierden, B. Singer, S. Oliver, and D. R. Williams. Use of a microelectromechanical mirror for adaptive optics in the human eye. *Opt. Lett.*, 27(17):1537–1539, 2002.

[81] Y. Zhang, S. Poonja, and A. Roorda. Mems-based adaptive optics scanning laser ophthalmoscopy. *Opt. Lett.*, 31(9):1268–1270, 2006.

[82] E. J. Fernández, L. Vabre, B. Hermann, A. Unterhuber, B. Povazay, and W. Drexler. Adaptive optics with a magnetic deformable mirror: applications in the human eye. *Opt. Express*, 14(20):8900–8917, 2006.

[83] F. Vargas-Martín, P. M. Prieto, and P. Artal. Correction of the aberrations in the human eye with a liquid-crystal spatial light modulator: limits to performance. *J. Opt. Soc. Am. A*, 15(9):2552–2562, 1998.

[84] P. M. Prieto, E. J. Fernández, S. Manzanera, and P. Artal. Adaptive optics with a programmable phase modulator: applications in the human eye. *Opt. Express*, 12(17):4059–4071, 2004.

[85] E. P. Wallner. Optimal wave-front correction using slope measurements. *J. Opt. Soc. Am. A*, 73(12):1771–1776, 1983.

[86] H. Hofer, L. Chen, G. Y. Yoon, B. Singer, Y. Yamauchi, and D. R. Williams. Improvement in retinal image quality with dynamic correction of the eye's aberrations. *Opt. Express*, 8(11):631–643, 2001.

[87] E. Gendron and P. Léna. Astronomical adaptive optics i. modal control optimization. *Astron. Astrophys.*, 291:337–347, 1994.

[88] R. N. Parschall and D. J. Anderson. Linear quadratic gaussian control of a deformable mirror adaptive optics system with time-delayed measurements. *Appl. Opt.*, 32(31):6347–6358, 1993.

[89] C. Dessenne, P.-Y. madec, and G. Rousset. Modal prediction fro closed-loop adaptive optics. *Opt. Lett.*, 22(20):1535–1537, 1997.

[90] E. J. Fernández, I. Iglesias, and P. Artal. Closed-loop adaptive optics in the human eye. *Opt. Lett.*, 26(10):746–748, 2001.

[91] T. Shirai. Liquid-crystal adaptive optics based on feedback interferometry for high-resolution retinal imaging. *Appl. Opt.*, 41(19):4013–4023, 2002.

[92] G. Vdovin, M. Loktev, A. Simonov, V. Kijko, and S. Volkov. Adaptive correction of human-eye aberrations in a subjective feedback loop. *Opt. Lett.*, 30(17):795–797, 2005.

[93] N. López-Gil, H. C. Howland, B. Howland, N. Charman, and R. Applegate. Generation of third-order spherical and coma aberrations by use of radially symmetrical fourth-order lenses. *J. Opt. Soc. Am. A*, 15(9):2563–2571, 1998.

[94] R. Navarro, E. Moreno-Barriuso, S. Bará, and T. Mancebo. Phase plates for wave-aberration compensation in the human eye. *Opt. Lett.*, 25(4):236–238, 2000.

[95] A. Guirao, D. R. Williams, and I. G. Cox. Effect of rotation and translation on the expected benefit of an ideal method to correct the eye's higher-order aberrations. *J. Opt. Soc. Am. A*, 18(5):1003–1015, 2001.

[96] J. Schwiegerling. Wavefront guided lasik. *Opt. Photon. News*, 15:26–29, 2000.

[97] L. E. Marchese, R. Munger, and D. Priest. Wavefront-guided correction of ocular aberrations: are phase plate and refractive surgery solutions equal? *J. Opt. Soc. Am. A*, 22(8):1471–1481, 2005.

[98] J. Holladay, P. Piers, G. Koranyi, M. van der Mooren, and N. Norrby. A new intraocular lens design to reduce spherical aberration of pseudophakic eyes. *J. Ref. Surg.*, 18(6):683–691, 2002.

[99] G. Vdovin, M. Loktev, and A. Naumov. On the possibility of intraocular adaptive optics. *Opt. Express*, 11(7):810–817, 2003.

[100] R. J. Zawadzki, S. S. Choi, J. S. Werner, S. M. Jones, D. Chen, S. S. Olivier, Y. Zhang, J. Rha, B. Cense, and D. T. Miller. Two deformable mirror adaptive opticssystem for *in vivo* retinal imaging with optical coherence tomography. In *Biomedical Optics, Technical Digest (CD) (Optical Society of America, 2006), paper WC2*, 2006.

[101] S. Bará and R. Navarro. Wide-field compensation of monochromatic eye aberrations: expecetd [erformance and design trade-offs. *J. Opt. Soc. Am. A*, 20(1):1–10, 2003.

[102] D. C. Johnston and B. M. Welsh. Analysis of multiconjugate adaptive optics. *J. Opt. Soc. Am. A*, 11(1):394–408, 1994.

[103] P. A. Bedgood, R. Ashman, G. Smith, and A. B. Metha. Multiconjugate adaptive optics applied to an anatomically accurate human eye model. *Opt. Express*, 14(18):8019–8030, 2006.

[104] J. Caroll, D. C. Gray, A. Roorda, and D. R. Williams. Recent advances in retinal imaging with adaptive optics. *Opt. Photon. News*, 16(1):36–42, 2005.

[105] E. J. Fernández and P. Artal. Study on the effects of monochromatic aberrations in the accommodation response by using adaptive optics. *J. Opt. Soc. Am. A*, 22(9):1732–1738, 2005.

[106] L. Chen, P. B. Kruger, H. Hofer, B. Singer, and D. R. Williams. Accommodation with higher-order monochromatic aberrations corrected with adaptive optics. *J. Opt. Soc. Am. A*, 23(1):1–8, 2006.

[107] S. Poonja, S. Patel, L. Henry, and A. Roorda. Dynamic visual stimulus presentation in an adaptive optics scanning laser ophthalmoscope. *J. Ref. Surg.*, 21:575–580, 2005.

[108] H. Hofer, B. Singer, and D. R. Williams. Different sensations from cones with the same photopigment. *J. Vis.*, 5(5):444–454, 2005.

[109] N. M. Putman, H. J. Hofer, N. Doble, L. Chen, J. Carroll, and D. R. Williams. The locus of fixation and the foveal cone mosaic. *J. Vis.*, 5(7):632–639, 2005.

[110] W. Makous, J. Carroll, J. I. Wolfing, J. Lin, N. Christie, and D. R. Williams. Retinal microscotomas revealed with adaptive-optics microflashes. *Invest. Ophthalmol. Visual Sci.*, 47(9):4161–4167, 2006.

[111] R. K. Tyson. *Principles of adaptive optics*. Academic Press, San Diego, USA, 2^{nd} edition, 1998.

[112] N. Doble, D. T. Miller, G. Yoon, M. A. Helmbrecht, and D. R. Williams. Wavefront corrector requirements for compensation of ocular aberrations in two large populations of normal human eyes. *Proc. SPIE*, 6138, 2006.

[113] D. T. Miller, L. N. Thibos, and X. Hong. Requirements for segmented correctors for diffraction-limited performance in the human eye. *Opt. Express*, 13(1):275–289, 2005.

[114] E. Dalimier and C. Dainty. Comparative analysis of deformable mirrors for ocular adaptive optics. *Opt. Express*, 13(11):4275–4285, 2005.

[115] C. Paterson, I. Munro, and J. C. Dainty. A low cost adaptive optics system using a membrane mirror. *Opt. Express*, 6(9):175–185, 2000.

[116] D. A. Horsley, H. K. Park, S. P. Laut, and J. S. Werner. Characterization for vision science applications of a bimorph deformable mirror using phase-shifting interferometry. In F. Manns, P. G. Söderberg, A. Ho, B. E. Stuck, and eds. M. Belkin, editors, *Ophthalmic Technologies XV*, Proc. SPIE **5688**, pages 133–144, 2005.

[117] L. N. Thibos, A. Bradley, and X. Hong. A statistical model of the aberration structure of normal, well-corrected eyes. *Ophthal. Physiol. Opt.*, 22(5):427–433, 2002.

[118] G. T. Kennedy and C. Paterson. Correcting the ocula aberrations of a healthy adult population using microelectromechanical (mems) deformable mirrors. *Opt. Commun.*, 271(1):278–284, 2007.

[119] S. Bonora andL. Poletto. Push-pull membrane mirrors for adaptive optics. *Opt. Express*, 14(25):11935–11944, 2006.

[120] T. Farrell, E.M Daly, and E. Dalimier C. Dainty. Task-based assessment of deformable mirrors. In *MOEMS-MEMS 2007*, Proc. SPIE **6467**, 2007.

[121] K. M. Hampson. *The higher-order aberrations of the human eye: relation to the pulse and effect on vision*. PhD thesis, Imperial College, London, 2004.

[122] F. C. Delori and K. P. Pflibsen. Spectral reflectance of the human ocular fundus. *Appl. Opt.*, 28(6):1061–1077, 1989.

[123] L. Diaz Santana Haro. *Wavefront sensing in the human eye with a Shack-Hartmann sensor*. PhD thesis, Imperial College of Science, Technology and Medicine, University of London, 2000.

[124] W. H. Southwell. Wave-front estimation from wave-front slope measurements. *J. Opt. Soc. Am.*, 70(8):998–1006, 1980.

[125] E. Delano. First-order design and the $y, \bar{y}$ diagram. *Appl. Opt.*, 2(12):1251–1256, 1963.

[126] L. N. Thibos, M. ye, X. X. Zhang, and A. Bradley. The chromatic eye: a new reduced-eye model of chromatic aberration in humans. *Appl. Opt.*, 31(19):3594–3600, 1992.

[127] S. Marcos, S. A. Burns, E. Moreno-Barriuso, and R. Navarro. A new approach to the study of ocular chromatic aberrations. *Vision Res.*, 39(26):4309–4323, 1999.

[128] G. A. Gescheider. *Psychophysics: The Fundamentals*. Lawrence Erlbaum Associates, Publishers, 10 Industrial Avenue, Mahwah, New Jersey 07430, 3^{rd} edition, 1997.

[129] H. L. DeVries. The quantum character of light and its bearing upon threshold of vision, the differential sensitivity and visual acuity of the eye. *Physica*, 7:553–564, 1943.

[130] A. B. Watson and D. G. Pelli. Quest: A bayesian adaptive psychometric method. *Perc. Psych.*, 33(2):113–120, 1983.

[131] B. Treutwein. Adaptive psychophysical procedures. *Vision Res.*, 35(17):2503–2522, 1995.

[132] A. Peli, L. E. Arend, G. M. Young, and R. B. Goldstein. Contrast sensitivity to patch stimuli: effects of spatial bandwidth and temporal presentation. 7(1):1–14, 1993.

[133] A. B. Watson. Summation of grating patches indicates many types of detectors at one retinal location. *Vision Res.*, 22(1):17–25, 1982.

[134] C. M. Chisholm, A. D. B. Evans, J. A. Harlow, and J. L. Barbur. New test to assess pilot's vision following refractive surgery. *Aviat. Space Environ. Med.*, 74(5):551–559, 2003.

[135] R. F. Hess, C. B. Williams, and A. Chaudhry. Contour interaction for an easily resolvable stimulus. *J. Opt. Soc. Am. A*, 18(10):2414–2418, 2001.

[136] O. Ehrt, R. F. Hess, C. B. Williams, and K. Sher. Foveal contrast thresholds exhibit spatial-frequency- and polarity-specific contour interactions. *J. Opt. Soc. Am. A*, 20(1):11–17, 2003.

[137] R. L. De Valois, H. Morgan, and D. M. Snodderly. Psychophysical studies of monkeys vision – iii. spatial luminance contrast sensitivity tests of macaque and human observers. *Vision Res.*, 14(1):75–81, 1974.

[138] P. Artal, L. Chen, E. J. Fernández, B. Singer, S. Manzanera, and D. R. Williams. Neural compensation for the eye's optical aberrations. *J. Vis.*, 4(4):281–287, 2004.

[139] S. G. de Groot and J. W. Gebhard. Pupil size as determined by adapting luminance. *J. Opt. Soc. Am.*, 42(7):492–495, 1952.

[140] O. Nestares, R. Navarro, and B. Antona. Bayesian model of snellen visual acuity. *J. Opt. Soc. Am. A*, 20(7):1371–1381, 2003.

[141] M. B. Sachs, J. Nachmias, and J. G. Robson. Spatial-frequency channels in human vision. *J. Opt. Soc. Am.*, 61(9):1176–1186, 1971.

[142] H. H. Barrett and K. J. Myers. *Foundations of Image Science*. John Wiley and Sons, Inc., 111 River Street, Hoboken, NJ 07030, 2004.

[143] H. R. Wilson and D. J. Gelb. Modified line-element theory for spatial-frequency and width discrimination. *J. Opt. Soc. Am. A*, 1(1):124–131, 1984.

[144] C. K. Abbey and H. H. Barrett. Human- and model-observer performance in ramp-spectrum noise: effects of regularization and object variability. *J. Opt. Soc. Am. A*, 18(3):473–488, 2001.

[145] V. M. Bondarko and M. V. Danilova. What spatial frequency do we use to detect the orientation of a landolt c? *Vision Res.*, 37(15):2153–2156, 1997.

[146] K. R. Alexander, W. Xie, and D. J. Derlacki. Spatial-frequency characteristics of letter identification. *J. Opt. Soc. Am. A*, 11(9):2375–2382, 1994.

[147] S. T. L. Chung, G. E. Legge, and B. S. Tjan. Spatial-frequency characteristics of letter identification in central and peripheral vision. *Vision Res.*, 42(18):2137–2152, 2002.

[148] R. S. Anderson and L. N. Thibos. Relationship between acuity for gratings and for tumbling-e letters in peripheral vision. *J. Opt. Soc. Am. A*, 16(10):2321–2333, 1999.

[149] R. Navarro, E. Moreno, and C. Dorronsoro. Monochromatic aberrations and point-spread functions of the human eye across the visual field. *J. Opt. Soc. Am. A*, 15(9):2522–2529, 1998.

[150] D. A. Atchison and D. H. Scott. Monochromatic aberrations of human eyes in the horizontal field. *J. Opt. Soc. Am. A*, 19(11):2180–2184, 2002.

[151] S. S. Choi, N. Doble, J. L. Hardy, S. M. Jones, J. L. Keltner, S. S. Olivier, and J. S. Werner. In vivo imaging of the photoreceptor mosaic in retinal dystrophies and correlations with visual function. *Invest. Ophthalmol. Visual Sci.*, 47(5):2080–2092, 2006.

[152] J. I. Wolfing, M. Ching, J. Carroll, A. Roorda, and D. R. Williams. High-resolution retinal imaging of cone-rod dystrophy. *Ophthal.*, 113(6):1014–1019, 2006.